

ION ENERGIZATION BY A PAIR OF BEATING ELECTROSTATIC WAVES

ROSTISLAV SPEKTOR

A DISSERTATION
PRESENTED TO THE FACULTY
OF PRINCETON UNIVERSITY
IN CANDIDACY FOR THE DEGREE
OF DOCTOR OF PHILOSOPHY

RECOMMENDED FOR ACCEPTANCE
BY THE DEPARTMENT OF
MECHANICAL AND AEROSPACE ENGINEERING

NOVEMBER, 2006

© Copyright by Rostislav Spektor, 2006.

All Rights Reserved

Abstract

It has been shown that a pair of beating electrostatic waves (BEW) propagating perpendicularly to a magnetic field can, under some conditions, accelerate ions from arbitrarily low initial velocity, in stark contrast with the well-known nonlinear threshold criteria for ion acceleration by a single electrostatic wave (SEW). Such a mechanism is believed to be the cause of rapid ion acceleration from the Earth's ionosphere. The goal of this dissertation is to improve the theoretical understanding of the BEW ion acceleration mechanism through analytical and numerical investigations, and to demonstrate ion heating by beating electrostatic waves for the first time in a laboratory environment. It was found that the necessary and sufficient conditions for the acceleration to occur may be described through the Hamiltonian formulation. The elliptic and hyperbolic critical points on the Poincaré section define a potential well, which an ion must overcome in order to be accelerated by the beating waves. It is also found that in a collisional plasma the acceleration is further enhanced by the ion-ion collisions, which also thermalize the energy. In a collisionless plasma, appropriate wave frequencies may be chosen to optimize the heating efficiency. An experimental study of ion heating by beating electrostatic ion cyclotron (EIC) waves in a magnetized, radio-frequency sustained plasma has also been performed. Ion heating up to 35% was observed in the presence of the EIC waves excited by a two-plate antenna. It was found that ion-neutral collisions significantly damp the backward branch of the EIC wave, which is most effective in coupling with ions. Thus, ion-neutral collisions indirectly play a detrimental role in the heating mechanism. Despite the damping effects of such collisions, it was shown that the beating electrostatic waves can heat ions to a higher temperature than a single electrostatic wave. This enhancement in ion temperature was found to be 15% for the particular conditions of the reported experiment, but is expected to be significantly higher in a less collisional plasma. This finding supports the theoretical prediction that beating waves can produce more efficient heating by interacting with ions below the single-wave velocity threshold.

Acknowledgements

I received immeasurable support from many people during my graduate studies. Without them I could not have succeeded. This dissertation cannot be complete without expressing my gratitude for their help.

First and foremost I would like to thank my wife, Tanya, for sacrificing so much for me. Your patience, devotion, and love have guided me through many tough days. Your smile at the end of the day made it all worth it. Thank you for being in my life.

I would also like to thank my advisor, professor Choueiri, for suggesting this topic for my graduate research. Your unwavering pursuit of perfection in research and life in general has been one of the most important lessons that I've learned in Princeton. To rf magician, and Smith chart extraordinaire, Bob Sorenson, without your help I would still be trying to get my experimental setup together. Your expertise and precision in the machine shop are unrivalled. May the price of gold increase exponentially!

To my three classmates, Lenny Cassady, Jack Berkery, and Kurt Polzin, I know that in you I have found friends for life. You will be successful in all your undertakings, and I am looking forward our future research collaborations. To Tom Markusic and Kamesh Sankaran, thank you for saving me from many injuries by showing the picture of Tom's black eye. That picture is the reason why I stopped playing squash. To Andrea Kodys, your compassion and humanity are commendable, I have not met a gentler person. I know you will enjoy teaching! Jimmy Cooley, you are the coolest and smartest guy I know. I will always remember how much fun Becca, you, Tanya, and me had in Italy. To Luke Uribarri, well, you are probably tired of hearing it by now, but I am sorry for the broken nose. I am simply amazed at how good you are at everything you do. If you ever end-up in the Southern California I hope we can take up tennis again, and maybe I can beat you in a 3-mile race. Peter Norgaard, you have taken on one of the toughest projects, and I wish you luck. I am glad that the tradition of good story telling is alive and well in our lab. It seems that the skill is passed through the "numerical" gene.

I would also like to thank professor Earl Scime and Costel Biloiu of the West Virginia University for their help in designing and constructing the portable LIF system used in the experiments reported in this dissertation. You've been the last-minute life savers to me in the time of desperation.

To all the teachers I've had throughout my life – each one of you have left a mark. To professors Samuel Cohen, Philip Holmes, Szymon Suckewer, and Robert Jahn, you are the top experts in your fields, and I am extremely honored to count myself as one of your students. To professor emeritus and my undergraduate mentor Antoni Oppenheim, you have taught me so much more than just science. Your energy and zest for life are unending.

Last, but not least, I would like to thank my parents for raising me, instilling the right values, and encouraging me to be a good student. I can only hope to be as good of a parent to my children as you've been to me.

This work was supported by a research contract from the Air Force Office of Scientific Research (AFOSR), Department of Aerospace and Materials Science (Dr. Mitat Birkan, Program Manager). It also was supported by the Program in Plasma Science and Technology, Princeton Plasma Physics Laboratory.

Чтобы достичь совершенства, надо прежде многого не
понимать! А слишком скоро пойдем, так, пожалуй, и не хорошо
пойдем. Это я вам говорю, вам, которые уже так много умели
понять... и не понять.

Достоевский, Федор Михайлович
Из "Идиота"

No one can begin by being perfect - there is much one cannot understand in
life at first. In order to attain to perfection, one must begin by failing to
understand much. And if we take in knowledge too quickly, we very likely are
not taking it in at all. I say all this to you - you who by this time understand so
much - and doubtless have failed to understand so much, also.

Dostoevskii, Fedor Mikhailovich
From "The Idiot"

Nomenclature

\perp	Perpendicular to applied magnetic field
\parallel	Parallel to applied magnetic field
$J_\nu(\rho)$	Bessel function of the first kind
$I_\nu(\rho)$	Modified Bessel function of the first kind
$\Gamma(\rho)$	Gamma function
m_e	Mass of an electron
m_i	Mass of an ion
q	Elementary charge
k_b	Boltzmann's constant
γ	Adiabatic index
E	Electric field
B	Magnetic field
$v = (v_x, v_y, v_z)$	Particle velocity in the laboratory frame
$u = (u_x, u_y, u_z)$	Relative particle velocity in the center of mass frame
v_{de}	Parallel electron drift velocity
v_{di}	Diamagnetic ion drift velocity
v_{te}	Electron thermal velocity
v_{ti}	Ion thermal velocity
c_s	Ion sound speed
v_A	Alfvén speed
c	Speed of light
$\mathbf{k} = (k_\perp, k_\parallel)$	Wavenumber
f	Frequency in Hz
ω	Frequency in s^{-1}
ω_{ce}	Electron cyclotron frequency
ω_{ci}	Ion cyclotron frequency

ω_{pe}	Electron plasma frequency
ω_{pi}	Ion plasma frequency
r_L	Ion Larmor radius
T_e	Electron temperature
T_i	Ion temperature
n_e	Plasma density
$Z(\zeta_n^j)$	Plasma dispersion function
$f_e(v)$	Electron velocity distribution function
$f_i(v)$	Ion velocity distribution function
V	Electric potential
V_p	Plasma potential
V_f	Floating potential
I	Electric current
I^{sat}	Saturation current
Z_r, Z_i	Real and imaginary components of impedance
$\varepsilon = k_{\perp} q E / m_i \omega_{ci}$	Normalized wave amplitude
$\nu = \omega / \omega_{ci}$	Normalized wave frequency
$\kappa_{\perp} = k_{\perp} / k_{\perp,1}$	Normalized wavenumber, where subscript “1” refers to a reference wave
$\tau = \omega_{ci} t$	Normalized time
ρ	Normalized Larmor radius
θ	Particle phase angle
H	Hamiltonian
A_p	Langmuir probe tip surface area
ν_{l0}	Laser frequency in the laboratory coordinate system
ν_l	Doppler-shifted laser frequency
$I_l(\nu_l)$	Light intensity

Contents

Abstract	iii
Acknowledgements	iv
Nomenclature	vii
1 Introduction	1
1.1 Background and Motivation	1
1.2 Dissertation Objectives	2
1.3 Ionospheric Rocket Observations	3
1.4 Previous Laboratory Experiments	4
1.5 Review of Previous Theoretical Work	6
1.5.1 Single-Wave Ion Acceleration	7
1.5.2 Multi-Wave Ion Acceleration	8
1.6 Dissertation Outline and Approach	10
2 Theoretical Investigation	11
2.1 Resonance Overlap and Stochastic Motion	12
2.2 Choosing the Analytical Model	13
2.3 Analytical Formulation	14
2.4 Poincaré Section Construction	19
2.5 Single-Wave Interaction	21
2.6 Multi-Wave Interaction	24
2.6.1 Multiple Non-beating Waves	25

2.6.2	Two Beating Waves	27
2.6.3	ε Dependence	31
2.6.4	ν Dependence	33
2.7	Critical Points	33
2.8	Particle Motion in the Regular Acceleration Region	41
2.9	Two Beating On-resonance Waves	45
2.10	Chapter Summary	47
3	Numerical Investigation	49
3.1	Single Particle Model	50
3.2	Including Collisions	53
3.2.1	Overall Implementation	54
3.2.2	Momentum Exchange During Collisions	55
3.2.3	Moving the Particles	57
3.3	Simulations	58
3.3.1	Poincaré Sections	59
3.3.2	Velocity Evolution	62
3.4	Chapter Summary	74
4	Experimental Setup and Diagnostics	75
4.1	Vacuum Chamber	75
4.2	Plasma Source	79
4.3	Electrostatic (ES) Wave Antennas	83
4.3.1	Two-plate ES Antenna	84
4.3.2	Loop ES Antenna	84
4.3.3	Beating Waves – Mixing Signals from Two Sources	87
4.4	Diagnostics	88
4.4.1	Langmuir Probes	88
4.4.2	Electron Temperature and Plasma Density Measurements	90

4.4.3	Dispersion Relation Measurements	92
4.4.4	Laser Induced Fluorescence	94
4.4.5	LIF Theory	95
4.4.6	LIF Implementation	97
4.4.7	LIF Instrumentation	98
4.5	Operation and Procedures	101
5	Experimental Results and Analysis	102
5.1	Wave Detection	103
5.2	Dispersion Relation Measurements	107
5.3	Effects of Ion-Neutral Collisions	112
5.4	Ion Heating in the BWX	113
5.5	Final Remarks	119
6	Conclusions	121
6.1	Summary of Major Findings	122
6.1.1	Theoretical Findings	122
6.1.2	Numerical Findings	123
6.1.3	Experimental Findings	124
6.2	Recommendations for Future Work	124
A	Review of Previous Work	127
A.1	Review of Ionospheric Rocket Observations	127
A.2	Review of Previous Laboratory Experiments	130
A.2.1	EIC Waves Excited with Field Aligned Currents (CDEIC)	131
A.2.2	EIC Waves Excited without Field Aligned Currents	133
A.2.3	Waves Excited by Antennas	135
B	Derivation of the Hamiltonian	137
B.1	Lorentz Equation	137

B.2	Canonical Variables	139
C	Lie Transformations	141
C.1	General Considerations	141
C.2	First-Order Solution	144
C.3	Second-Order Solution	145
C.4	Autonomous Hamiltonian to the Second Order	148
D	$S_6^{\nu_i, \nu_j}(\rho)$ Term Simplification	150
E	Symplectic Integration Algorithm	152
F	ES Dispersion for a Homogeneous, Isotropic, Magnetized, Collisional Plasma	154
	Bibliography	158

Chapter 1

Introduction

Research is what I'm doing when I don't know what I'm doing.

– Wencher Von Braun

1.1 Background and Motivation

Nonlinear wave-particle interactions in plasmas occur naturally in space plasmas, and are harnessed in the laboratory for plasma generation and plasma heating for fusion applications. An example of such an interaction is ionospheric ion acceleration by electrostatic waves that propagate perpendicularly to the Earth's magnetic field. An electrostatic wave is a wave with the oscillating electric field, \mathbf{E} , aligned along the direction of wave propagation, \mathbf{k} . According to Maxwell's equations such a wave does not have an oscillating magnetic field component. The fundamental mechanism behind ion acceleration by a single electrostatic wave (SEW) was first elucidated theoretically by Karney [1] in 1977. He found that ion acceleration is inherently a stochastic mechanism that can only occur if the particle velocity is within a nonlinearly broadened resonance with the wave, and is also above a velocity threshold ($v \gtrsim \omega/k_{\perp}$).

Ion acceleration by a *spectrum* of electrostatic waves propagating perpendicularly to the magnetic field was proposed by Ram *et al.* [2] in 1998 as an explanation for ionospheric ion

acceleration observed by the Topaz 3 rocket. In the same year Benisti *et al.* demonstrated that ions with arbitrarily low initial velocity can be accelerated through a nonlinear interaction with the waves whenever the spectrum contains a pair of waves that obey a beating criterion [3, 4],

$$\omega_2 - \omega_1 = n\omega_{ci},$$

where ω_1 and ω_2 are the frequencies of the two waves, $\omega_{ci} = qB_0/m_i$ is the ion cyclotron frequency, and n is a positive integer. As will be shown later in this dissertation, the above criterion is necessary but not sufficient for acceleration to occur.

The main feature of ion acceleration by beating electrostatic waves (BEW) is the lack of threshold for the initial ion velocity. This renders a plasma heating scheme based on this effect a particularly efficient one, as compared to resonant wave heating, since a larger portion of the ion distribution function can interact with the waves. Since the BEW ion acceleration mechanism can energize ions whose velocity is well below the single-wave threshold, we expect that in real plasmas the ion temperature will be enhanced, as compared to the case of SEW heating. This is particularly appealing for electric propulsion applications, where higher heating efficiency implies system benefits.

1.2 Dissertation Objectives

The goal of this dissertation is to investigate nonlinear interaction between beating electrostatic waves and charged, magnetized particles. Theoretical works by Karney *et al.* and Benisti *et al.* noted in the section above, serve as a starting point for this dissertation. While many questions about the wave-particle interaction remain unanswered, this dissertation is focused on three of these questions:

- What is the nature of the BEW acceleration mechanism?

- What are the necessary and sufficient conditions for particle acceleration by beating electrostatic waves?
- How can the beating electrostatic waves acceleration mechanism be demonstrated in the laboratory?

In order to answer these questions we first review previous works on the subject of particle interaction with electrostatic waves. In particular, we overview ionospheric rocket observations pertaining to the Cleft Ion Fountain phenomenon and previous theoretical and experimental investigations of electrostatic wave propagation and particle heating in magnetized plasmas.

1.3 Ionospheric Rocket Observations

The work described in this dissertation was initially motivated primarily by the ionospheric observation of the Cleft Ion Fountain (CIF) and related phenomena [5]. The CIF, shown schematically in Fig. 1.1, is a large-scale outflow of energetic ions from the regions of the low-altitude polar ionosphere, and serves as a major source of the Earth's magnetospheric plasma. It has been suspected that the Cleft Ion Fountain may be the result of the interaction between ions and electrostatic waves propagating in the Earth's ionosphere.

Most of the evidence toward the ionospheric origin of magnetospheric plasma comes from a variety of satellite observations that point to high-energy ions streaming from ionosphere to magnetosphere [6]. In particular, it has been observed that vigorous ion acceleration from the ionosphere takes place both parallel and perpendicular to the ambient magnetic field at an altitude ranging from 400 km to 8000 km. The most detailed study of ion acceleration was performed by the S3-3 (1976-65B) satellite that was launched in 1976, and performed the first *in situ* measurements of electric fields in the auroral region [7, 8]. A more comprehensive overview of ionospheric rocket observations is given in Appendix A.

A connection between ion acceleration and electrostatic waves was established by

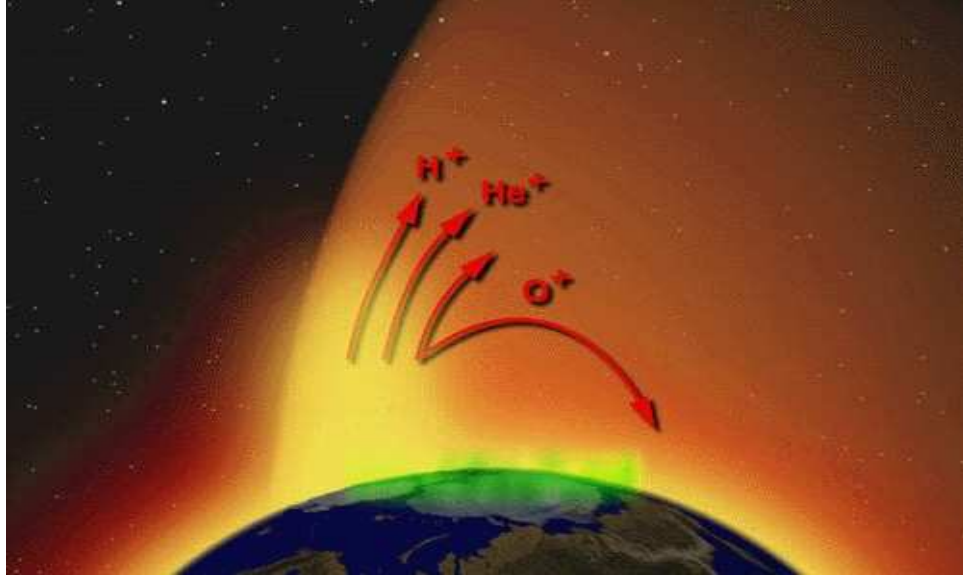


Figure 1.1: An artist's depiction of the Cleft Ion Fountain showing ions being accelerated out of the ionosphere in the Earth's auroral region. This picture is taken from <http://pluto.space.swri.edu>.

Mozer *et al.* [7], who investigated the plasma density and electric field fluctuation data collected by the S3-3 satellite. They determined that the electric field structure observed by the spacecraft in the region of ion acceleration was due to formation of Electrostatic Ion Cyclotron (EIC) waves.

1.4 Previous Laboratory Experiments

While transverse ionospheric ion acceleration was observed in regions of electrostatic wave activity, the satellite observations could not unambiguously point to the wave-ion interaction mechanism as the source of acceleration. Laboratory experiments simulating ionospheric conditions were therefore conducted to investigate this interaction mechanism.

In 1963 Motley and D'Angelo [13] performed a series of experiments where they excited a *single* Electrostatic Ion Cyclotron (EIC) wave in a Q-machine (first described by Rynn and D'Angelo in 1960 [14]) by drawing the electron current along the magnetic field lines. Using similar experimental configuration Cartier *et al.* [15] measured perpendicular

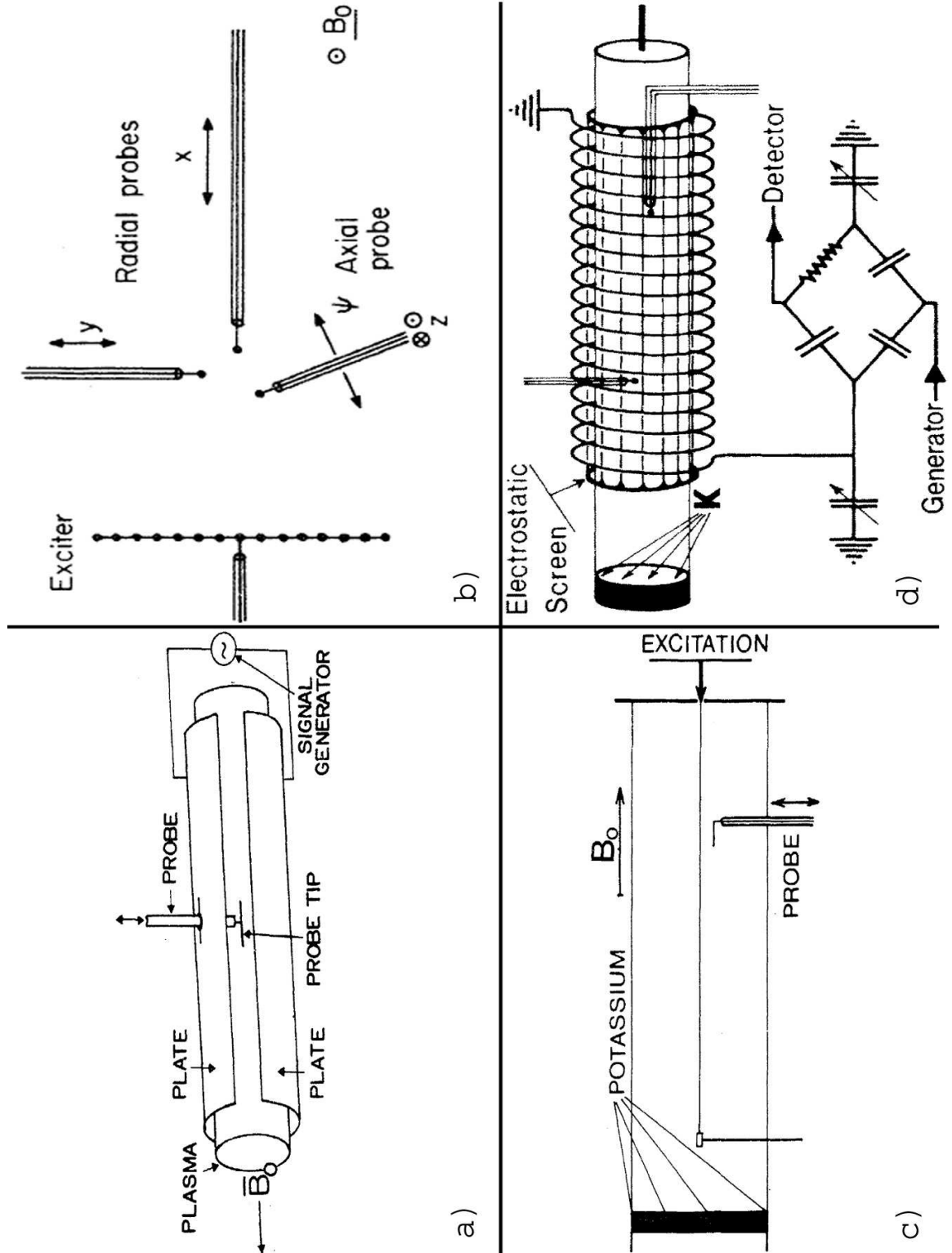


Figure 1.2: Schematics of various experiments to study electrostatic waves in magnetized plasmas. a) and b) Schematics of two experiments to study the waves in the lower-hybrid range of frequency [9, 10]. c) Schematic of an experiment reported by Schmitt [11], who studied propagation of the Pure Ion Bernstein wave. d) Experimental setup for studying mode conversions [12].

ion heating when the current exceeded a certain threshold. These experiments corroborated the S3-3 data, which also showed that the electron field-aligned current in the ionosphere was above the threshold necessary for the excitation of the hydrogen EIC wave [8]. Additionally, Goree *et al.* [16] (1985) and Skiff *et al.* [17] (1987) used an electrostatic plate antenna to launch a single electrostatic wave above the ion cyclotron frequency perpendicularly to the magnetic field in argon and neon plasmas. Similar experiments were performed in hydrogen and deuterium plasmas by Alba *et al.* [18]. These experiments also reported significant ion heating. Figure 1.2 shows a few other experimental arrangements used to study electrostatic waves in magnetized plasmas. A broader review of various laboratory wave-particle interaction experiments is given in Appendix A.

1.5 Review of Previous Theoretical Work

The ionospheric and laboratory observations of particle heating by electrostatic waves that were described in the previous sections did not fit within the existing theoretical understanding of plasma heating, and motivated the development of new theoretical approach. A model developed by Zaslavsky and others [19, 20, 21, 22] showed that ion acceleration results from the nonlinear interaction between the waves and ions. Since the resulting particle motion is stochastic, as will be discussed in the next section, we will refer to this type of acceleration as the stochastic acceleration. Also, because temperature is a statistical property of a particle aggregate, we will adopt the following convention: whenever we refer to the wave interaction with multiple particles we will talk about *stochastic heating*, however, when we investigate the wave interaction with a single particle we will talk about *stochastic acceleration* instead.

1.5.1 Single-Wave Ion Acceleration

As was mentioned in previous sections, the theory of stochastic acceleration by a single obliquely, as well as transversely, propagating electrostatic (ES) wave was primarily developed to explain the ionospheric ion acceleration related to the CIF phenomenon [23, 24, 1, 25, 22]. The theory showed that while the equations describing the particle motion are completely deterministic, i.e. contain no random forces, the solutions to these equations produce intrinsically stochastic particle dynamics. Smith and Kaufman [23, 25] (1975) studied stochastic acceleration by an obliquely propagating wave. They derived the threshold for the wave-particle interaction and found an analytical approximation that described the particle dynamics. Their theory was applied to the problem of the ionospheric ion heating by Singh *et al.* [26] and Menyuk *et al.* [27].

Karney [28] (1978) was able to derive analytical expressions approximating the dynamics of an ion interacting with a single wave that propagates transversely to the magnetic field. He found that, just like for oblique waves, there is a threshold condition for the wave amplitude below which no stochastic heating is observed. Skiff *et al.* (1987) have validated these findings experimentally [17]. Papadopoulos [29] applied Karney's analysis to the problem of ionospheric ion acceleration and Lysak *et al.* used a similar idea to show how an ionospheric ion can gain energy in the presence of more than one wave [30].

Another important result shown by Karney was the existence of an ion velocity threshold below which the ions cannot gain energy from an ES wave. This threshold is essentially the lower bound of a nonlinearly broadened resonance condition between the ion and wave phase velocities. If the initial velocity of an ion is below the threshold, then the ion is not accelerated by the wave. This threshold was also found to separate two regions of the ion motion: a *regular* (or coherent) motion region of low energies below the threshold and a *stochastic* region – above the threshold. Nonlinear ion acceleration (or energization) by a single wave is therefore always a stochastic process.

The intricacies of the nonlinear dynamics describing the interaction between a single

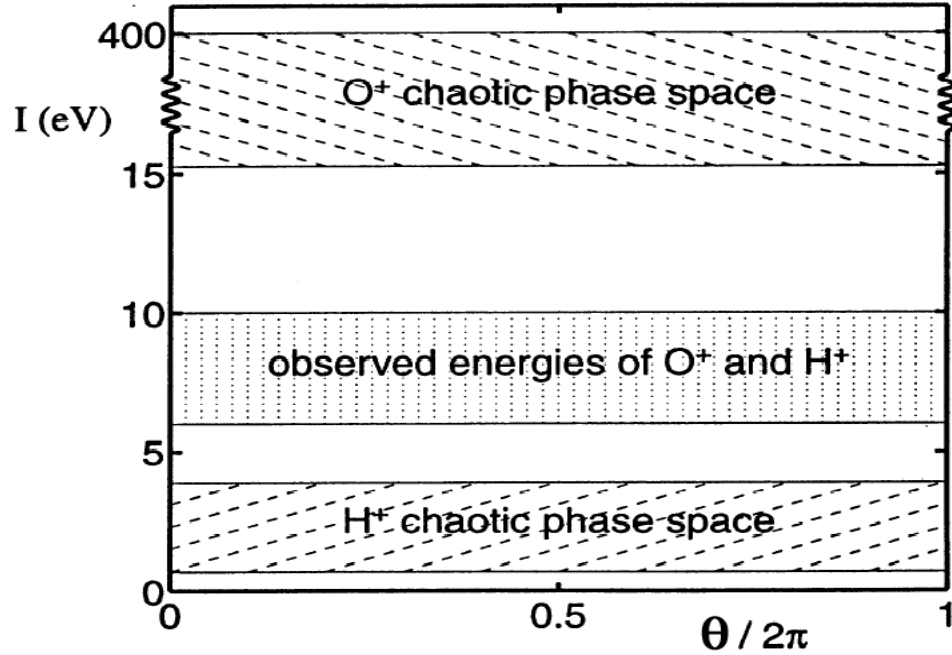


Figure 1.3: This figure demonstrates that the single-wave theory does not predict correctly the ion energies observed in the ionosphere. Ion energies predicted by the single-wave theory are shown by H^+ and O^+ “chaotic phase space”. The x axis is the phase angle of the ions as described in Chapter 2. The figure is taken from Ref. [2].

wave and a charged particle, and stochastic acceleration in general are discussed in a book by Lichtenberg and Lieberman [31] published in 1983. A more detailed approach with specific emphasis on particle acceleration is taken in a book by Zaslavsky *et al.* [22].

1.5.2 Multi-Wave Ion Acceleration

While the investigations of a single wave ion interaction by Karney *et al.* and Smith and Kaufman were successful in describing the single-wave interaction, they did not fully explain the CIF phenomenon. For example, as was pointed out by Ram *et al.* [2], the single-wave theories either under- or over-predict the observed H^+ and O^+ ion energies, which are shown in Fig. 1.3. In that figure, the observed ion energies are either above (for H^+) or below (for O^+) the energies predicted by the single-wave theory, which are marked as “chaotic phase space”. To improve upon the single-wave model, efforts were made to include multiple waves. Deeskow *et al.* [32] used both kinetic and Hamiltonian approaches

to study the interaction of multiple waves with one common frequency but different wave vectors. Zaslavsky *et al.* [20] studied interaction between a particle and a propagating wave packet. Chia *et al.* [33] employed the Lie transformation technique to arrive to a general second-order equation that described a system of one particle and multiple waves.

In 1998 Benisti *et al.* improved upon these works by suggesting that a particular combination of multiple waves that propagate perpendicularly to the Earth's magnetic field can fundamentally alter the stochastic acceleration mechanism [3, 4]. The proposed scheme required *pairs* of the ES waves such that their corresponding frequencies differ by an integer number of the ion cyclotron frequency, as shown in Eq. (1.1). In essence, these waves create a beating wave that interacts with the ions. Under such conditions the single-wave theory threshold is modified in such a way that the regular and stochastic acceleration regions become connected, allowing ions with arbitrary small initial velocity to obtain high energy through coherent acceleration followed by stochastic energization. Because the beating waves can accelerate the slower ions, this type of nonlinear interaction may result in a more efficient ion heating mechanism in a real plasma than the single-wave scheme.

It is important to note that because of the dispersion properties of electrostatic waves in a real plasma, these waves do not propagate exactly at 90° with respect to magnetic field. In recent years (2003) investigations by Strozzi *et al.* [34] have been conducted to extend the theoretical BEW model introduced by Benisti *et al.* to include the effects of finite parallel wavenumber. That work has shown that regular and stochastic acceleration regions remain connected to each other as long as the beating waves have the same parallel wavenumber. This condition can be achieved in the laboratory by launching beating electrostatic waves simultaneously from the same antenna.

The BEW interaction allows acceleration of a larger portion of the ion velocity distribution than the single electrostatic wave (SEW) interaction, and may be promising for many applications where the efficiency of ion heating is of prime importance. These applications can range from fusion plasma heating to space plasma propulsion.

1.6 Dissertation Outline and Approach

The series of papers published by Benisti *et al.* [35, 3, 4] serve as the starting point for the work presented in this dissertation. The dissertation reports on *theoretical*, *numerical*, and *experimental* investigations of ion acceleration and heating by beating electrostatic waves. In order to address three dissertation objectives that were established in Section 1.2 we focus this work on

1. Refining the previous theories by defining the *necessary and sufficient* conditions for the ion acceleration by beating electrostatic waves,
2. Developing a numerical simulation of ion heating by beating electrostatic waves that takes into account ion collisions,
3. Presenting experimental results that our support theoretical and numerical findings.

Chapter 2 of this dissertation contains a theoretical description, which is based on first principles, that is used to describe the interaction between a single ion and beating electrostatic waves (BEW). The description is similar in spirit to the approach developed by Karney *et al.* [1] and Benisti *et al.* [3]. Using this approach we proceed to derive necessary and sufficient conditions for the ion acceleration by beating electrostatic waves. In Chapter 3 we build upon this theoretical framework with a numerical investigation of multiple ions interacting with beating electrostatic waves. The investigation includes ion-ion collisions through a Monte-Carlo technique. In Chapter 4 we overview the experimental setup of the Beating Wave Experiment (BWEX) and its diagnostics. The Beating Waves Experiment at the Princeton's Electric Propulsion and Plasma Dynamics Laboratory (EPPDyL) was the first laboratory demonstration of the ion heating by beating electrostatic waves. In Chapter 5 we present and analyze the results of the experimental investigation. Finally, in Chapter 6 we offer concluding remarks and suggests future avenues for the research.

Chapter 2

Theoretical Investigation

In theory, there is no difference between theory and practice. But, in practice, there is.

– Jan L.A. van de Snepscheut

This chapter describes theoretical investigation of the interaction between a charged, magnetized particle and two beating electrostatic waves. As was discussed in Chapter 1, the interest in this problem arose from the ionospheric observations, as well as some theoretical and experimental studies of ion acceleration by electrostatic waves. However, in principle the equations described here can be applied to any magnetized charged particle, including electrons, and in some cases waves that are not purely electrostatic, as discussed in Section 2.3.

The approach undertaken in this chapter involves solving the equation of particle motion using a second-order perturbation theory to examine the dynamics of the interaction. Additionally, we use a combination of analytical and numerical solutions to investigate the nature of particle motion for a wide range of relevant parameters.

As a first step for describing our theoretical work we make some general comments on the nature of stochastic acceleration and various analytical approaches taken to investigate it. We then overview the analytical formulation of the problem, and summarize the

better-known results for the single wave case. Beating wave interaction is introduced in Section 2.6. In that section we first describe the dynamics of an ion interacting with a pair of non-beating waves, and then contrast that with the case of the beating electrostatic waves. Next, for the case of beating electrostatic waves, we focus our analysis on finding the necessary and sufficient conditions for stochastic acceleration to occur.

2.1 Resonance Overlap and Stochastic Motion

One of the most important concepts relevant to wave-particle interactions is the resonance between the wave and the particle. A classical example of a resonant interaction is Landau damping. When a large number of particles have velocity on the order of the wave phase velocity, energy transfer between the wave and the particles can occur. Particles that move slightly below the wave phase velocity gain energy from the wave, and particles that move slightly faster than the wave lose energy to it.

Very often a situation arises when multiple wave-particle resonances are present. In principle the appearance of extra resonances does not produce a fundamental difficulty in finding the analytical solution. However, when the wave amplitude is large enough the resonances might grow and eventually start to overlap [31]. In that case the particle motion may become random, or more precisely stochastic. Equations describing the particle motion in those cases do not have an exact analytical solution, and need to be solved to at least the second order. This is certainly true for the ions interacting with electrostatic waves. Stochastic ion acceleration resulting from such an interaction requires at least a second-order analysis.

Stochasticity refers to the process in which the trajectories of any two particles initially infinitely close to each other diverge exponentially with time. It is important to note that stochasticity in the particle motion does not come from any random forces. Indeed, the equations describing the beating wave particle interaction contain no random terms and

look deceptively simple at first glance. Neither does the stochasticity necessarily result from any random particle-particle interactions. Stochastic behavior may even arise for a simple system consisting of only one particle and one wave. Stochasticity in fact, is an intrinsic property of some nonlinear equations. Furthermore, analogous to random motion, one can define stochastic diffusion (Arnol'd diffusion) [20, 36, 37]. This concept serves as a bridge between two types of the analytical models used to describe the stochastic wave-particle interaction. These models are the subject of the next section.

2.2 Choosing the Analytical Model

One of the requirements necessitated by the nature of our investigation is that the analytical model should be able to track individual particle trajectories in the field of the waves. This condition makes fluid models inappropriate, leaving only two choices: kinetic and particle-dynamic models.

Particle-dynamic models offer a more manageable approach to the problem of stochastic acceleration by beating electrostatic waves. The approach is limited to dealing with a single particle interacting with one or more waves, and thus produces a simple set of equations, derived directly from Newton's and Lorentz's equations. Furthermore, this method can serve as a stepping stone to more complex models. For this reason, particle-dynamic models were the methods of choice for Zaslavsky [19, 20, 21, 22], Karney [1, 28, 38], Benisti [35, 3, 4], and others, who investigated nonlinear interaction mechanisms between a single particle and electrostatic waves. Because of the existing body of knowledge, and simplicity of the equations, the particle-dynamic model used by Karney and Benisti is adopted for this chapter. While simple, this approach allows us to study the fundamental nature the nonlinear interaction mechanism between a single, charged, magnetized particle and beating electrostatic waves.

One the other hand, the kinetic approach treats multiple particles, and is generally a

better way to model a real plasma. It is usually the tool of choice to tackle wave-particle interaction problems that do not result in stochastic particle behavior, such as Landau damping. Additionally, propagation of some plasma waves can only be described using a kinetic model. The dispersion relation for the backward branch of the Electrostatic Ion Cyclotron (EIC) wave, given in Section 5.2 and in Appendix F, is a good example of kinetic model application.

However, application of kinetic theories to the problem of stochastic particle acceleration by beating electrostatic waves produces an extremely complex set of equations. Some successful efforts in obtaining the nonlinear evolution of particle velocity distribution using this type of models are reported in Refs. [19] and [39]. However, because of the complexities involved in the kinetic treatment, we choose to investigate beating electrostatic wave interaction with multiple particles through a Monte Carlo numerical simulation. This work will be described in the next chapter.

2.3 Analytical Formulation

We start by defining the coordinate system as shown in Fig. 2.1. The figure shows a single ion of mass m and charge q in a constant, homogeneous magnetic field $B_0 \hat{z}$. This ion interacts with a packet of electrostatic waves that propagate in the positive x direction. While in a real plasma electrostatic waves do not propagate precisely perpendicularly to magnetic field, work by Strozzi *et al.* [34] has demonstrated that as long as the angle of propagation is close to 90° , and wavenumbers of the beating electrostatic waves are equal, particle dynamics is similar to the case of perpendicular wave propagation. Therefore, for the sake of simplicity we will focus on the perpendicular wave propagation. Because the waves are purely electrostatic the wavenumber $k_{\perp j}$ is parallel to the electric field E_j direction of each of these waves, and hence lie in xy -plane. The x - y motion of the single ion in Fig. 2.1 is described by the following equation of motion, which is given in Refs. [33] and [3], and is

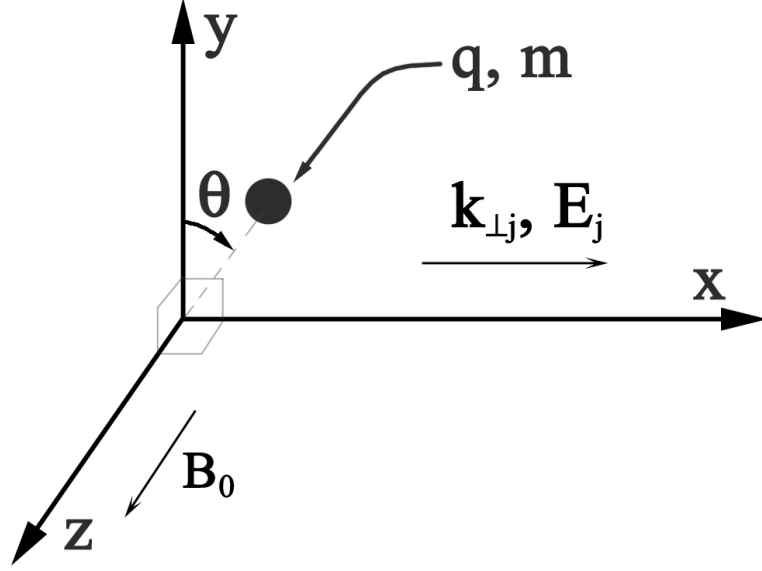


Figure 2.1: A single ion of charge q and mass m in a constant homogeneous magnetic field $\mathbf{B}\hat{z}$ interacts with a spectrum of electrostatic waves whose wavenumber and electric field direction is parallel to the x -axis.

also derived for completeness in Appendix B:

$$\frac{d^2x}{dt^2} + \omega_{ci}^2 x = \frac{q}{m} \sum_{j=1}^n E_j \sin(k_{\perp j} x - \omega_j t + \varphi_j), \quad (2.1)$$

where $\omega_{ci} = qB_0/m$ is the ion cyclotron frequency and φ_j is the phase angle each wave.

As a footnote we should mention that similar analysis can be applied to other stochastic heating problems. Alfvén wave heating is one such example [40, 41]. The similarity can be demonstrated by considering a linearly polarized Alfvén wave propagating obliquely to the external magnetic field such that magnetic field of the wave $B = B_w \cos(kx - \omega t)$ and its frequency $\omega = k_z v_A$. Here k_z is the z component of the wavenumber and v_A is the Alfvén velocity. The resulting equation of motion is [41]

$$\frac{d^2x}{dt^2} + x = x_0 - v_z B_w \cos(kx - \omega t), \quad (2.2)$$

where to the zeroth order both B_w and v_z , which is the z component of the wave velocity,

are assumed to be constant. The equation above is similar to Eq. (2.1). Therefore, the subsequent analysis of the stochastic heating by Alfvén waves may follow along the path described below in this chapter.

The corresponding Hamiltonian for the system is [3]

$$\bar{H} = \rho^2/2 + \sum_{j=1}^n \frac{\varepsilon_j}{\kappa_{\perp j}} \cos(\kappa_{\perp j} \rho \sin \theta - \nu_j \tau + \varphi_j). \quad (2.3)$$

The derivation of the above equation of motion, as well as the Hamiltonian form, are detailed in Appendix B. In writing Eq. (2.3) we have used the fact that the system is periodic, and transformed the Hamiltonian into a normalized action-angle coordinate system [42], where $\kappa_{\perp j} = k_{\perp j}/k_{\perp 1}$, $\nu_j = \omega_j/\omega_{ci}$, $\tau = \omega_{ci} t$, $\varepsilon_j = (k_{\perp 1} q E_j)/(m \omega_{ci}^2)$, $\rho^2 = X^2 + \dot{X}^2$, and $X = k_{\perp 1} x$, $\dot{X} = dX/d\tau$, so that $X = \rho \sin \theta$, $\dot{X} = \rho \cos \theta$. The action-angle coordinate system is somewhat similar to polar coordinates, where θ corresponds to the cyclotron phase angle measured clockwise from the y -axis in the xy plane, as indicated in Fig. 2.1, while ρ is the normalized Larmor radius. In a constant magnetic field the variations in the Larmor radius correspond to the changes in the particle perpendicular velocity.

When ν_j is exactly an integer we speak of an *on-resonance* wave, otherwise we speak of an *off-resonance* wave. This chapter focuses on the off-resonance cases because, as will be demonstrated in Section 2.7, the analytical expressions for the off-resonance waves are significantly simpler.

Benisti *et al.* [3] defined a criterion for vigorous particle acceleration by multiple ES waves. They showed that for a particle with an arbitrary low initial velocity to undergo stochastic acceleration it is necessary (but, as we shall shortly show, not sufficient) to have at least one pair of ES waves such that

$$\omega_2 - \omega_1 = n \omega_{ci}, \quad (2.4)$$

where n is an integer. They also reported that the acceleration is more vigorous for $n \leq$

2, therefore for the sake simplicity we limit our analysis to the case of a single pair of beating electrostatic waves, such that $n = 1$. In addition, Ref. [3] reports that the maximum acceleration is achieved when all waves are of the same amplitude, $\varepsilon_i = \varepsilon_j = \varepsilon$. We also set $\kappa_{\perp i} = \kappa_{\perp j} = \kappa_{\perp 1}$ to simplify our analysis, and since the phase angles, φ_j , do not play a fundamental role in this acceleration process [3] we set all $\varphi_j = 0$. With these simplifications the Hamiltonian (2.3) becomes

$$\begin{aligned} \bar{H} = \rho^2/2 + \varepsilon[\cos(\rho \sin \theta - \nu_i \tau) + \\ \cos(\rho \sin \theta - \nu_j \tau)]. \end{aligned} \quad (2.5)$$

This Hamiltonian represents two coupled oscillators: one is the gyrating ion and the other corresponds to the beat wave composed of the two electrostatic waves. We therefore can interpret ε as a coupling parameter between the two oscillators. The presence of this coupling parameter induces perturbations in the particle gyro motion. Physically, one can see that parameter ε is the normalized wave amplitude. Therefore, it makes sense that for a small wave amplitude the particle motion reduces to the simple gyration around a magnetic field line.

The detailed derivation of the analytical solution for a particle interacting with a single wave can be found in Ref. [28]. However, a more generalized solution for multiple waves is obtained in Refs. [3, 4] through Deprit's modified Lie transformation [43, 33, 44]. The details of this derivation are also given in Appendix C. The resulting autonomous Hamiltonian, derived from Eq. (2.5) to the second order in the perturbation strength, is

$$\begin{aligned} H = & \varepsilon\{J_{\nu_i}(\rho) \cos(\nu_i \vartheta) + J_{\nu_j}(\rho) \cos(\nu_j \vartheta)\} \\ & + \varepsilon^2\{S_1^{\nu_i}(\rho) + S_1^{\nu_j}(\rho) \\ & + S_6^{\nu_i, \nu_j}(\rho) \cos[(\nu_j - \nu_i) \vartheta]\}, \end{aligned} \quad (2.6)$$

where,

$$\begin{aligned}
S_1^{\nu_i}(\rho) &= \frac{1}{2\rho} \sum_{m=-\infty}^{\infty} \frac{m J_m(\rho) J'_m(\rho)}{\nu_i - m}, \\
S_6^{\nu_i, \nu_j}(\rho) &= \frac{1}{2\rho} \left(\sum_{m=-\infty}^{\infty} \frac{m J_m(\rho) J'_{\nu_j - \nu_i + m}(\rho)}{\nu_i - m} + \right. \\
&\quad \left. + \sum_{m=-\infty}^{\infty} \frac{m J_m(\rho) J'_{\nu_i - \nu_j + m}(\rho)}{\nu_j - m} \right), \tag{2.7}
\end{aligned}$$

J_m is the Bessel function of the first kind, and J' is the derivative of the Bessel function with respect to its argument. When ν_i is an integer, the summations are performed over all $m \neq \nu_i$ to avoid singularities. When ν is not an integer, the first-order terms in Eq. (2.6) disappear and equation becomes more tractable. This is one of the reasons why we choose to focus on the non-resonant cases.

It should be noted that θ and ϑ in Eqs. (2.5) and (2.6) are two distinct variables, and are related as $\vartheta = \theta - \tau$, as described in Appendix C. However, for the purposes of comparing numerical and analytical Poincaré sections they are equivalent, since both are periodic variables. Furthermore, ϑ appears inside the “cos” terms in Eq. (2.6), and the values of τ at the intersections with Poincaré sections are always an integer multiple of 2π . Therefore, in this dissertation all figures with Poincaré sections (analytic and numeric) are shown as ρ vs. θ without making the distinction between the two variables.

We now explore particle dynamics as a function of the normalized wave amplitude and frequency, and in terms of the location of critical points on the phase diagrams. Solving Eq. (2.5) numerically we will demonstrate that when critical points are absent in the regular region of the phase diagram (as in the single wave-particle interaction case), the particle will not gain net energy.

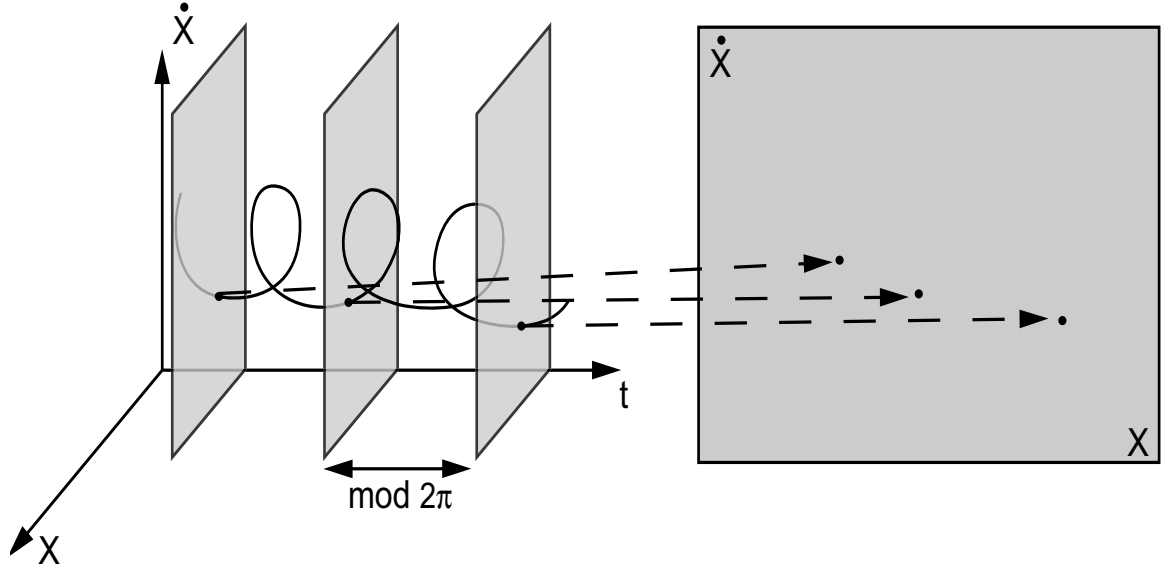


Figure 2.2: Construction of a Poincaré section. The intersections of the particle trajectory with the slices of $X - \dot{X}$ plane at a constant time interval are plotted together. If the motion is integrable, the points form a well-defined curve. If the motion is stochastic, the points are distributed randomly within some region on the Poincaré section.

2.4 Poincaré Section Construction

A convenient way of representing both numerical and analytical solutions of Eq. (2.1) is to plot the particle trajectories on a Poincaré section [31]. Poincaré sections are special types of phase diagrams that are very useful in analyzing periodic motion. A schematic illustrating construction of a Poincaré section is shown in Fig. 2.2. For a simple example of periodic motion one may think of a linear harmonic oscillator. To construct the Poincaré section for this example we follow the trajectory of the oscillator in three dimensional position-momentum-time ($X - \dot{X} - t$) space, shown in the left panel of Fig. 2.2. We then take slices of the $X - \dot{X}$ planes at some constant time intervals (usually $2\pi/\text{frequency} \text{ mod } 2\pi$) and collapse all the points where the trajectory intercepts the slices onto one 2-dimensional plot, as shown by the arrows and the right panel of Fig. 2.2. Thus, for the linear harmonic pendulum the points will form a circle if the frequency isn't an integer. If the frequency is an integer, then all the points on the Poincaré section will collapse to one. One may also think of a grandfather clock. If one snaps a picture of the pendulum every

second (i.e. once every period) then all pictures will show the pendulum to be in the same position.

The visual interpretation of Poincaré sections is straightforward. If the particle motion is integrable then all the intersection points will fall on some kind of well-defined curve on the Poincaré section. For example, circles and ellipses form close to the elliptic critical points, and hyperbolic lines form in the neighborhood of the hyperbolic critical points. On the other hand, when the particle motion is stochastic the points produce a random pattern.

To construct a Poincaré section from the numerical integration of Eq. (2.3) we plot the point intersections of the ion trajectory in three dimensions (ρ, θ, τ) with the ρ - θ plane at specific time intervals. For integer values of ν this reduces to plotting ρ vs. θ at $\tau = 2\pi j$, where $j = 0, 1, 2, \dots$ is a nonnegative integer. For noninteger values of ν the time interval is chosen according to the least common period of the waves. Since the magnetic field is constant, the normalized cyclotron radius ρ is a direct measure of the perpendicular ion velocity. Therefore Poincaré sections give direct visual insight into the acceleration process.

Poincaré sections can also be constructed from analytical solutions to the second-order approximations, given by Eq. (2.6). In constructing the Poincaré sections from the analytical solution we note that the Hamiltonian in Eq. (2.6) is autonomous (i.e. not a function of time τ), and therefore is an invariant of motion. Curves of constant H in a Poincaré section represent the complete analytical solution to second order. It should be noted that while the numerical solutions to Eq. (2.3) give “exact” answers, the Poincaré section obtained from Eq. (2.6) are the second-order approximations to the exact answer. For example, the analytical Poincaré sections do not show any stochastic behavior.

Poincaré sections obtained from numerical integration of Eq. (2.3) for the SEW and BEW cases are shown in Fig. 2.3b and Fig. 2.3d. It can be seen that for the SEW case trajectories below some ρ form a set of horizontal lines. These represent the particles that are not accelerated by the single electrostatic wave, as shown in Fig. 2.3a. Particles above

the threshold move stochastically.

When a particle undergoes an interaction with beating electrostatic waves the Poincaré section looks fundamentally different than that in the SEW case. Now some particles with arbitrary low initial velocity are accelerated by the BEW first through integrable motion and then stochastic, as shown in Fig. 2.3c and d.

We also observe an elliptic point at $(\rho, \theta) \sim (\nu/2, \pi)$ in Fig. 2.3d. Critical points define the local dynamics of the particle motion. Since the system is not dissipative, we expect to find two types of critical points on the Poincaré section: elliptic and hyperbolic. As we shall show later, the location of the critical points is key to determining which initial conditions lead to acceleration or trapping in the BEW case. Defining the criteria for stochastic acceleration therefore reduces to finding critical points. Our research is guided by a comparison of the Poincaré sections obtained from the analytical solution and those from numerical integration of Eq. (2.5). Again we note that analytical solution will not display any stochastic behavior because Eq. (2.6) is a second-order approximation to the exact solution.

2.5 Single-Wave Interaction

In this section, in order to create a context for our study, we summarize the results obtained by Karney [28] for the interaction of a magnetized particle with a single electrostatic wave. Using the first-order perturbation theory Karney [1, 28] was able to derive analytical expressions approximating the overall nonlinear dynamics of the ion motion. He showed that stochastic motion occurs when the wave amplitude exceeds a certain threshold. The work also revealed a threshold in the initial ion velocity below which a particle cannot gain net energy from the single electrostatic wave. These two threshold conditions can be expressed

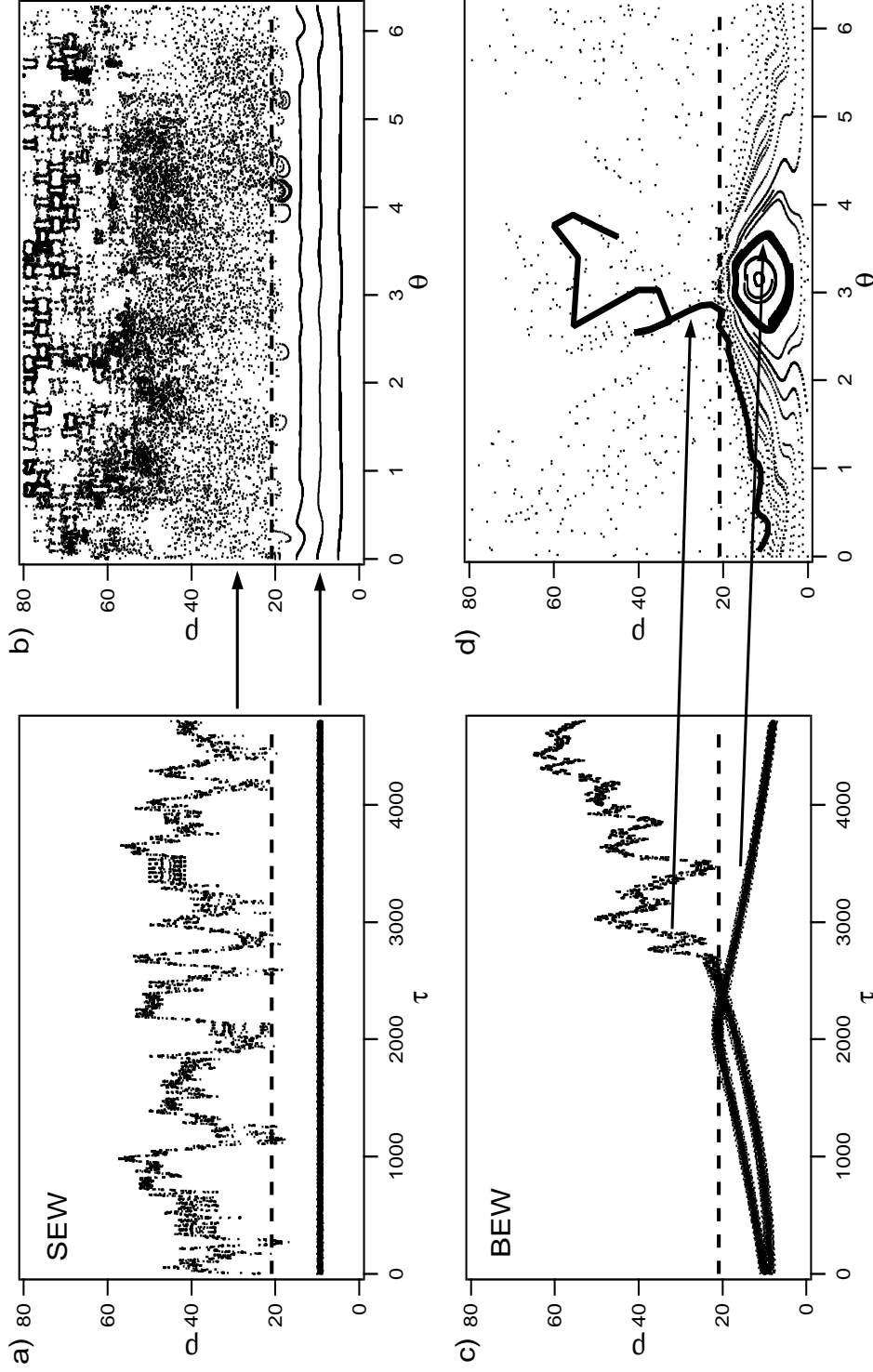


Figure 2.3: Time evolution of the normalized Larmor radius ρ and Poincaré sections showing numerical solutions to Eq. (2.3) for a single particle interacting with: **a)** and **b)** single electrostatic wave with $\varepsilon = 10$, $\nu = 24.3$, and **c)** and **d)** beating electrostatic waves with $\varepsilon = 10$, $\nu_1 = 24.3$, $\nu_2 = 25.3$. The threshold, given by Eq. (2.10), represents the boundary between the regular and stochastic domains and is shown as a horizontal thick dashed line. Ions below this threshold are unaffected by the single wave but may be accelerated by beating electrostatic waves.

in terms of the wave electric field and the ion velocity as

$$E/B = \frac{1}{4}(\omega_{ci}/\omega)^{1/3}(\omega/k_{\perp}), \quad (2.8a)$$

$$v = \frac{\omega}{k_{\perp}} - \sqrt{\frac{qE}{k_{\perp}m_i}}, \quad (2.8b)$$

where v, m_i, q and ω_{ci} are the velocity, mass, charge, and the cyclotron frequency of the ion, and ω, k_{\perp} and E are the frequency, wavenumber, and electric field amplitude of the wave. The normalized version of the above equations is expressed as

$$\varepsilon = \nu^{2/3}/4, \quad (2.9)$$

$$\rho = \nu - \sqrt{\varepsilon}. \quad (2.10)$$

Skiff *et al.* validated the wave amplitude threshold experimentally [17]. The significance of the wave amplitude threshold is clear. To produce stochastic acceleration, i.e. resonance overlapping, the wave amplitude needs to be high enough to produce the nonlinear behavior. The significance of the velocity threshold can be understood from a simple surfer analogy that illustrates the physical meaning of the threshold as a velocity resonance condition.

To ride an ocean wave a surfer laying on his board needs to start paddling toward the beach as the wave is about to overtake him. If the surfer does not paddle then the wave will pass him by without producing the desired acceleration. This is similar to stochastic ion acceleration by a single electrostatic wave, where an ion needs to be moving at a certain minimum velocity to be accelerated by the wave.

This idea is demonstrated in Fig. 2.3a. The figure shows the velocity evolution of two test ions interacting with SEW ($\varepsilon = 10, \nu = 24.3$), which is obtained through the numerical evaluation of Eq. (2.3). Below the velocity threshold, indicated by the horizontal dashed line, we observe that the ion motion is regular, and consequently we can predict

its behavior well by means of the perturbation theory. More importantly, as long as the ion's initial velocity is in that region the ion does not gain net energy from the wave [28]. When the initial velocity of the ion is above the threshold, the ion moves stochastically, and on average gains net energy, as shown by the upper trajectory in Fig. 2.3a. Thus, the velocity threshold separates two regions of phase space: the *regular* motion region of low energies below the threshold and the *stochastic* one – above the threshold. An important observation is that an ion gains energy from a single electrostatic wave only through the stochastic motion, when its initial velocity exceeds the threshold.

On the other hand, as shown in Fig. 2.3c, ions may be accelerated from below the single-wave threshold into the stochastic acceleration region by beating electrostatic waves. The figure shows particles interacting with two beating electrostatic waves ($\varepsilon = 10, \nu_1 = 24.3, \nu_2 = 25.3$). The two particles are initially below the single-wave threshold, and gyrate at the same Larmor radius, $\rho = 1$, but have different initial phase angles, θ . While the trajectory of one of the particles remains below the velocity threshold, just like in the SEW case, the second particle can be accelerated to high velocities through the single-wave threshold. Describing this complicated behavior is the key to understanding the beating wave acceleration mechanism.

2.6 Multi-Wave Interaction

The first hint of the BEW ion acceleration mechanism came from an investigation of two ES waves interacting with a single ion conducted by Chia *et al.* [33] in 1996. They noticed that for the waves with even-even or odd-odd combinations of frequencies, ν , there existed a mechanism that allowed some ions to move through the stochastic web region of the phase space to high values of ρ , allowing “infinite” ion acceleration. In 1998 Benisti *et al.* [3, 4] determined a beating condition under which two electrostatic waves can pick a low-energy ion and transport it through the single-wave velocity threshold into the stochastic

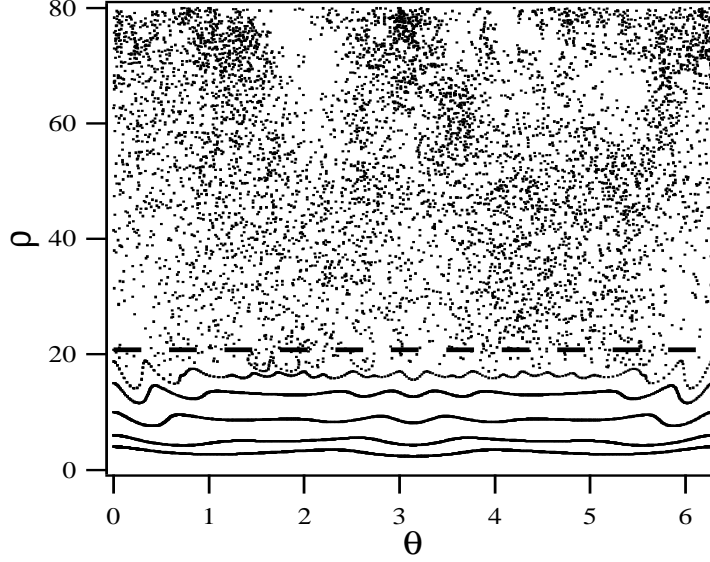


Figure 2.4: Poincaré section showing numerical solutions for a particle interacting with two non-beating waves ($\varepsilon = 10$, $\nu_1 = 24$, $\nu_2 = 25.5$). Particles with initial velocity below the single-wave threshold defined by Eq. (2.10), shown as a dashed line, do not gain energy from the waves. This picture is qualitatively similar to the SEW interaction shown in Fig. 2.3b.

acceleration region, where it can be further accelerated by the waves. They demonstrated this condition to be

$$\nu_j - \nu_i = n, \quad (2.11)$$

where n is an integer. The equation above amounts to the wave beating condition. We will shortly show that Eq. (2.11) specifies necessary but not sufficient condition for particle acceleration from below the single-wave threshold given by Eq. (2.10).

2.6.1 Multiple Non-beating Waves

We start studying the particle interaction with multiple waves by demonstrating the importance of the beating criteria derived by Benisti *et al.*. Figure 2.4 shows a typical Poincaré section obtained by solving Eq. (2.3) numerically for $\varepsilon = 10$, $\nu_i = 24$, and $\nu_j = 25.5$, i.e. when Eq. (2.11) does not hold. The Poincaré section is qualitatively very similar to that of

the single wave-particle interaction shown in Fig. 2.3b. The ions with energies below the single-wave threshold do not gain energy.

The particle interaction with the “almost” beating waves such that $\nu_2 - \nu_1 = n + \delta\nu$, where $\delta\nu$ is small, was briefly discussed by Benisti *et al.* in Ref. [3]. They showed the Hamiltonian (2.6) is transformed in this case into

$$\begin{aligned}
H(\nu_i - \nu_j \neq n) = & \varepsilon \{ J_{\nu_i}(\rho) \cos(\nu_i \vartheta) + J_{\nu_j}(\rho) \cos(\nu_j \vartheta) \} \\
& + \varepsilon^2 \{ S_1^{\nu_i}(\rho) + S_1^{\nu_j}(\rho) \\
& + S_6^{\nu_i, \nu_j}(\rho) \cos[(\nu_j - \nu_i) \vartheta] + S_6^{\nu_i, \nu_j}(\rho) \cos[n \vartheta - \delta\nu \tau] \}. \quad (2.12)
\end{aligned}$$

The equation above is non-autonomous and thus does not have analytical solutions. Numerical investigation of these cases is also difficult because the least common period becomes longer and longer as $\delta\nu$ approaches 0 and, hence it takes longer to construct a Poincaré section. In order to investigate how close the two frequencies should be to produce the stochastic acceleration of the low-energy ions we conducted a numerical study by decreasing $\delta\nu$ from 0.5 to 0.05. Figure 2.5 shows an example with $\varepsilon = 10$, $\nu_1 = 24.3$, and $\nu_2 = 25.35$. The figure demonstrates that the beating criterion given by Eq. (2.11) is very strict, and for $\delta\nu$ as low as 0.05 the two wave interaction is qualitatively similar to the single-wave interaction.

We further study the beating wave criterion by investigating the beat order n . Poincaré sections obtained from the analytical solution to Eq. (2.6), as well as numerical solution to Eq. (2.1) for $n = 2$ are shown in Fig. 2.6. These figures demonstrate that for n as low as 2 the two-wave interaction is qualitatively similar to the single-wave interaction, and only the particles above the $\rho = \nu - \sqrt{\varepsilon}$ threshold are stochastically accelerated. Therefore, we conclude that a particle with an arbitrary small initial velocity can only be

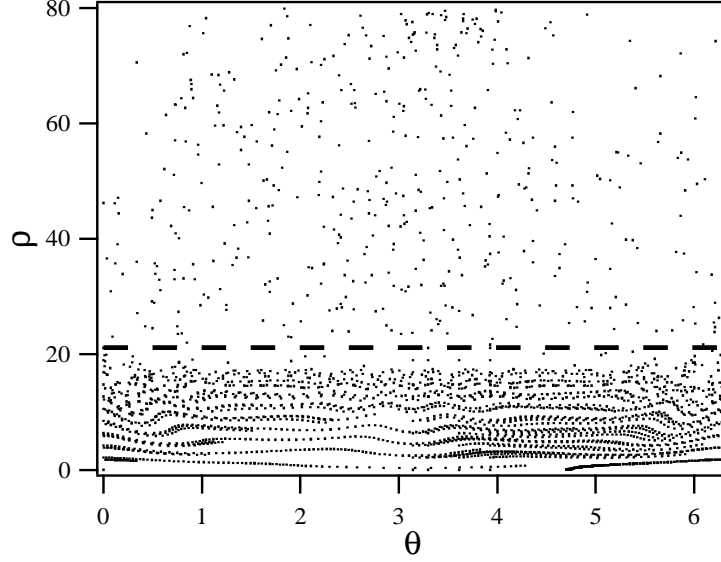


Figure 2.5: Poincaré section showing numerical solutions for a particle interacting with two “almost” beating waves ($\varepsilon = 10$, $\nu_1 = 24.3$, $\nu_2 = 25.35$). Similarly to the non-beating case, the particles with initial velocity below the threshold (dashed line) do not gain energy from the waves. The beating wave acceleration mechanism is destroyed for small $\delta\nu$.

accelerated by two beating waves such that

$$\nu_1 - \nu_2 = 1.$$

Consequently, we limit our investigations of the BEW interaction to that condition.

2.6.2 Two Beating Waves

We now gauge how well the second-order perturbation analysis compares to the numerical solutions. Figure 2.7 shows the Poincaré sections obtained by plotting the curves of constant H from Eq. (2.6) (panel a) and through numerical integration of Eq. (2.3) (panel b) for $\varepsilon = 10$, $\nu_1 = 24.3$, and $\nu_2 = 25.3$. The comparison indicates a good degree of agreement between the two Poincaré sections. Even though the detailed structure of the regular motion curves is not captured by the analytical solution, the latter does predict the position of the lower elliptic point (**E**) as well as the hyperbolic point (**H**) rather well. On the other

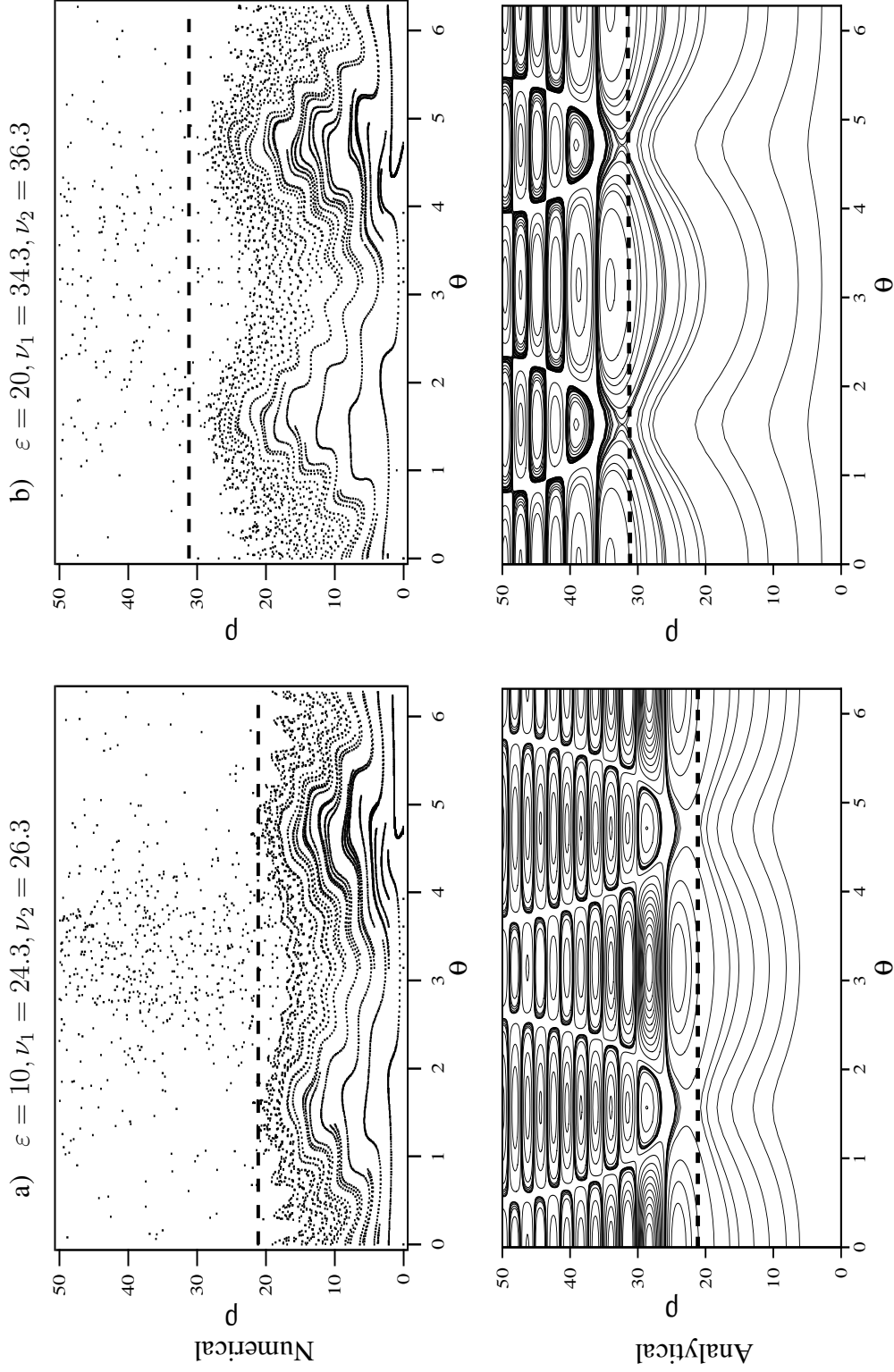


Figure 2.6: Poincaré sections obtained through numerical integration of Eq. (2.3) (top), and by plotting the curves of constant H of Eq. (2.6) (bottom). The plots indicate that for $\nu_1 - \nu_2 = 2$ the particle dynamics is qualitatively similar to the case of SEW interaction. The single-wave threshold is shown by the horizontal dashed lines.

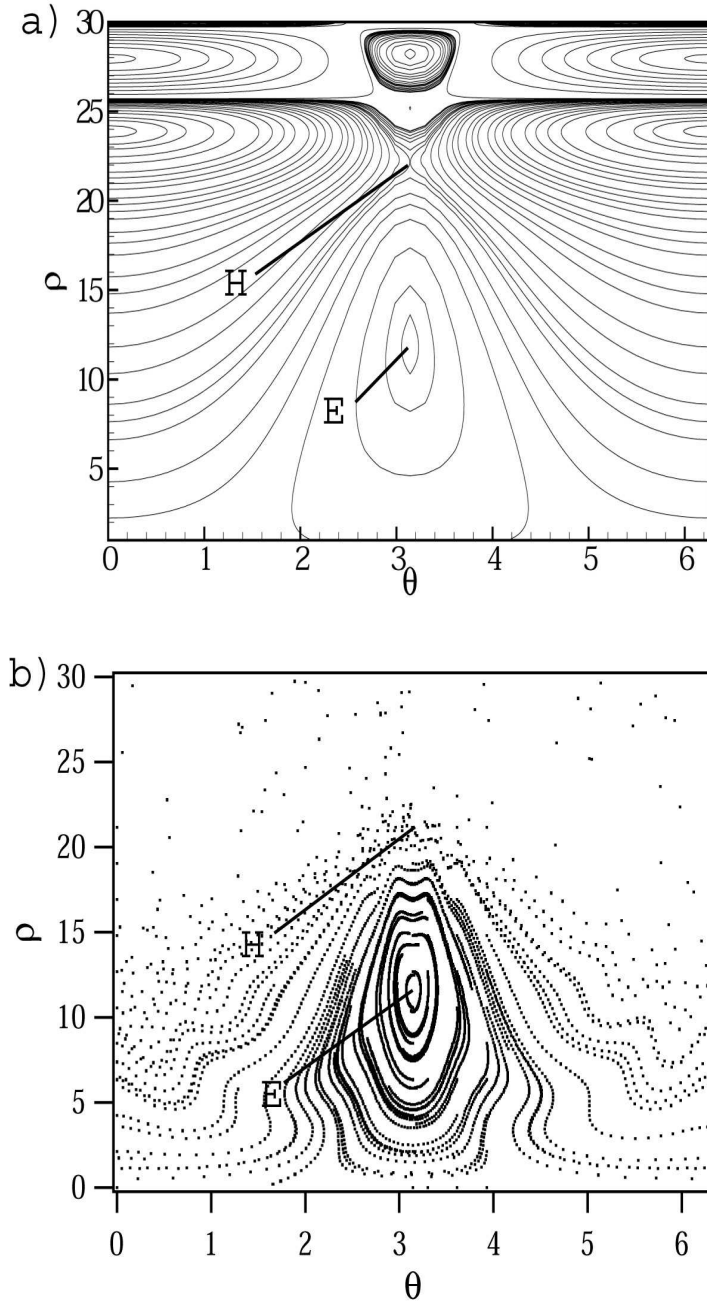


Figure 2.7: Poincaré section for a particle interacting with two beating waves. a) Analytical solution showing the existence of hyperbolic and elliptic points marked by **H** and **E** respectively. b) Numerical solution also showing the critical points. $\varepsilon = 10$, $\nu_1 = 24.3$, $\nu_2 = 25.3$.

hand, our analytical approach breaks down in the stochastic region, as should be expected. However, as described in Ref. [4], even in that region of phase space the overall ion motion could be analytically approximated by the first-order orbits, for small ε .

We now see that the beating wave interaction with the low-energy particles can be directly associated with the presence of the elliptic point **E** in the regular acceleration region, and its counterpart, the hyperbolic point **H**, at the junction with the stochastic region. It is clear by tracing trajectories emanating from the hyperbolic point and those that surround the elliptic point in Fig. 2.7a that these two critical points bound the region where the low-energy ions do not experience the stochastic acceleration. Instead their trajectories circulate around the elliptic critical point **E** or cover the full range of cyclotron phase angles ($0 \leq \theta \leq 2\pi$) while remaining below point **H**.

Another way of describing the bound region is to make a three-dimensional plot, as shown in Fig. 2.10a. We see that the bound region is a “potential well”. The extent of the well can be found by determining the position of the two critical points. We note that both points lie at $\vartheta = \pi$. Figure 2.11 shows the Hamiltonian determined from Eqs. (2.6) and (2.7) as a function of ρ for $\vartheta = \pi$, and illustrates that the location of the elliptic and the hyperbolic points could be found by determining the local minimum and the maximum of the Hamiltonian H using Eq. (2.6).

Therefore, for given values of ν and ε , the inequality

$$H_E < H(\rho_0, \vartheta_0) < H_H, \quad \text{with } \rho_0 < \nu - \sqrt{\varepsilon} \quad (2.13)$$

defines the *forbidden acceleration domain*. Here H_E and H_H are the Hamiltonian values for the elliptic (**E**) and the hyperbolic (**H**) points, and the subscript “0” refers to initial conditions. By “forbidden acceleration domain” we mean the domain of initial conditions for which an ion cannot reach the stochastic region of phase space. This restriction shows that not all ions can be accelerated by the waves, even when the beating criterion (2.4) is

satisfied. All other ion trajectories then lie in the *allowed acceleration domain* of phase space. The ions in the allowed acceleration domain are affected by the waves strongly. The forbidden and allowed acceleration regions are schematically illustrated in Fig. 3.1b

The “trapping” criterion in Eq. (2.13) given in terms of the Hamiltonian should be contrasted with the threshold criterion for interaction with a single wave, given by Eq. (2.8b). It is clear that, unlike the single-wave case, an ion with initial velocity ρ_o below the “threshold” can still be accelerated to high energies if the corresponding Hamiltonian is outside the range described by Eq. (2.13)

The physical implication of Eq. (2.13) to a real plasma experiment is this: by selecting the appropriate wave and plasma parameters we can limit the number of particles trapped in the forbidden acceleration domain ($H_E < H(\rho_o, \vartheta_o) < H_H$). Ions outside of this region gain much higher energies through first regular (if their initial velocity is low) and then stochastic acceleration. However, even the trapped particles can escape into the stochastic domain when collisional effects are introduced. We will explore this aspect in the next chapter.

2.6.3 ε Dependence

In Fig. 2.8 we show typical Poincaré sections obtained by numerical integration of Eq. (2.3) with $\nu_1 = 24.3$ and $\nu_2 = 25.3$. The panels in this figure illustrate the effect of increasing wave amplitude. For low perturbation strength (low values of ε) the regular region extends to the values of ρ approximately predicted by the single-wave threshold, which is given by Eq. (2.10). However, as ε is increased the stochastic acceleration region extends to ever lower values of ρ , and the regular acceleration region quickly shrinks to the vicinity of the elliptic critical point. Notice that the location of the elliptic point **E** does not change. Eventually, as the wave amplitude is raised above the values shown on Fig. 2.8, stochastic motion dominates the Poincaré section, and the forbidden acceleration region disappears completely.

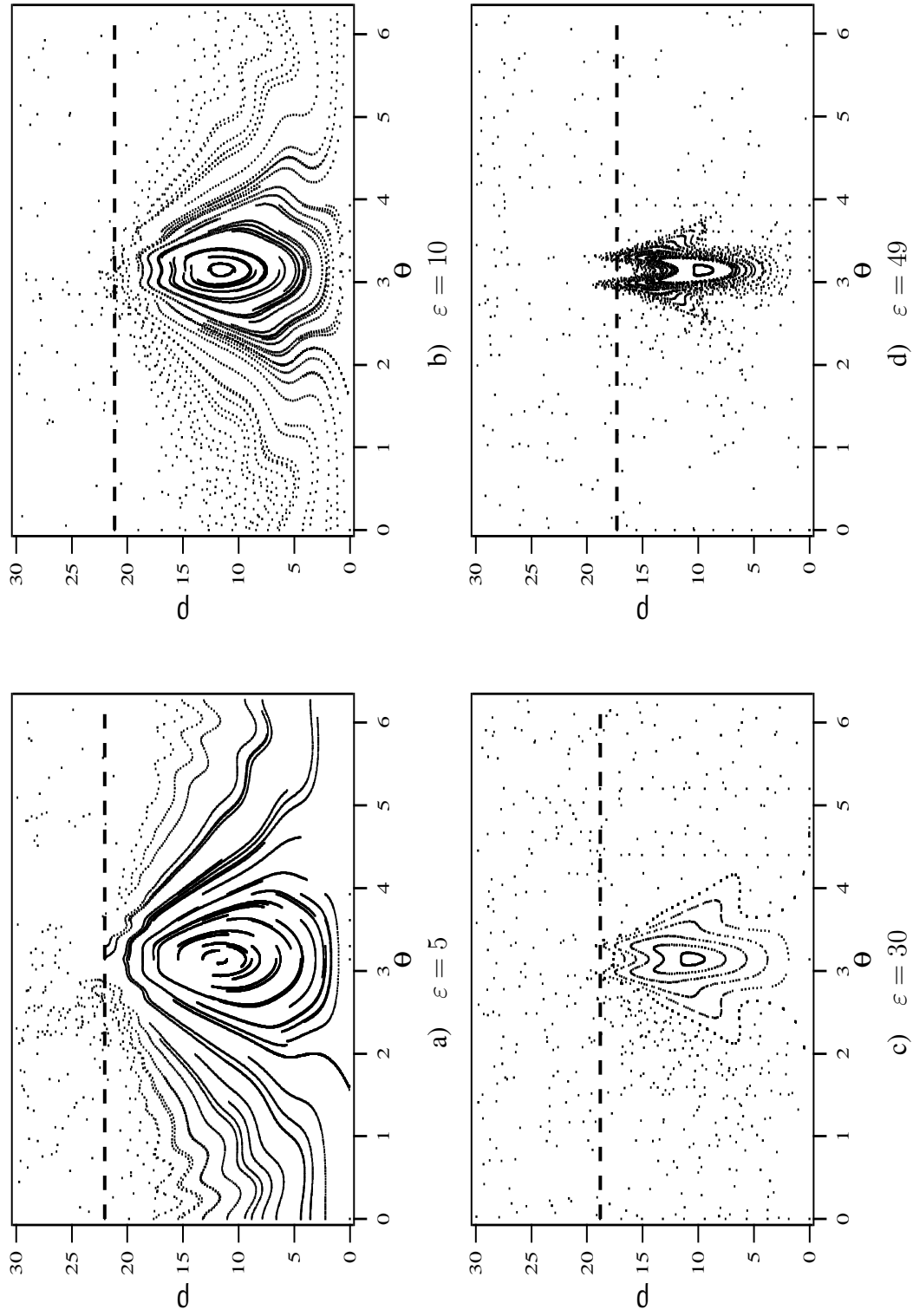


Figure 2.8: Poincaré sections showing numerical solutions for a particle interacting with two beating waves ($\nu_i = 24.3$, $\nu_j = 25.3$). The stochastic acceleration region occupies a greater fraction of the phase space, and reaches to the lower values of ρ as the wave amplitude is increased. The single-wave threshold is shown by the horizontal dashed lines.

In other words, as the wave amplitude increases more ions are accelerated by the beating waves, which makes sense physically. As we will demonstrate in Chapter 3 the maximal energy obtained by a system of particles, i.e. temperature, is a strong function of the wave amplitude.

2.6.4 ν Dependence

The wave frequency ν plays a more complicated role in the particle dynamics than the wave amplitude ε . In Fig. 2.9 we demonstrate the changes in the Poincaré section as ν is varied from 14.3 to 44.3 (for $\varepsilon = 10$). The four panels in the figure show that the entire phase space scales with ν . For example, as will be shown in the next section, the vertical coordinate of the hyperbolic and elliptic points varies as ν and $\nu/2$ respectively.

The extent of the regular acceleration region also scales with ν . However, this dependence is not as straightforward as might seem initially. For instance, panel a) in Fig. 2.9 shows that the stochastic domain reaches below the elliptic point for $\nu_{1,2} = 14.3, 15.3$ while the regular region in Fig. 2.9d ($\nu_{1,2} = 44.3, 45.3$) reaches up to the SEW velocity threshold value of $\nu - \sqrt{\varepsilon}$. This behavior can be understood from Eq. (2.9), which describes the wave amplitude threshold. Computations of Eq. (2.9) for the four panels in Fig. 2.9 show that for $\varepsilon/\nu^{2/3} < 1$ the regular acceleration region extends up to the single-wave threshold, while for $\varepsilon/\nu^{2/3} > 1$ the stochastic acceleration region reaches to lower values of ρ . The topic of the ion heating dependance on the wave frequency will be further picked up in the next chapter.

2.7 Critical Points

To define the domains of allowed and forbidden acceleration described by Eq. (2.13) we need to find the location of the critical points **E** and **H**. We now seek analytical expressions for both. Since both points are extrema of the Hamiltonian, given by Eq. (2.6), their loca-

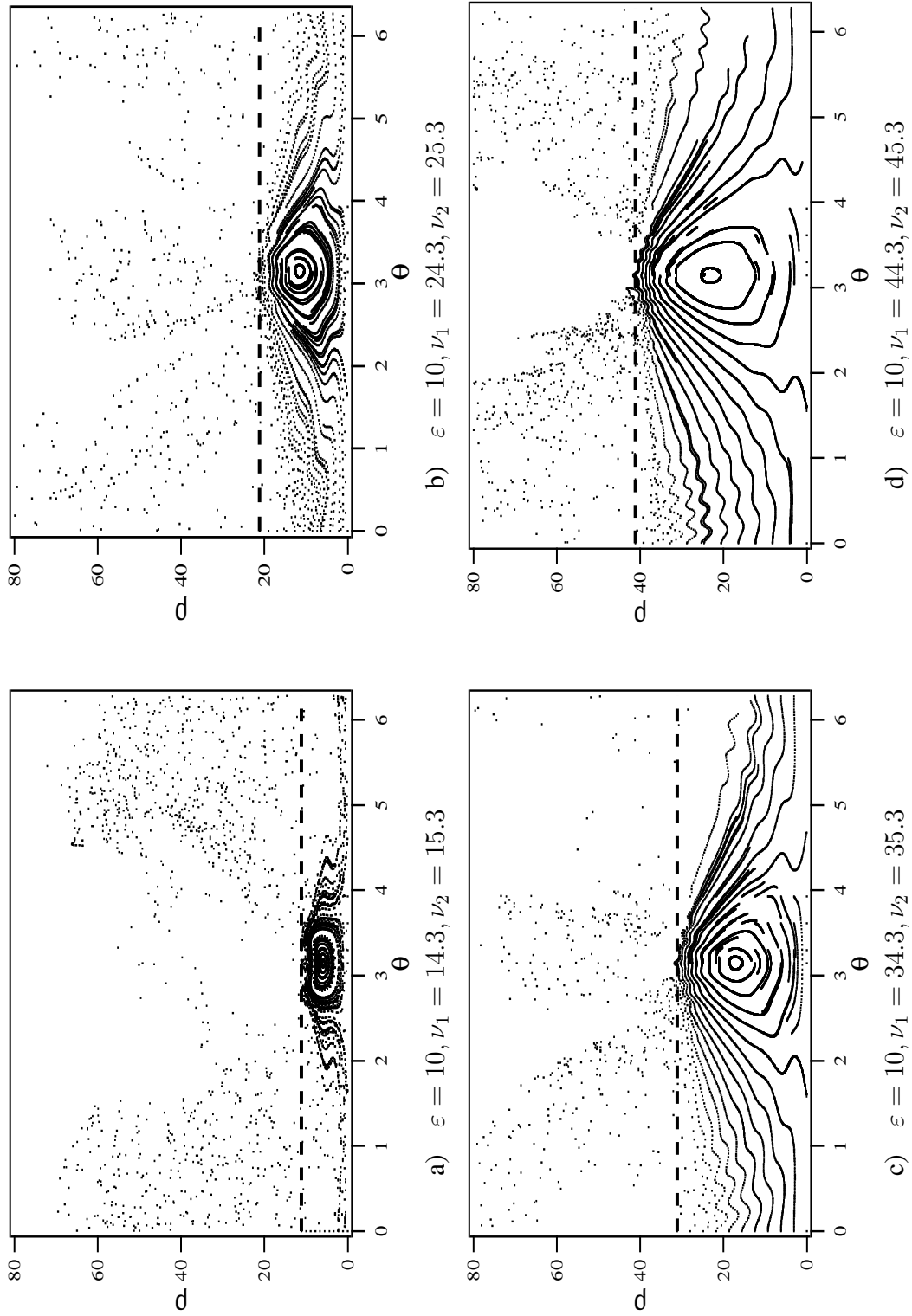


Figure 2.9: Poincaré sections obtained for various frequencies of beating electrostatic waves. The four panels indicate that the vertical position of the elliptic and hyperbolic points depends linearly on the wave frequency ν . Thus, the area occupied by the regular acceleration region also increases with ν for a given ε . The single-wave threshold is shown by the horizontal dashed lines.

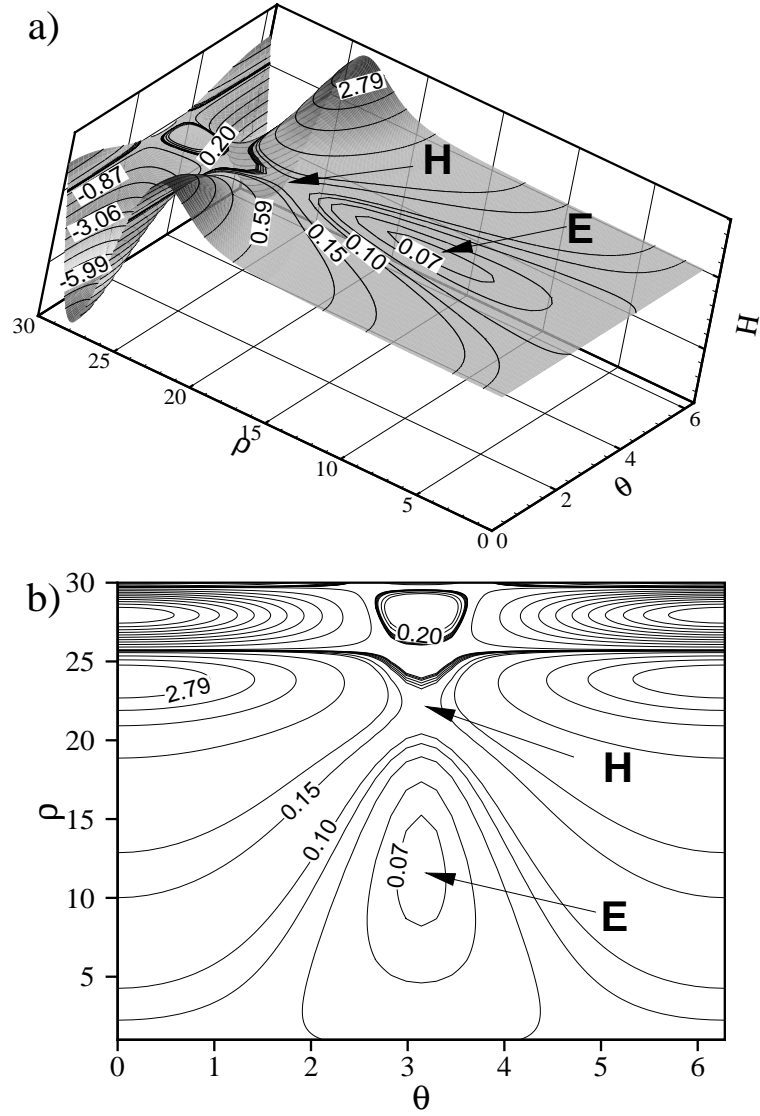


Figure 2.10: a) Three dimensional representation of the analytical Poincaré section shown in panel b). A potential well bounding the forbidden acceleration region can be described by the positions of critical points **E** and **H**. $\varepsilon = 10$, $\nu_i = 24.3$, $\nu_j = 25.3$.

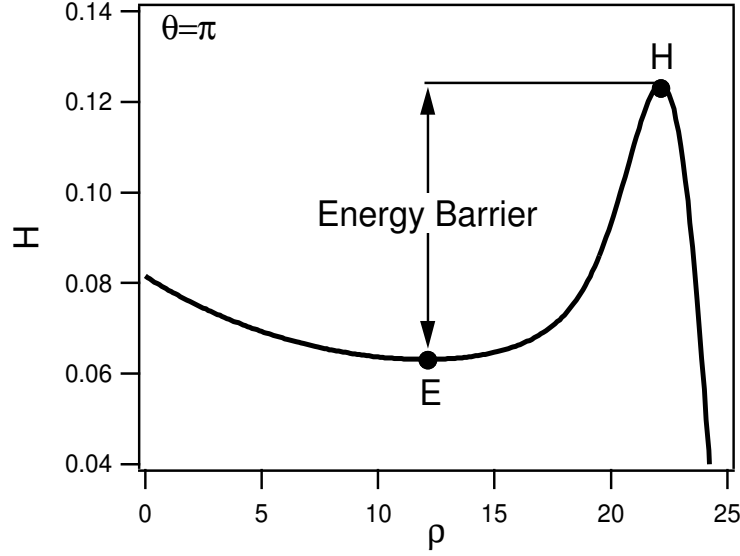


Figure 2.11: Analytical Hamiltonian as a function of ρ at $\vartheta = \pi$. The elliptic and the hyperbolic points corresponding to the ones shown in Fig. 2.10 are the minimum and the maximum of H . $\nu_i = 24.3$, $\nu_j = 25.3$.

tions can be found by setting the time derivative of ρ and ϑ to zero simultaneously [31, 45].

Utilizing the Hamilton's equations of motion in conjunction with Eqs. (2.6) and (2.7) we get

$$\dot{\rho} = -\frac{\partial H}{\partial \vartheta} = \varepsilon \{ \nu_i J_{\nu_i}(\rho) \sin(\nu_i \vartheta) \quad (2.14)$$

$$+ \nu_j J_{\nu_j}(\rho) \sin(\nu_j \vartheta) \}$$

$$+ \varepsilon^2 (\nu_i - \nu_j) S_6^{\nu_i, \nu_j}(\rho) \sin[(\nu_j - \nu_i) \vartheta] = 0,$$

$$\dot{\vartheta} = \frac{\partial H}{\partial \rho} = \varepsilon \{ J'_{\nu_i}(\rho) \cos(\nu_i \vartheta) \quad (2.15)$$

$$+ J'_{\nu_j}(\rho) \cos(\nu_j \vartheta) \}$$

$$+ \varepsilon^2 \{ S_1'^{\nu_i}(\rho) + S_1'^{\nu_j}(\rho) \}$$

$$+ S_6'^{\nu_i, \nu_j}(\rho) \cos[(\nu_i - \nu_j) \vartheta] \} = 0.$$

When both wave frequencies are off-resonance ($\nu_i, \nu_j \neq \text{integer}$), the equations above simplify because the first-order terms are absent (see Appendix C), and we can obtain the

position of critical points analytically. For integer values of ν the position of the elliptic point can also be computed with these equations.

Before we proceed to evaluate the positions of critical points we need to simplify the expression for the Hamiltonian. For $\nu \neq \text{integer}$, the $S_1^{\nu_i}(\rho)$ term in Eq. (2.7) could be simplified to an algebraic expression containing only a few Bessel functions of the first kind [33],

$$\begin{aligned} S_1^{\nu_i}(\rho) &= \frac{\pi}{8 \sin \nu_i \pi} [J_{\nu_i+1}(\rho) J_{-(\nu_i+1)}(\rho) \\ &\quad - J_{\nu_i-1}(\rho) J_{-(\nu_i-1)}(\rho)]. \end{aligned} \quad (2.16)$$

As a result of this simplification we can reduce the $S_6^{\nu_i, \nu_j}(\rho)$ term down to

$$S_6^{\nu_i, \nu_j}(\rho) = \frac{\rho}{\nu_i} S_1^{\nu_i}(\rho) + \frac{\rho}{\nu_j} S_1^{\nu_j}(\rho). \quad (2.17)$$

The details of this derivation are given in Appendix D. We can therefore express the Hamiltonian given by Eq. (2.6) in terms of $S_1^{\nu_i}(\rho)$ only,

$$\begin{aligned} H &= \varepsilon^2 \left\{ \left(1 + \frac{\rho}{\nu_i} \cos[\nu_i - \nu_j] \vartheta \right) S_1^{\nu_i}(\rho) \right. \\ &\quad \left. + \left(1 + \frac{\rho}{\nu_j} \cos[\nu_i - \nu_j] \vartheta \right) S_1^{\nu_j}(\rho) \right\}. \end{aligned} \quad (2.18)$$

As we will show later, our analysis breaks down for small values of ν . Consequently we take $\nu_i \gg 1$, and remembering that $n = 1$, we approximate $\rho/\nu_i \sim \rho/\nu_j$. Dropping the subscripts in $S_1^{\nu_i}(\rho)$ we have

$$\begin{aligned} H &= \varepsilon^2 \left[1 + \frac{\rho}{\nu_i} \cos(\nu_i - \nu_j) \vartheta \right] \times \\ &\quad \left[S^{\nu_i}(\rho) + S^{\nu_j}(\rho) \right]. \end{aligned} \quad (2.19)$$

Finally, we substitute Eq. (2.16) for each of the $S_1^{\nu_i}(\rho)$ functions. Expressing everything in

terms of ν_i we get

$$H = \frac{\varepsilon^2 \pi}{8 \sin \nu \pi} \left(1 + \frac{\rho}{\nu} \cos \vartheta \right) \quad (2.20)$$

$$\left[\begin{aligned} & - J_{\nu-1}(\rho) J_{-(\nu-1)}(\rho) + J_{\nu}(\rho) J_{-\nu}(\rho) \\ & + J_{\nu+1}(\rho) J_{-(\nu+1)}(\rho) - J_{\nu+2}(\rho) J_{-(\nu+2)}(\rho) \end{aligned} \right],$$

where we have replaced ν_i with ν .

This simplified expression allows us to calculate the position of points **E** and **H**. From Eq. (2.14) (as well as from Fig. 2.7) we see that both critical points lie at $\vartheta = \pi$. This reduces Eqs. (2.14) and (2.15) to one equation

$$\frac{\partial}{\partial \rho} \left\{ \left(1 - \frac{\rho}{\nu} \right) L(\rho) \right\} = 0, \quad (2.21)$$

where

$$\begin{aligned} L(\rho, \nu) &= -J_{\nu-1}(\rho) J_{-(\nu-1)}(\rho) + J_{\nu}(\rho) J_{-\nu}(\rho) \\ &+ J_{\nu+1}(\rho) J_{-(\nu+1)}(\rho) - J_{\nu+2}(\rho) J_{-(\nu+2)}(\rho). \end{aligned}$$

From Eq. (2.21) we can express ρ as a function of $L(\rho)$ and $L'(\rho)$, where prime denotes the derivative with respect to ρ , and arrange the resulting expression as

$$\frac{\rho}{\nu} = 1 - \frac{1}{\nu} \frac{L(\rho, \nu)}{L'(\rho, \nu)}, \quad (2.22)$$

or

$$F(\rho, \nu) \equiv 1 - \frac{\rho}{\nu} - \frac{1}{\nu} \frac{L(\rho, \nu)}{L'(\rho, \nu)} = 0. \quad (2.23)$$

The first and second roots of Eq. (2.23), ρ_E and ρ_H , for a given value of ν , correspond to

the locations of the *elliptic* and *hyperbolic* points respectively.

The solution to Eq. (2.15) is plotted as a function of ρ/ν for $\nu \in [55.001, 55.999]$ in Fig. 2.12. It is now important to discuss the behavior of these solutions. As we discussed above, we are only considering the cases with $\nu \neq \text{integer}$. Unfortunately, due to the asymptotic behavior of the Bessel function near the “turning point” [46], defined as $\rho_{tp} = \sqrt{\nu(\nu+1)}$, the solution approaches different limits as ν gets close to an integer from different sides. Therefore, no simple analytical expression could be obtained for the position of the hyperbolic point. Instead, Fig. 2.13 shows a range of solutions for the location of this point. On the other hand, the elliptic point is very well defined. It can be seen that for sufficiently large values of ν the location of the elliptic point, according to our second-order perturbation analysis is at

$$\rho_E \simeq \frac{\nu}{2}, \quad \vartheta_E = \pi. \quad (2.24)$$

Although no simple expression could be found for the location of the hyperbolic point, we see from Fig. 2.13 that its location asymptotes (at large values of ν) to a value of $\rho/\nu \sim (0.8 - 1.0)$, therefore we may approximate

$$\rho_H \simeq 0.9\nu, \quad \vartheta_H = \pi. \quad (2.25)$$

It is also important to mention that because of the asymptotic behavior of the Bessel functions, the elliptic and hyperbolic points could not always be found for small values of ν . For these cases while the expression for the Hamiltonian, Eq. (2.20), is still valid, our analysis of the allowed and forbidden acceleration domains does not apply.

Another limitation is placed on our analysis by its independence on ε in locating the critical points, as seen from Eq. (2.21). Extensive ($\varepsilon = 5 - 100$, $\nu = 10 - 50$) numerical exploration of the weak dependence of the critical point locations on ε suggests the follow-

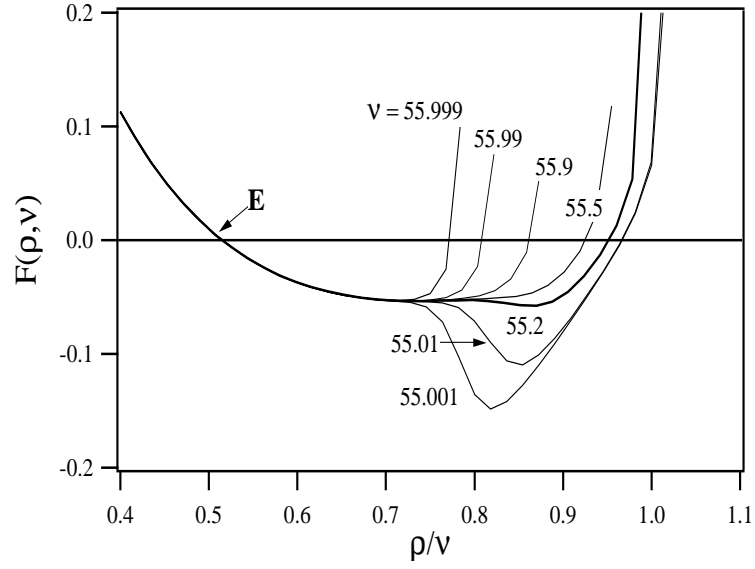


Figure 2.12: Plot of the function $F(\rho, \nu)$, given by Eq. (2.23), showing how the second root (corresponding to the hyperbolic point) moves away from $\rho/\nu = 1$ as ν changes from 55.001 to 55.999. The first root on the left, marked **E**, represents the elliptic point and the subsequent roots represent the hyperbolic points for the various values of ρ/ν .

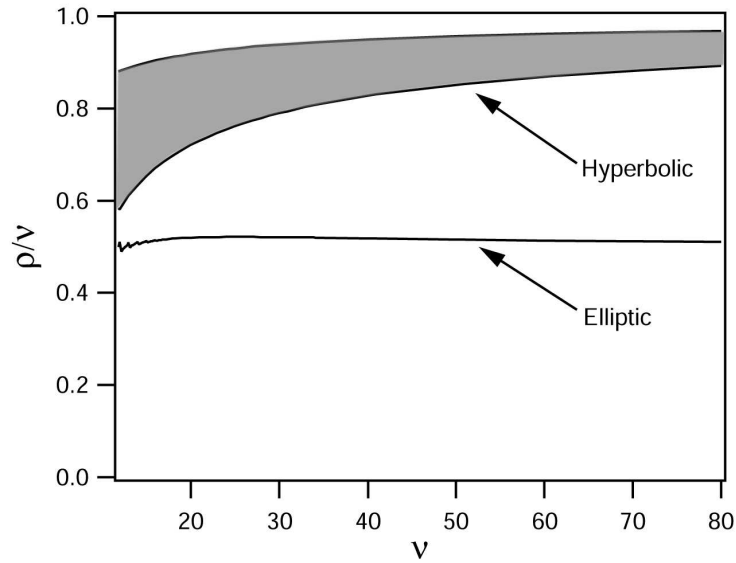


Figure 2.13: Solution to Eq. (2.22) as a function of ν . The range of positions for point **H** (gray region) increases for small ν . In addition the elliptic and hyperbolic points, **E** and **H**, could not always be found for $\nu < 9$.

ing corrections to expressions (2.24) and (2.25), which are reminiscent of the ε dependence in the single wave interaction [28] given by Eq. (2.10),

$$\rho_E \simeq \frac{(\nu - \sqrt{\varepsilon})}{2}, \quad \vartheta_E = \pi, \quad (2.26a)$$

$$\rho_H \simeq \nu - \sqrt{\varepsilon}, \quad \vartheta_H = \pi. \quad (2.26b)$$

The physical interpretation and significance of these two points may be understood as follows. As was discussed earlier, the difference in the Hamiltonian of the two points can be thought of as an “energy barrier”, which an ion must overcome to be accelerated by the wave. Another way to understand the importance of the two critical points is to realize that at the elliptic point the energy exchange between the ion and the waves is at the minimum. This is equivalent to a stable equilibrium for a pendulum. Any small perturbation from that equilibrium will only cause small oscillations about it. This implies that in the immediate neighborhood of point **E** the ion energy cannot be altered sufficiently to push the ion into the stochastic region, as seen in Fig. 2.10. On the other hand, the hyperbolic point corresponds to the unstable equilibrium of the pendulum and any small perturbation from it will cause significant changes in the ion motion, i.e. escape into the stochastic region and subsequent vigorous acceleration.

2.8 Particle Motion in the Regular Acceleration Region

Numerical solutions of Eq. (2.5) for various wave frequencies indicate that particle acceleration in the regular acceleration region is approximately constant, as shown in Fig. 2.14a and b. The solid curve, $\rho(\tau)$, in Fig. 2.14a was obtained with the following initial conditions for the particle velocity and phase angle: $(\rho_0, \theta_0) = (1, 0)$. These initial conditions place the particle in the lower left corner of the Poincaré section at $\tau = 0$, as can be seen from Fig. 2.3c and d as well as Fig. 2.15. Trajectories in the regular acceleration region of the BEW Poincaré section move clockwise around the elliptic point. In other

words, trajectories to the left of the elliptic point result in net particle acceleration, while those to the right of the elliptic point result in net particle deceleration. We can thus see that the particle acceleration in the regular acceleration region, shown in Fig. 2.14a and b, depends, in part, on the choice of the initial conditions.

Using Eq. (2.14), with the simplifications made in Eq. (2.20), it is possible to derive analytic expression for the particle acceleration in the regular acceleration region. The results of this derivation are also useful for the interpretation of the multi-particle numerical simulations undertaken in the next chapter. Specifically, we are interested in determining the dependence of this acceleration on the wave amplitude, ε , and frequency, ν .

Since the regular acceleration region lies at $\rho < \nu$, we can derive the analytic expression for $d\rho/d\tau$ by performing asymptotic expansion of the Bessel functions in Eq. (2.20) in terms of the Gamma functions [47],

$$J_\nu(\rho) = \frac{1}{\Gamma(\nu+1)} \left(\frac{\rho}{2}\right)^\nu, \quad \text{where} \quad \Gamma(\nu) = \int_0^\infty t^{\nu-1} e^{-t} dt \quad \text{for} \quad \nu \gg \rho > 0. \quad (2.27)$$

Using these identities we express function $L(\rho, \nu)$ (see Eq. (2.21)) as,

$$\begin{aligned} L(\nu) = & -\frac{1}{\Gamma(\nu)\Gamma(-\nu+2)} + \frac{1}{\Gamma(\nu+1)\Gamma(-\nu+1)} \\ & + \frac{1}{\Gamma(\nu+2)\Gamma(-\nu)} - \frac{1}{\Gamma(\nu+3)\Gamma(-\nu-1)}. \end{aligned}$$

We can further simplify these expressions using the following identities,

$$\begin{aligned} \Gamma(1+\nu) &= \nu\Gamma(\nu) \\ \Gamma(1-\nu) &= -\nu\Gamma(-\nu) = \frac{\pi}{\Gamma(\nu)\sin\pi\nu} = \frac{\pi\nu}{\Gamma(1+\nu)\sin\pi\nu}. \end{aligned}$$

Notice that now $L(\nu)$ is a function of ν only. Finally we are able to write down the follow-

ing expression for the particle acceleration

$$\frac{d\rho}{d\tau} = -\frac{\partial H}{\partial \vartheta} = \frac{\rho \sin \vartheta}{\nu} \frac{\varepsilon^2 \pi}{8 \sin \pi \nu} L(\nu), \quad (2.28)$$

and after some algebraic manipulations we obtain the following simplification,

$$\frac{d\rho}{d\tau} = \varepsilon^2 \rho \sin \vartheta \left[\frac{2\nu^2 + 2\nu - 1}{4\nu^2(\nu^2 - 1)(\nu + 2)} \right], \quad (2.29)$$

which for $\nu \gg 1$ becomes

$$\frac{d\rho}{d\tau} = \frac{1}{2} \rho \frac{\varepsilon^2}{\nu^3} \sin \vartheta, \quad (2.30)$$

While it may seem from the equation above that the overall acceleration is zero (because the average of “ $\sin \vartheta$ ” over one period is zero), we now show that this is not the case. To do that we investigate the trajectory of a particle interacting with beating electrostatic waves under the following conditions: $\varepsilon = 10$, $\nu_1 = 24.3$, $\nu_2 = 25.3$, and $(\rho_0, \vartheta_0) = (1, 0)$. The non-integer wave frequencies have been chosen for the investigation since this was one of the restrictions placed on our analysis (see previous section). However, as we will demonstrate shortly, general dependencies that we will derive in this section are also valid for integer frequencies, as well.

Time evolution of the particle velocity, ρ , for $0 < \tau < 1500\pi$ is shown in Fig. 2.14a. This trajectory was obtained by solving numerically Eq. (2.5) with the conditions given above. Derivative of this trajectory with respect to τ is marked appropriately as $d\rho/d\tau$, and is approximately constant, as expected. We check validity of Eq. (2.30) by substituting into the RHS of that expression values of ρ (and corresponding values of ϑ) for this trajectory. The dot-dashed curve in Fig. 2.14a shows that Eq. (2.30) also predicts an approximately constant acceleration over most of the region. However, the absolute value of this acceleration is about an order of magnitude above that predicted by the numerical simulation.

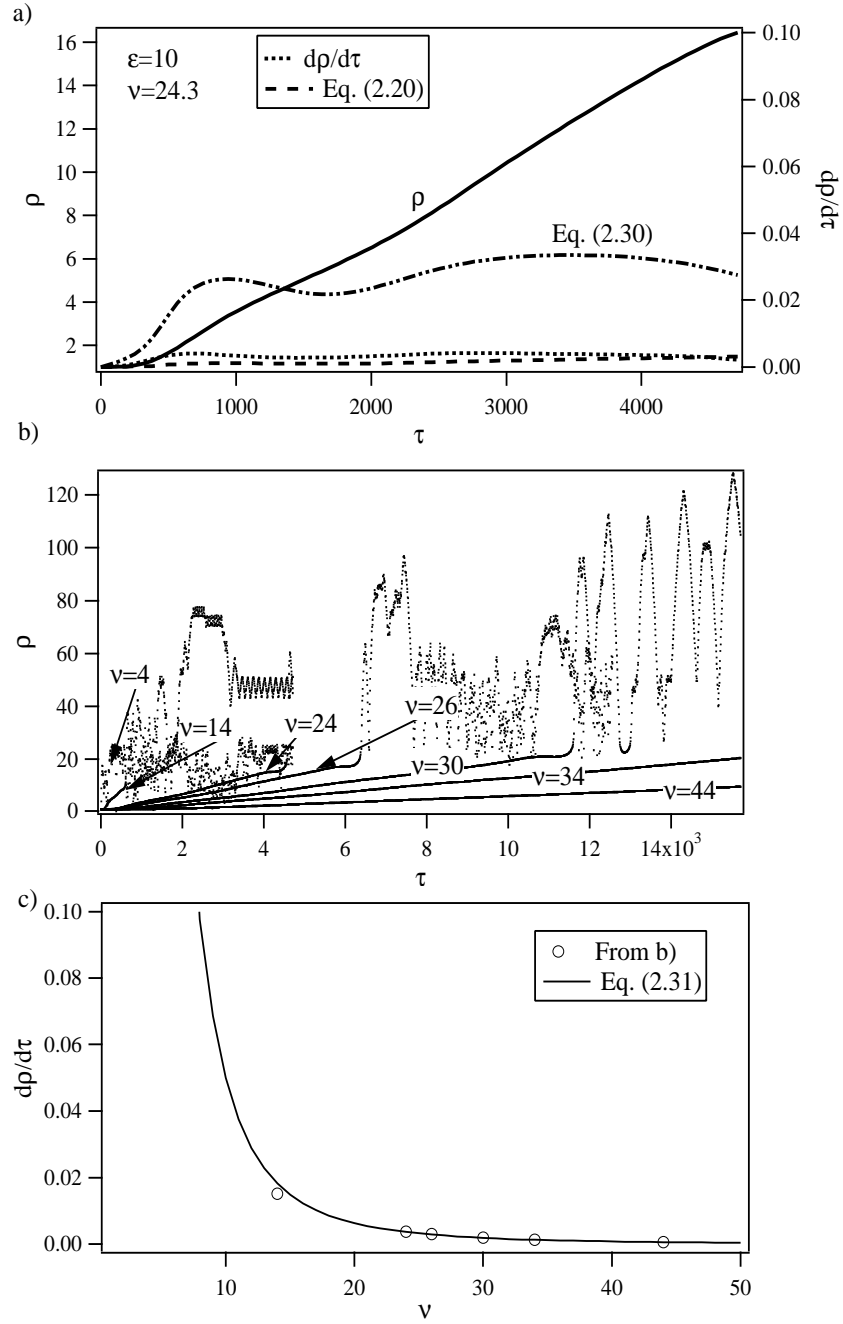


Figure 2.14: a) Particle acceleration determined from numerical solution to Eq. (2.5) is matched well by the analytic solution to Eq. (2.20). b) Velocity evolution for a single particle interacting with beating waves of various frequencies and $\varepsilon = 10$. For all cases the initial conditions were the same: $(\rho_0, \vartheta_0)=(1,0)$. c) The RHS of the expression (2.31) (—) is in good agreement with the slopes determined from numerically differentiating the curves in b) for the same ε (○).

This difference is the result of all the approximations made in deriving Eq. (2.20) from Eq. (2.30). Upon substituting the corresponding values of ρ and ϑ into the expression for $d\rho/d\tau$ evaluated with Eq. (2.20), we obtain a much better agreement, as demonstrated by the curve marked as “Eq. (2.20)” in Fig. 2.14a.

However, the point of this exercise was not to obtain the exact analytic expression for $d\rho/d\tau$, but rather to demonstrate that Eq. (2.30) approximates the overall particle behavior. Once again, we are specifically interested in the ε and ν dependencies, and thus we may conclude that

$$\frac{d\rho}{d\tau} \sim \frac{1}{2} \frac{\varepsilon^2}{\nu^3}. \quad (2.31)$$

Figure 2.14c shows the RHS of the expression (2.31) (solid line) together with the slopes measured from numerical simulations, similar to the one shown in Fig. 2.14a, but with various *integer* wave frequencies. These trajectories are shown in Fig. 2.14b. The wave amplitude as well as the particle initial conditions are the same as those used in Fig. 2.14a. For the specific initial conditions used in these simulations, quantitative agreement with the RHS of (2.31) is good; however, we must note that while the scaling implicit in (2.31) applies to all values of ν and ε , the close agreement shown in Fig. 2.14c may not hold for a different set of initial parameters.

2.9 Two Beating On-resonance Waves

While we have focused on the off-resonance cases, a few words on the on-resonance cases should also be added. When we choose ν_i and ν_j to be both integers, the overall behavior becomes much more complicated and no simple analytical expression for the positions of critical points can be found, as was the case in the previous section. Figure 2.15 shows a typical on-resonance example with $\varepsilon = 10$, $\nu_i = 24$, and $\nu_j = 25$. One major difference is the location of the hyperbolic point. There are two hyperbolic points in the regular accel-

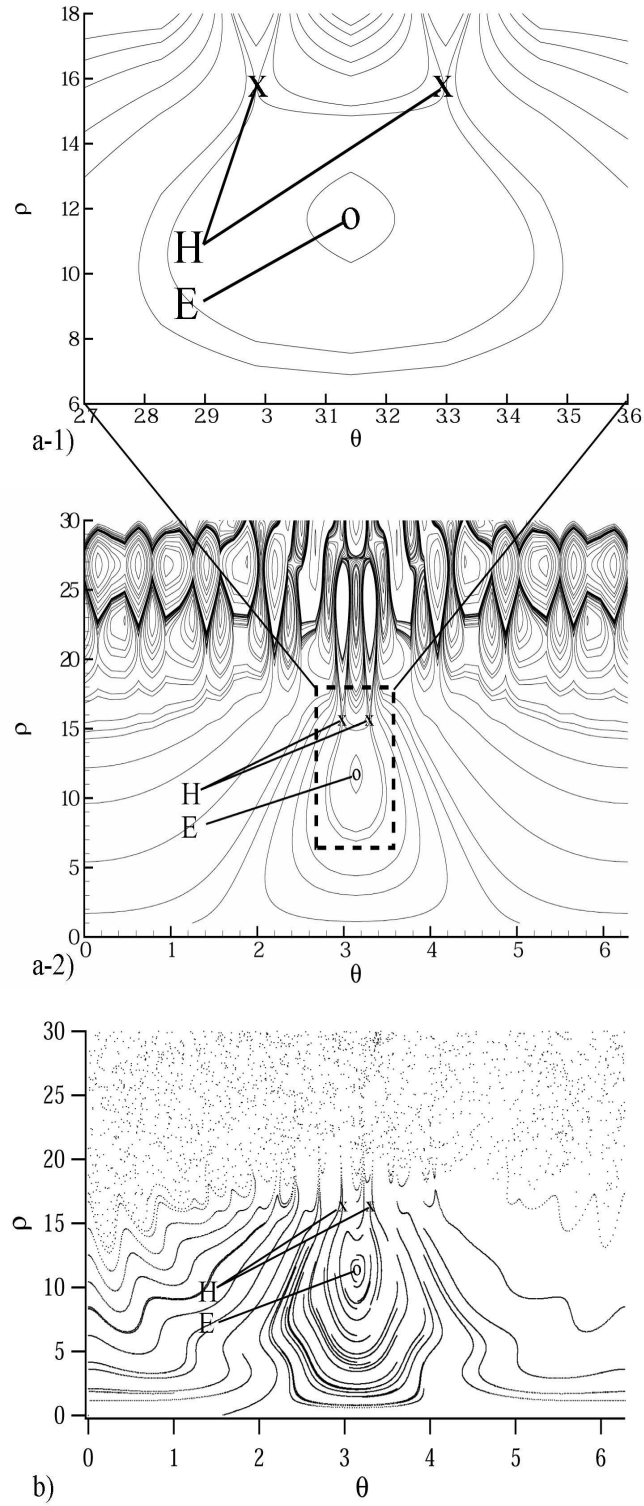


Figure 2.15: Poincaré section for a particle interacting with two beating on-resonance waves showing a more complicated dynamics than that of the off-resonance case shown in Fig. 2.7. ($\varepsilon = 10$, $\nu_i = 24$, $\nu_j = 25$). a-1) and a-2) analytical solution. b) numerical solution.

eration region in the on-resonance case, and these points do not lie at $\theta = \pi$. Nevertheless, we could still find their positions by solving Eqs. (2.14) and (2.15) numerically.

The elliptic point remains at $\theta = \pi$. Therefore its location could be obtained from the calculations identical to those done in the off-resonance case. The calculations are simplified because the first-order terms in Eqs. (2.14) and (2.15) drop out for $\theta = \pi$, as in the off-resonance case. Therefore, Eq. (2.26)a is also valid for the on-resonance cases.

Figure 2.15 shows that the analytical solution exhibits a complicated chain of critical points at large values of ρ . This partly illustrates why the analytical treatment of the on-resonance case is more challenging. However, we note that the two hyperbolic points in the regular acceleration region even in this case are very close to the hyperbolic point in the similar off-resonance case, and thus their position may be approximated by Eq. (2.26)b. Indeed, by studying numerically solutions to Eq. (2.5) for both on-resonance and off-resonance cases we conclude that the locations of the elliptic and hyperbolic points for both cases could be well approximated by Eqs. (2.26).

2.10 Chapter Summary

The beating criterion ($\omega_1 - \omega_2 = n\omega_c$) proposed by Benisti *et al.* [3, 4] allows magnetized ions to be accelerated by a pair of beating electrostatic waves. The importance of this mechanism stems from its ability to accelerate ions with arbitrarily low initial velocity. It has become clear however, (see Fig. 2.7) that this criterion is not sufficient for acceleration.

In order to better define the criteria for acceleration we investigated multiple ion trajectories (multiple initial conditions) on the same Poincaré section. This analysis led to the identification of critical points on the phase diagram. A vigorous ion acceleration now can be explained in terms of the location of these points in the region of regular motion. A second-order perturbation analysis of the equation of motion allowed us to derive the criterion defining the allowed and forbidden acceleration regions in terms of the location

of these points.

According to this analysis, for a pair of beating ($\nu_1 - \nu_2 = 1$) electrostatic waves interacting nonlinearly with a magnetized ion, significant ion acceleration can occur as long as the Hamiltonian of the system *does not* satisfy the following “trapping” criterion

$$H([\nu - \sqrt{\varepsilon}]/2; \pi) < H(\rho_0; \vartheta_0) < H(\nu - \sqrt{\varepsilon}; \pi),$$

$$\text{with } \rho_0 < \nu - \sqrt{\varepsilon}, \quad (2.32)$$

(which strictly applies when $\nu \gg 1$). If the ion’s initial conditions do not satisfy the above trapping criteria, the ion can be accelerated from arbitrarily low initial velocity through the region of regular motion to the stochastic region where substantial acceleration can occur. It is important to note that the trapping criterion is expressed in terms of the *Hamiltonian* and not just the *velocity* (ρ_0). Regular ion acceleration is a much slower process than stochastic energization [48]. However, as the wave amplitude is increased, the region of stochastic motion can extend down to low initial velocities.

The necessary (wave-beating) condition, stated in Eq. (2.4), along with the avoidance of the trapping criterion, stated in Eq. (2.32), represent two *necessary and sufficient* conditions for the beating-wave ion acceleration mechanism to occur.

While the above study offers insight into the fundamental problem of a single ion interacting with two beating electrostatic waves, the relevance of the mechanism to practical problems involving a real plasma rests on resolving the issues of: 1) the extension of the study to collection of particles and the role of collisions and, 2) the wave propagation in a real plasma. This first issue is the subject of the next chapter, while the discussion of the second issue will be undertaken in Chapter 5.

Chapter 3

Numerical Investigation

All models are wrong, but some are useful.

– George E. P. Box

This chapter presents a numerical model of ion heating by electrostatic waves that is based on combining a Monte Carlo technique to describe Coulomb collisions between ions, and solving a nonlinear 3-dimensional equation of ion motion between collisions. Using this model we conduct a parametric study to investigate the effects of ion collisions on heating effectiveness for both Single Electrostatic Wave (SEW) and Beating Electrostatic Waves (BEW) heating mechanisms.

This chapter is organized as follows. Section 3.1 interprets the findings from the previous chapter in a context relevant to the numerical study. In Section 3.2 we present a numerical model that describes the ion Coulomb collision dynamics using a Monte Carlo technique and also tracks a large number of ions using a 3-dimensional equation of motion between collisions. Section 3.3 presents and discusses the results of our numerical investigation, and in Section 3.4 we summarize the findings.

3.1 Single Particle Model

As discussed in the previous chapter, the motion of an ion interacting with electrostatic waves that propagate perpendicularly to a constant magnetic field is governed by the following equation,

$$\frac{d^2x}{dt^2} + \omega_{ci}^2 x = \frac{q}{m} \sum_j E_j \sin(k_{\perp j} x - \omega_j t + \varphi_j). \quad (3.1)$$

Furthermore, Benisti *et al.* have found that ions can be accelerated from an arbitrary low velocity by a pair of beating electrostatic waves, such that [3]

$$\omega_2 - \omega_1 = n\omega_{ci}. \quad (3.2)$$

This was a significant finding, as discussed in Chapter 2, since the non-beating waves can only accelerate ions that are already moving above a certain velocity. We have also found, in Chapter 2, that the beating criterion should be augmented with a restriction on the particle energy – Hamiltonian. For that we defined the “forbidden acceleration region”

$$H_H < H(\rho_0; \vartheta_0) < H_E, \quad \text{with } \rho_0 < \nu - \sqrt{\varepsilon}, \quad (3.3)$$

where the subscript “0” denotes initial conditions, and H_H and H_E are the values of the Hamiltonian evaluated at the hyperbolic and elliptic points, as shown schematically in Fig. 3.1b. As long as the two waves satisfy Eq. (3.2), ions that *do not* lie in the forbidden acceleration region will be accelerated by the beating waves. This statement constitutes the necessary and sufficient condition for ion acceleration by the BEW.

The following graphical illustration can help to explain the formidable mathematics governing the SEW and BEW acceleration mechanisms and the necessary and sufficient conditions for the acceleration to occur. Figure 3.1 shows all possible acceleration processes for the SEW (Fig. 3.1a) and BEW (Fig. 3.1b) schemes.

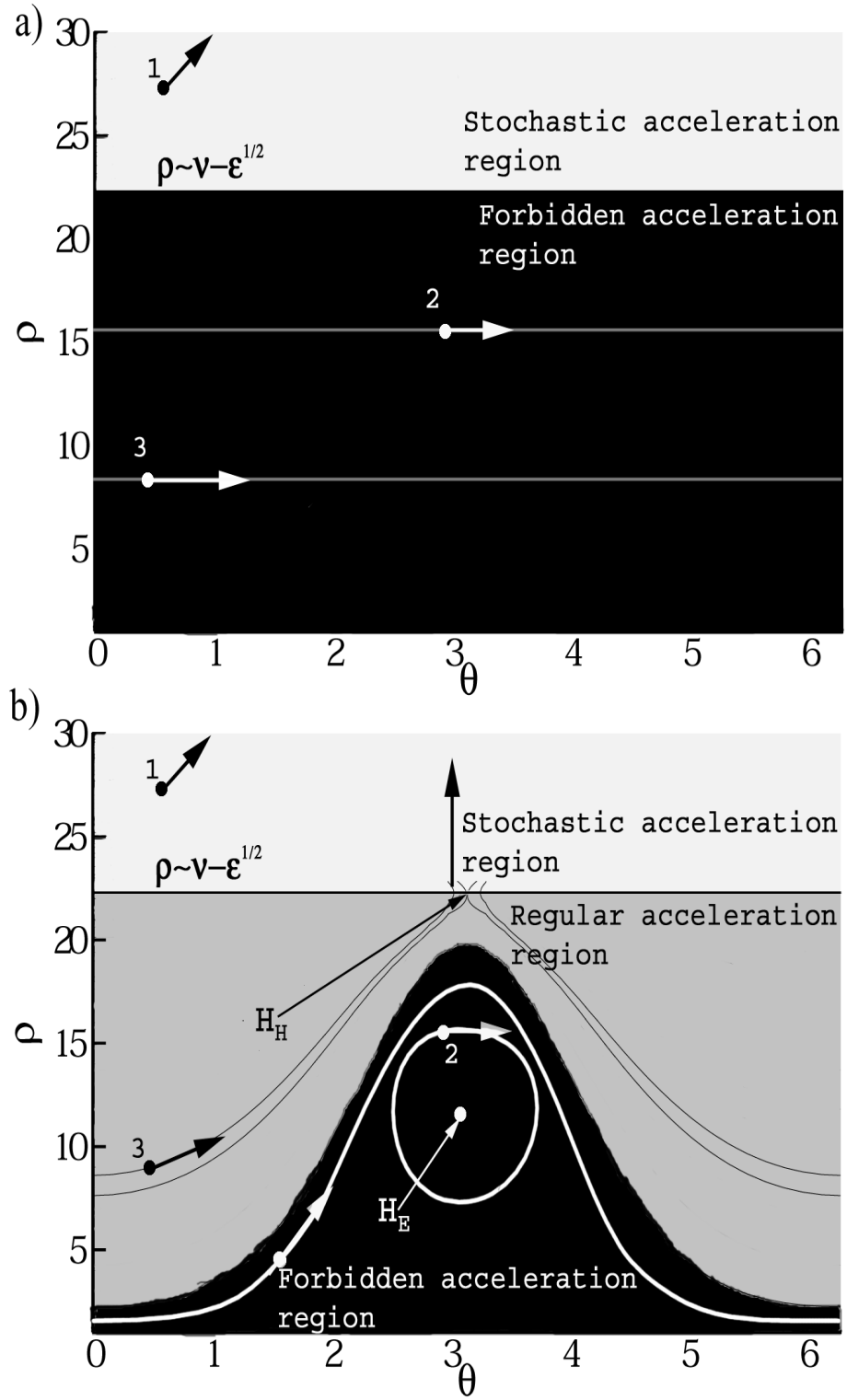


Figure 3.1: Poincaré section schematics. The figure shows typical trajectories for various initial conditions of an ion interacting with: a) a single electrostatic wave (SEW), b) beating electrostatic waves (BEW).

For the SEW case (Fig. 3.1a) the Poincaré section consists of two regions: the “forbidden acceleration region” (black) and “stochastic acceleration region” (light grey). Particles initially in one region cannot move into the other unless scattered by collisions with other particles, as will be discussed later in this chapter. A particle in the forbidden acceleration region is not affected by the wave, and its trajectory remains circular in the xy space (a particle gyrating in magnetic field). Since θ is the particle gyro-angle, this trajectory is represented by a horizontal line on the Poincaré section, as illustrated by the trajectories of particles 2 and 3 in Fig. 3.1a. On the other hand, a particle in the stochastic acceleration region is vigorously accelerated, as shown schematically by particle 1. Since this is the only region on the Poincaré section where significant ion acceleration is possible, the stochastic acceleration region can also be generalized as the “allowed acceleration region”.

The BEW interaction case is shown in Fig. 3.1b. The allowed acceleration region now consists of the “regular acceleration region” (dark grey) and “stochastic acceleration region” (light grey). For small values of ε the border between the two regions is roughly predicted by the single-wave threshold ($\rho = \nu - \sqrt{\varepsilon}$). A particle in the regular acceleration region (e.g. particle 3 in Fig. 3.1b) is accelerated by beating electrostatic waves into the stochastic acceleration region. While the regular acceleration is slower than stochastic acceleration, it allows the particles with small initial velocities to reach the stochastic acceleration region, where they are further accelerated to very high velocities.

Thus, the salient differences between the SEW and BEW acceleration mechanisms can be understood by following trajectories of the three particles in Fig. 3.1. Particle 1 in both panels of Fig. 3.1 is in the stochastic acceleration region, and undergoes vigorous acceleration in both cases. Particle 2 with initial energy below the SEW resonance threshold ($\rho = \nu - \sqrt{\varepsilon}$) lies in the forbidden acceleration region for both SEW and BEW acceleration. It is affected by beating electrostatic waves only slightly, and is never allowed to reach the stochastic acceleration region. On the other hand, while particle 3 is also below the SEW threshold, it is in the allowed acceleration region for the BEW interaction. The

particle remains unaffected by the single electrostatic wave, Fig. 3.1a, but is accelerated by the beating electrostatic waves, Fig. 3.1b. It is important to note that the initial kinetic energy of particle 3 is less than that of particle 2 ($\rho_3 < \rho_2$). This point demonstrates the importance of the particle gyrophase with respect to the beating waves rather than its velocity, or more accurately, the importance of the Hamiltonian, which includes the phase information, over that of the energy.

3.2 Including Collisions

Collisions drastically alter the picture described in the previous section. Without collisions an ion inside the forbidden acceleration region (e.g. particle 2 in Fig. 3.1b) cannot be accelerated by the beating electrostatic waves. However, a collision can instantaneously change the ion trajectory and place it outside the forbidden acceleration region. Note that according to Fig. 3.1b the change in the phase angle θ is as important as the change in velocity. Thus for example, an ion in the forbidden acceleration region may lose momentum during a collision, move to the regular acceleration region, and, if its phase angle is favorable, consequently be accelerated by the beating electrostatic waves into the stochastic acceleration region.

Since collisions between the like particles are easier to simulate, in this chapter we consider ion-ion collisions only. Coulomb ion collisions are of interest since the main focus of this dissertation is the stochastic ion heating and this type of collisions thermalizes the heavy species. Effects of the ion-neutral collisions on the wave propagation and ion heating will be discussed later in Chapter 5.

To introduce collisions into our numerical model we follow the classical work of Takizuka and Abe [49]. We model the Coulomb collisions as an accumulation of small-angle binary collisions. We also assume that on a sufficiently small time scale we can uncouple these binary collisions from the particle motion. Thus, our algorithm consists of two parts.

We move each particle between collisions according to the equation of motion prescribed by the single-particle collisionless model, presented in the previous chapter. We then use the Monte Carlo approach to determine randomly the collision partners and the scattering angles for each binary collision.

3.2.1 Overall Implementation

1. We first choose a time step Δt much smaller than the ion-ion relaxation time calculated for the initial ion temperature. Since the ion temperature increases with time, and the Coulomb collision frequency is proportional to $T_i^{-3/2}$, the time step is assured to be smaller than the relaxation time throughout the simulation.
2. Using a 4th order Runge-Kutta scheme we then follow each particle in our simulation for Δt seconds according to the 3-dimensional equation of motion for a single ion, given below by the set of Eqs. (3.10).
3. Next we randomly choose a collision partner for each ion.
4. Using the Monte Carlo method described in Section 3.2.2 we then determine the velocity increments for each colliding pair. The new velocities are fed back into the Runge-Kutta solver.
5. After each binary collision, we store the value of the scattering angle Ψ for each particle. We assume that whenever $\sum \sin^2 \Psi \geq 1$ the particle has undergone one ion-ion Coulomb collision. Here the summation is over successive collisions for a given particle. This evaluation is consistent with the classical Coulomb collision frequency definition given by Mitchner and Kruger [50].

3.2.2 Momentum Exchange During Collisions

We model Coulomb collisions between ions as a sum of small angle binary elastic scattering events [49]. Such collisions preserve energy and momentum.

The relative velocity vector $\mathbf{u} = (u_x, u_y, u_z)$ for a colliding pair of particles is

$$\mathbf{u} = \mathbf{v}_a - \mathbf{v}_b, \quad (3.4)$$

where \mathbf{v}_a and \mathbf{v}_b are the velocities of the two colliding ions in the laboratory frame. The post-collision relative velocity \mathbf{u}^f is

$$\mathbf{u}^f = \mathbf{u}^i + \Delta\mathbf{u}, \quad (3.5)$$

where \mathbf{u}^i is the relative velocity right before the collision and $\Delta\mathbf{u}$ is the change in the relative velocity caused by the collision. The change in the relative velocity due to a scattering event can be derived from the conservation principles, and is given by [49],

$$\begin{aligned} \Delta u_x &= (u_x/u_\perp)u_z \sin \Psi \cos \Phi - (u_y/u_\perp)u \sin \Psi \sin \Phi \\ &\quad - u_x(1 - \cos \Psi), \end{aligned} \quad (3.6a)$$

$$\begin{aligned} \Delta u_y &= (u_y/u_\perp)u_z \sin \Psi \cos \Phi + (u_x/u_\perp)u \sin \Psi \sin \Phi \\ &\quad - u_y(1 - \cos \Psi), \end{aligned} \quad (3.6b)$$

$$\Delta u_z = -u_\perp \sin \Psi \cos \Phi - u_x(1 - \cos \Psi), \quad (3.6c)$$

where $u_\perp^2 = u_x^2 + u_y^2$ and $u^2 = u_\perp^2 + u_z^2$. Here the perpendicular and parallel directions are defined relative to the magnetic field (\hat{z} axis). Angle Φ is chosen homogeneously randomly

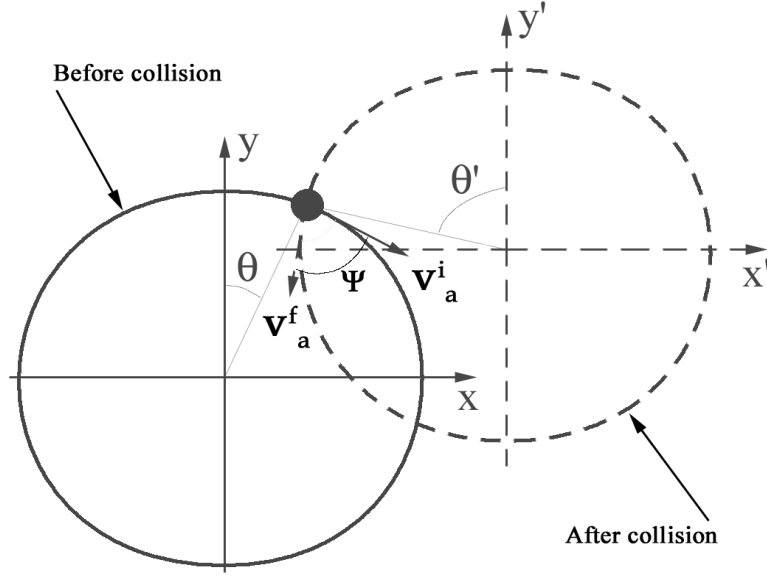


Figure 3.2: Illustration of the particle cross-field diffusion due to collisions. A particle is gyrating around the center of axis in the xy coordinate system before a collision. Right after the collision the particle gyrates about the center of axis in the $x'y'$ coordinate system. The new position of the particle (x', y') and its phase angle θ' are used instead of (x, y) in the numerical simulation for consistency.

from 0 to 2π , and angle Ψ can be found from

$$\sin \Psi = \frac{2\delta}{1 + \delta^2}, \quad (3.7a)$$

$$1 - \cos \Psi = \frac{2\delta^2}{1 + \delta^2}, \quad (3.7b)$$

where $\delta = \tan(\Psi/2)$ is a random number chosen with the Gaussian distribution centered around zero and having the following variance $\langle \delta^2 \rangle$:

$$\langle \delta^2 \rangle = \Delta t \frac{q^4 n_e \lambda}{\pi \epsilon_0^2 m_i^2 \|\mathbf{u}^i\|^3}, \quad (3.8)$$

where q and m are the charge and the mass of the ion, n_e is the particle number density, λ is the Coulomb logarithm, ϵ_0 is the permittivity of free space, $\|\mathbf{u}^i\|$ is the relative speed of the two colliding ions before the collision, and Δt is the time step [49].

Because the two colliding particles have the same mass, the post-collision velocity is

found from the following simple relations

$$\mathbf{v}_a^f = \mathbf{v}_a^i + \frac{1}{2}\Delta\mathbf{u}, \quad (3.9a)$$

$$\mathbf{v}_b^f = \mathbf{v}_b^i + \frac{1}{2}\Delta\mathbf{u}. \quad (3.9b)$$

As was stated earlier, elastic binary collisions occur on a significantly smaller time scale than the particle motion, and consequently the position of the colliding particles is not altered during the collision. Presence of a magnetic field however, introduces some difficulty in tracking the particle trajectory self-consistently. Consider, for example, a particle right before a collision. Equation (3.1) describes the gyromotion of this particle around the origin of the xy coordinate system, as shown in Fig. 3.2. At a moment right after the collision the velocity vector of this particle has instantaneously changed to \mathbf{v}_a^f . Essentially, the particle has jumped to a different magnetic field line. To track the trajectory consistently with the new velocity we now need to reorient the coordinate system to $x'y'$, as shown in Fig. 3.2. It can be demonstrated that

$$\begin{aligned} x' &= -(1/\omega_{ci})\mathbf{v}_y^f, \\ y' &= (1/\omega_{ci})\mathbf{v}_x^f, \\ z' &= z. \end{aligned} \quad (3.10)$$

These new coordinates (x', y', z') , rather than the pre-collision (x, y, z) coordinates, together with \mathbf{v}^f , obtained from Eq. (3.9), are fed back to the Runge-Kutta solver as the new initial conditions.

3.2.3 Moving the Particles

Starting from the Lorentz force equation,

$$\mathbf{F} = m\ddot{\mathbf{r}} = q(\mathbf{E} + \mathbf{v} \times \mathbf{B}), \quad (3.11)$$

we can derive the equation of motion for a single particle in three dimensions. In our analysis, the magnetic field is constant, $\mathbf{B} = B\hat{z}$, and the electric field arises from the propagating electrostatic waves, as shown in Fig. 2.1. Therefore, we can rewrite Eq. (3.11) as

$$\ddot{x} = \omega_{ci}\dot{y} + \frac{q}{m_i}E \sum_i \sin(k_i x - \omega_i t), \quad (3.12a)$$

$$\ddot{y} = -\omega_{ci}\dot{x}, \quad (3.12b)$$

$$\ddot{z} = 0, \quad (3.12c)$$

where \ddot{x} , \ddot{y} , and \ddot{z} are the second derivatives with respect to time t , and the other variables are the same as those appearing in Eq. (2.1). Equation (3.12) is equivalent to Eq. (2.1) but is written in the form that can be readily programmed into a 4th order Runge-Kutta numerical solver.

3.3 Simulations

We now use the model described in the previous section to conduct a parametric study of ion heating by two beating electrostatic waves. For this study, unless stated otherwise, we assume that the initial ion temperature is 0.1 eV. This is chosen to be similar to the values observed in the BWX experiment. In addition, we set $k_1 = k_2 = 20 \text{ cm}^{-1}$, and $B = 0.2$ Tesla. These numbers are consistent with the experiments reported by Skiff *et al.* [17]. During the simulation runs we follow trajectories of 1000 particles. A larger number of particles requires excessive computational time and a smaller number might not give a good statistical representation of the interaction.

We first visualize the results of the simulations using Poincaré sections, and compare and contrast these results with the schematic illustrated in Fig. 3.1b. Next we demonstrate the difference between the SEW and BEW ion heating schemes with an example ($\varepsilon =$

10, $\nu_1 = 24.3$, $\nu_2 = 25.3$, $\kappa_i = 1$), and show how the ion-ion collisions influence the kinetic energy evolution. By varying plasma the density, n_e , we then show that the ion Coulomb collisions enhance the effectiveness of ion heating by increasing the ion heating rate and the maximal energy obtained by the system of particles. Finally, we investigate the ion energy evolution as a function of the electric field amplitude and wave frequency.

3.3.1 Poincaré Sections

Figure 3.3 shows an example that follows the evolution of 1000 collisionless particles interacting with beating electrostatic waves ($\varepsilon = 10$, $\nu_1 = 24.3$, $\nu_2 = 25.3$). Initially we distribute all particles homogeneously over some region of the phase space ($\rho \lesssim 20$), as shown by the first panel in Fig. 3.3. We obtain this distribution by creating the 3-dimensional Maxwellian ion velocity distribution profile corresponding to $T_i = 0.1$ eV. Then we normalize the perpendicular velocity of each particle in accordance with the rules given below Eq. (2.3) to get ρ . Finally, for each particle we calculate the phase angle $\theta = \tan^{-1} v_y/v_x$.

Stochastic motion is observed whenever the ions reach the stochastic acceleration region ($\rho > 20$). Once that happens, an ion can be accelerated vigorously to a very high velocity corresponding to $\rho \sim 80 - 100$. Figure 3.3 shows the time evolution of the Poincaré section for the BEW collisionless scheme. In that figure only the particles with initial conditions laying outside the forbidden acceleration region are accelerated. Points corresponding to the unaccelerated particles form a mount-like structure, seen in the last two panels of Fig. 3.3. The structure corresponds to the forbidden acceleration region shown in Fig. 3.1b.

Figure 3.4 follows evolution of 1000 particles with the same initial distribution as in Fig. 3.3, but now the particles are allowed to collide with each other. This simulation corresponds to the plasma density $n_e = 10^{12} \text{ cm}^{-3}$. The evolution of the particle distribution is fundamentally different from that of the collisionless case, illustrated in Fig. 3.3. Many more ions reach the high values of ρ than during the collisionless interaction. This happens

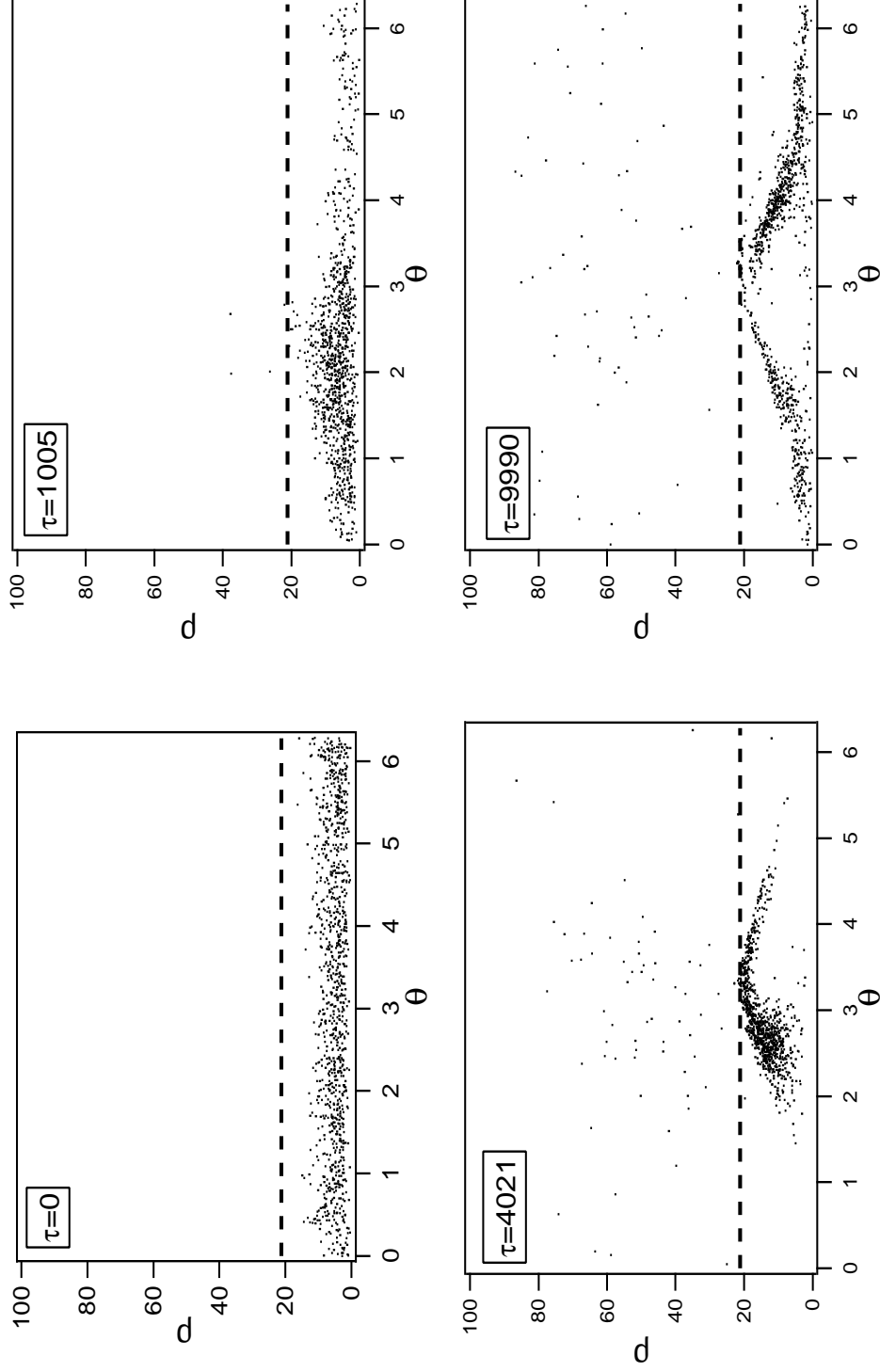


Figure 3.3: Poincaré sections showing the time evolution of particle velocities during the collisionless BEW interaction. Because the particles are not allowed to collide with each other, the "hump" corresponds to the particles inside the forbidden acceleration region. These particles are not strongly affected by the beating waves in accordance with Eq. (3.3). $\varepsilon = 10$, $\nu_1 = 24.3$, $\nu_2 = 25.3$.

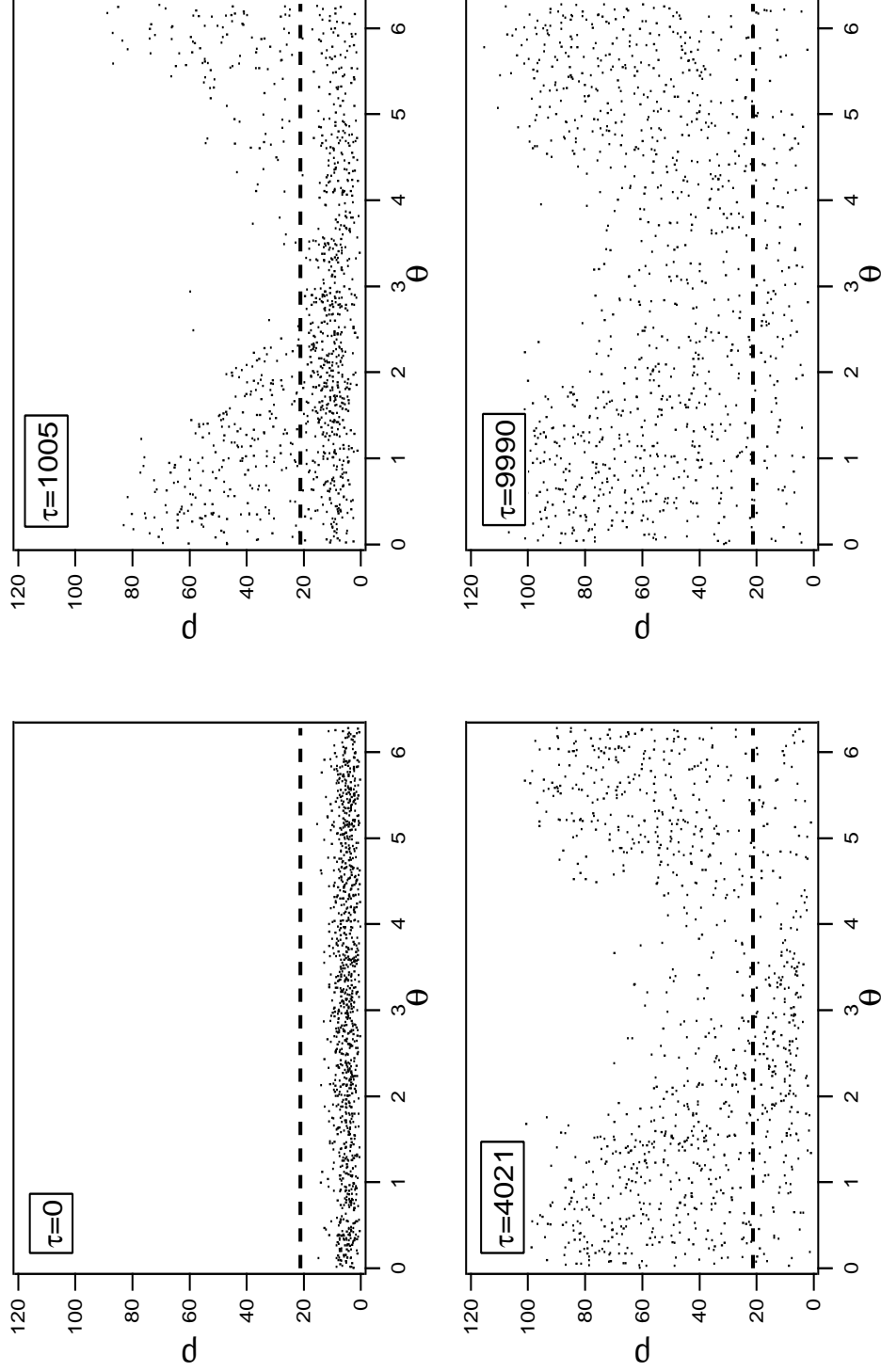


Figure 3.4: Poincaré sections showing the time evolution of particle velocities during the collisional BEW interaction. In contrast to Fig. 3.3, particles inside the forbidden acceleration region can be knocked out into the allowed acceleration region by a collision, and subsequently accelerated by the beating electrostatic waves. $n_e = 10^{12} \text{ cm}^{-3}$, $\varepsilon = 10$, $\nu_1 = 24.3$, $\nu_2 = 25.3$.

because ions originally in the forbidden acceleration region can now be accelerated by the waves. This can happen by two different routes.

An ion in the forbidden acceleration region can be knocked directly into the stochastic acceleration region, where it will then undergo vigorous acceleration by the beating waves. Another route involves an ion knocked into the regular acceleration region, where it will then be slowly accelerated into the stochastic acceleration region by the beating electrostatic waves following a trajectory similar to particle 3 in Fig. 3.1b. It is important to point out that, while the colliding partner may lose its energy during such a collision, that particle does not necessarily end up in the forbidden acceleration region. Thus, after the collision both colliding partners may be accelerated by the beating waves.

Ion Coulomb collisions enhance stochastic ion heating because collisions allow all ions (with finite probability) to eventually be accelerated by the beating electrostatic waves. That is what makes the BEW acceleration mechanism attractive for the ion heating in warm collisional plasmas, such as used for space plasma propulsion.

3.3.2 Velocity Evolution

Comparison of numerical simulation results gives insights into the effectiveness of the wave heating mechanism. We define the ion heating effectiveness by the following two indices: 1) the ion heating rate and, 2) the maximum energy attained by the system of ions (or maximum temperature, when the distribution is Maxwellian). Both indices may be important for the design of a practical device based on the stochastic ion heating mechanism.

Keeping these two indices in mind we now investigate the evolution of the kinetic energy of the entire system consisting of 1000 particles as a function of various parameters. Figure 3.5 compares the BEW and SEW heating mechanisms for both collisionless and collisional cases. Each curve was obtained by averaging the perpendicular kinetic energy over all particles, and then normalizing v_{ave} to obtain ρ_{ave} . In that figure the dashed curves correspond to the collisionless cases while the solid curves represent simulations with the

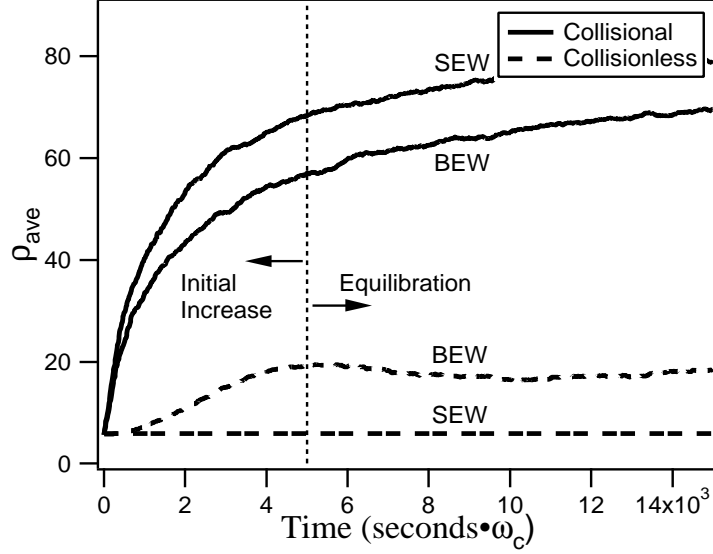


Figure 3.5: Perpendicular velocity evolution for 1000 particles interacting with beating electrostatic waves with $\varepsilon = 10$, $\nu_1 = 24.3$, $\nu_2 = 25.3$. For comparison we also show the evolution for the single electrostatic wave interaction with $\varepsilon = 10$, $\nu = 24.3$. The collisional case corresponds to plasma density $n_e = 10^{12} \text{ cm}^{-3}$. Initial ion temperature is $T_i = 0.1 \text{ eV}$.

plasma density equivalent to $n_e = 10^{12} \text{ cm}^{-3}$. The initial ion distribution used to obtain all curves in Fig. 3.5 was the same as that shown in Figs. 3.3 and 3.4, so that most ions lie below the threshold for the SEW heating. Additionally, wave amplitude in the SEW simulation ($\varepsilon = 20$) was twice that of each wave in the BEW simulation ($\varepsilon = 10$). This condition ensures that the total wave energy is equal in both cases. The curves in Fig. 3.5 show two stages in the velocity evolution: 1) the initial energy increase followed by 2) the equilibration stage, where the system energy approaches a plateau. The curve for the collisionless SEW mechanism is flat because we chose the initial particle distribution such that most of the particles are below the single-wave acceleration threshold, and thus do not interact with the single electrostatic wave.

Therefore, Fig. 3.5 shows that beating electrostatic wave can produce heating in a collisionless plasma because the waves can accelerate ions, whose velocities are below the single-wave threshold, as discussed in the previous chapter. Our simulations also show (see Figs. 3.3 and 3.4) that the initial velocity rise is caused by the ions funneling to the

stochastic region. In the case of the beating electrostatic waves interacting with a collisionless plasma, a fraction of the ions below the single-wave threshold reach the stochastic acceleration region. These ions initially reside in the allowed acceleration region and follow trajectories similar to that of the particle 3 in Fig. 3.1b.

As mentioned earlier, collisions provide another mechanism by which an ion, even in the forbidden acceleration region, can reach the stochastic acceleration region. Therefore, the collisional BEW ion heating can result in even higher heating rate and maximal attained energy than BEW heating in a collisionless plasma, as shown in Fig. 3.5. Our simulations have also shown that with the help of collisions, a single electrostatic wave can heat the ions whose initial velocities are below the single-wave threshold, whereas no heating was possible in a collisionless plasma. Furthermore, for the chosen parameters in Fig. 3.5, the SEW mechanism resulted in a greater energy increase than the BEW mechanism. The SEW stochastic acceleration region, in this case, is more homogeneous than that for the BEW acceleration mechanism. As will be shown shortly, the maximal energy attained by the system of simulated particles is a function of the ratio between areas occupied by the stochastic and forbidden acceleration regions on the Poincaré section. Therefore, the higher effectiveness of the SEW heating mechanism can be explained, in this case, by the topological differences between the stochastic acceleration regions of the two mechanisms. However, as will be shown next, a different set of parameters may be found where the effectiveness of the BEW heating mechanism is greater than that of the SEW mechanism.

Effectiveness of the two heating mechanisms depends on many parameters, such as wave amplitude and frequency, initial ion temperature, and plasma density. Dependence on the latter two can be better understood through investigations of Coulomb collision frequency. Figure 3.6 shows curves for the BEW and SEW heating that qualitatively resemble respective collisionless curves in Fig. 3.5. However, in Fig. 3.6 we simulate a collisional plasma with initial ion temperature $T_i = 3$ eV, which is much higher than the initial ion temperature used in Fig. 3.5. Additionally, plasma density, normalized amplitude, and fre-

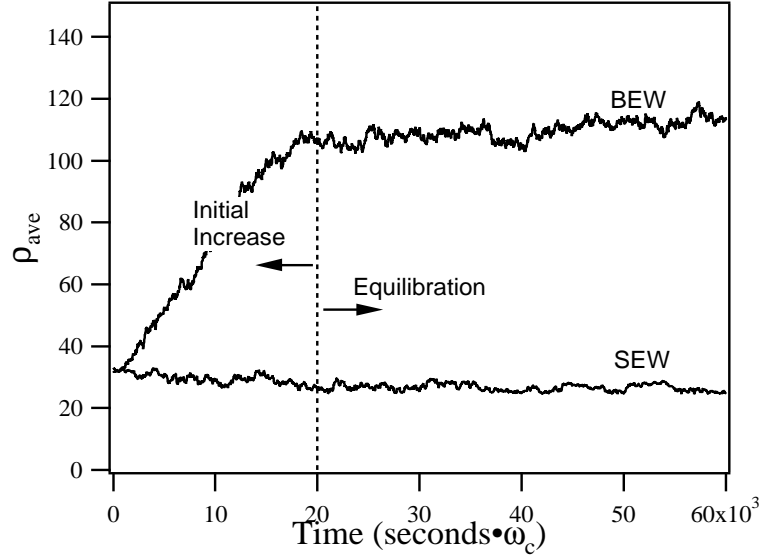


Figure 3.6: Perpendicular velocity evolution for 1000 particles interacting with BEW ($\varepsilon = 10$, $\nu_1 = 104.3$, $\nu_2 = 105.3$) and SEW ($\varepsilon = 100$, $\nu = 104.3$). Qualitatively, the improvement in the BEW heating over that of the SEW in this picture is similar to the improvement shown for the collisionless simulation in Fig. 3.5. Other parameters used in this simulations are: $n_e = 10^{11} \text{ cm}^{-3}$, $B = 0.1 \text{ T}$, $T_i = 3 \text{ eV}$.

quencies of the waves in Fig. 3.6 were chosen to be $n_e = 10^{11} \text{ cm}^{-3}$, $\varepsilon = 100$, $\nu_1 = 104.3$, and $\nu_2 = 105.3$ respectively ($\nu = 104.3$ for the SEW case). This particular choice of plasma density and initial ion temperature ensures very low, yet finite, Coulomb collision frequency. For the BEW case, this Coulomb collision frequency decreases even further as ions gain energy from the waves, since the frequency is proportional to $T_i^{-3/2}$. Thus, Fig. 3.6 demonstrates that even in dense plasmas the BEW heating scheme can be more effective than the SEW scheme, as long as the initial ion temperature is high enough to ensure low collision frequency.

It also should be noted that the wave frequency was chosen such that the bulk of the ion velocity distribution function lies below the single-wave threshold, as is the case in Fig. 3.5. If we were to chose a wave with a lower frequency, then the single-wave threshold would also be lowered, in accordance with Eq. (2.10), and a larger portion of the ion velocity distribution function would fall into the stochastic acceleration region for both SEW and BEW cases. Eventually, as wave frequency is lowered further, both mechanisms produce similar

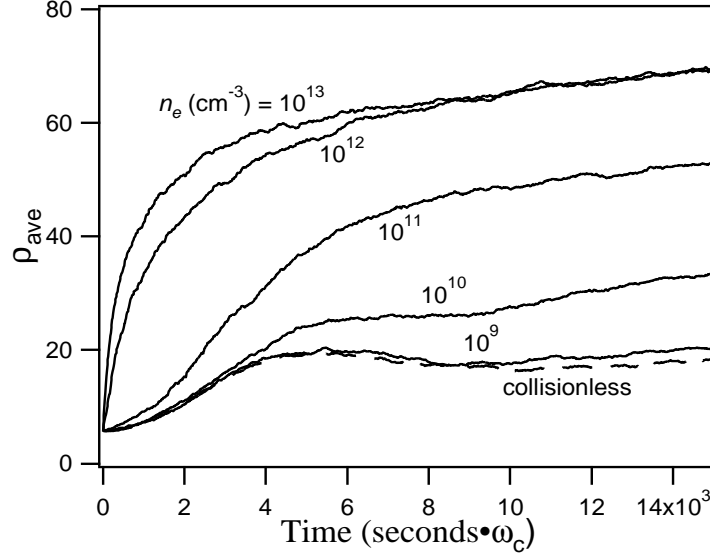


Figure 3.7: Velocity evolution of 1000 particles interacting with beating electrostatic waves as a function of plasma density (i.e. collision frequency). The ion heating rate and the maximal energy increase with the plasma density, i.e the collision frequency. $\varepsilon = 10$, $\nu_1 = 24.3$, $\nu_2 = 25.3$.

heating, because the bulk of the velocity distribution function lies in the stochastic acceleration region. This point is of particular importance, since in our experiments, presented in Chapter 5, we seek conditions where the BEW heating mechanism can be distinguished from the SEW mechanism. Finally, we also note that frequency $\nu \sim 100$ corresponds to the lower-hybrid wave, which is electrostatic.

We can further investigate effects of Coulomb collision frequency on the BEW heating scheme by varying plasma density. The results are shown in Fig. 3.7. Collisions have beneficial effects on both stages of plasma heating, the initial heating and equilibration. That trend can be explained by the ratio of the areas occupied by the forbidden and allowed acceleration regions on the Poincaré section. As can be seen from Fig. 3.1b, the forbidden acceleration region occupies a smaller area than the regular and stochastic acceleration regions combined. Therefore, because collisions are a random process, the chances that a particle is knocked out from the forbidden acceleration region are greater than the chances that a particle will end up in that region as a result of a collision. It follows that the more

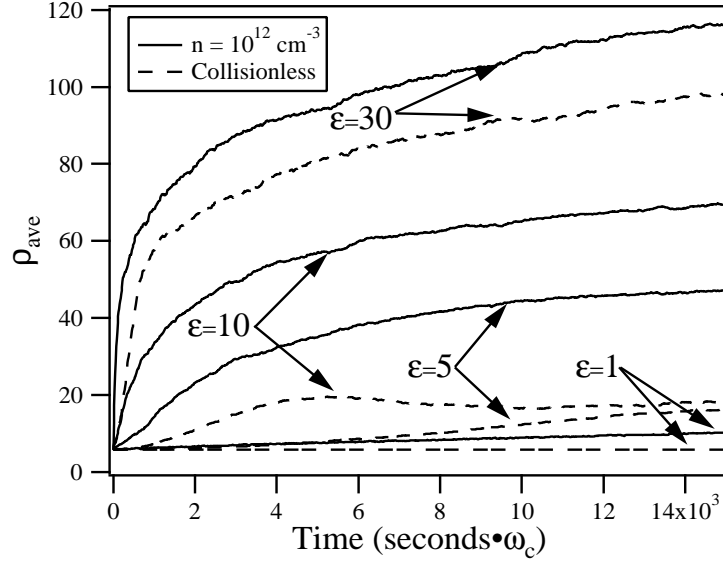


Figure 3.8: Velocity evolution of 1000 particles interacting with beating electrostatic waves as a function of the wave amplitude for both collisionless (dashed curves) and collisional (solid curves) cases. The heating effectiveness (both heating rate and the maximal energy) improves as the wave amplitude increases. $\nu_1 = 24.3$, $\nu_2 = 25.3$.

frequent collisions are, the more particles are knocked out from the forbidden acceleration region, and are then accelerated by the waves.

However, increasing the plasma density also means that an ion completes a lesser portion of the gyro-orbit between the collisions. This reduces the degree to which the nonlinear interaction affects the ion. At $n_e \gtrsim 10^{12} \text{ cm}^{-3}$ plasma is dominated by ion-ion collisions, i.e. $\nu_{ii} > \omega_{ci}$, where ν_{ii} is the ion-ion collision frequency. Furthermore, at plasma density $n_e \gtrsim 10^{13} \text{ cm}^{-3}$ the ion-ion collision frequency is greater than the wave frequency. This means that above $n_e = 10^{13} \text{ cm}^{-3}$ ion motion is dominated by collisions and maximal energy attained by the system of particles may plateau or even decrease with density. This is evident by comparing the lines for $n_e = 10^{12}$ and 10^{13} cm^{-3} in Fig. 3.7.

We next investigate the heating effectiveness as a function of the wave amplitude ε . Figure 2.8 shows that the stochastic acceleration region extends to the lower values of ρ as ε increases. Figure 3.8 demonstrates the ε dependence for the BEW interaction with a collisional ($n_e = 10^{12} \text{ cm}^{-3}$) as well as collisionless plasma. The effectiveness of the BEW

heating mechanism increases with increasing ε . This is an expected trend since ε is the normalized wave amplitude. Because the energy carried by a wave is proportional to the square of its amplitude, the wave with the higher ε will produce more heating. Furthermore, collisionless heating is always less effective than the collisional heating. However, the difference between the collisionless and collisional cases decreases at larger wave amplitudes because of the extended stochastic acceleration region.

Finally, we investigate the ion heating dependence on the wave frequency ν . Figure 3.9 shows this dependence for the collisional ($n_e = 10^{12} \text{ cm}^{-3}$) plasma interacting with beating electrostatic waves of various frequencies. As can be seen from that figure, the ion heating effectiveness displays a complex monotonic dependence on the wave frequency. The curves in the figure indicate that a wave with a smaller frequency heats ions faster, but to a lower final energy than a wave with a higher frequency.

Dependence gets even more complicated for the collisionless cases, which are shown in Fig. 3.10. While the heating rate decreases with the wave frequency, as in the collisional case, the maximal (final) energy is a more complex function of ν . To understand this complex dependence we need to take into account the initial particle velocity distribution as well as the nonlinear nature of the velocity evolution dictated by the equation of motion.

Looking back at Fig. 3.1b, it is reasonable to assume that the normalized maximal energy $E_{max}(\sim \rho_{max}^2)$ of the particles in all three regions of the Poincaré section scales with the wave frequency ν (since the vertical extent (ρ axis) of the entire Poincaré section scales with the location of the critical points of motion [51]) as well as the fraction of particles in each region. Therefore, we can express the total energy of all the particles on the Poincaré section as the sum of the total energy of each acceleration region. For example, the energy of the particles in the forbidden acceleration region is proportional to the square of the product $\eta_f N_r$ (the fraction of particles in that region) and $(\nu - \sqrt{\varepsilon})/2$, which is the vertical coordinate of the elliptic point on the Poincaré section. Here N_r is the *initial* fraction of particles below the single-wave threshold, given by Eq. (3.16), and η_f is

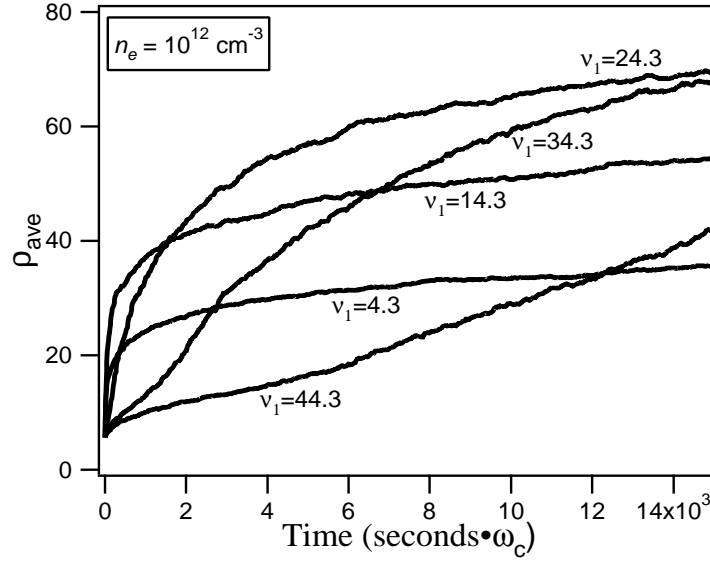


Figure 3.9: Velocity evolution of 1000 particles interacting with beating electrostatic waves ($\varepsilon = 10$) as a function of the wave frequency. Simulated plasma corresponds to $n_e = 10^{12} \text{ cm}^{-3}$.

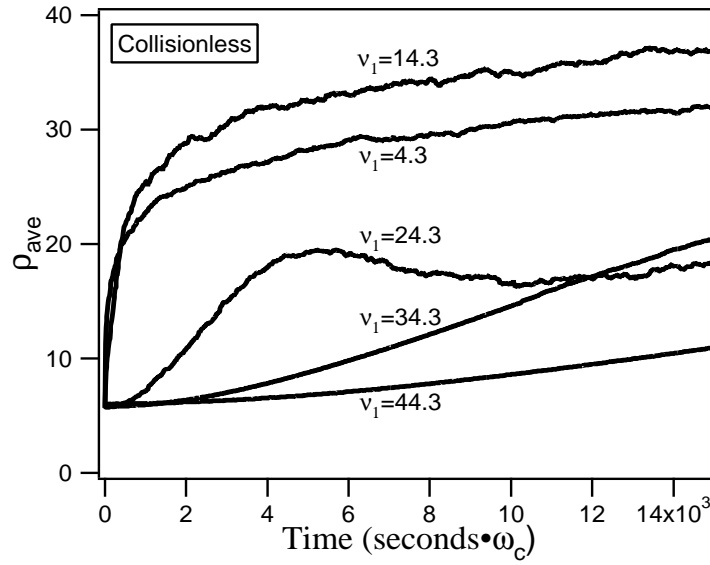


Figure 3.10: Velocity evolution of 1000 collisionless particles interacting with beating electrostatic waves ($\varepsilon = 10$) as a function of the wave frequency.

the fraction of those particles in the forbidden acceleration region. The total energy is then,

$$\begin{aligned}\rho_{max}^2 &= [c_f \eta_f N_r]^2 \\ &+ [c_r \eta_r \{(1 - \eta_f)N_r + N_s\}]^2 \\ &+ [c_s (1 - \eta_r) \{(1 - \eta_f)N_r + N_s\}]^2,\end{aligned}\tag{3.13}$$

where N_r and N_s are the initial fractions of particles below and above the single-wave threshold respectively, and the c 's are proportionality coefficients for each acceleration region. The final fraction of particles in the regular acceleration region is η_r – this is the fraction of particles in the region when the system reaches equilibrium. These fractions, of course, sum to unity,

$$\begin{aligned}\eta_f N_r + \eta_r \{(1 - \eta_f)N_r + N_s\} + (1 - \eta_r) \{(1 - \eta_f)N_r + N_s\} \\ = N_r + N_s = 1\end{aligned}$$

Values of η_r and η_f cannot be calculated exactly and must be extracted from the numerical simulations. Figure 3.11a shows η_r as a function of the wave frequency ν , and its corresponding best fit curve. These values are computed as the fraction of particles in the regular acceleration region at the end of the simulation. Figure 3.11b shows η_f , which was calculated as the ratio of the area of the forbidden acceleration region to the total area below the stochastic acceleration region, $2\pi(\nu - \sqrt{\varepsilon})$, on the Poincaré section. Since the Hamiltonian is a complicated function of θ and ρ , the area of the forbidden acceleration region was computed numerically. The best fit curves to these points are used in Eq. (3.13) and are given by the following expressions

$$\eta_r = 0.18 + 0.19 \tanh[0.22(\nu - 13.56)]\tag{3.14a}$$

$$\eta_f = 0.65 - 0.49 \exp[-0.10\nu]\tag{3.14b}$$

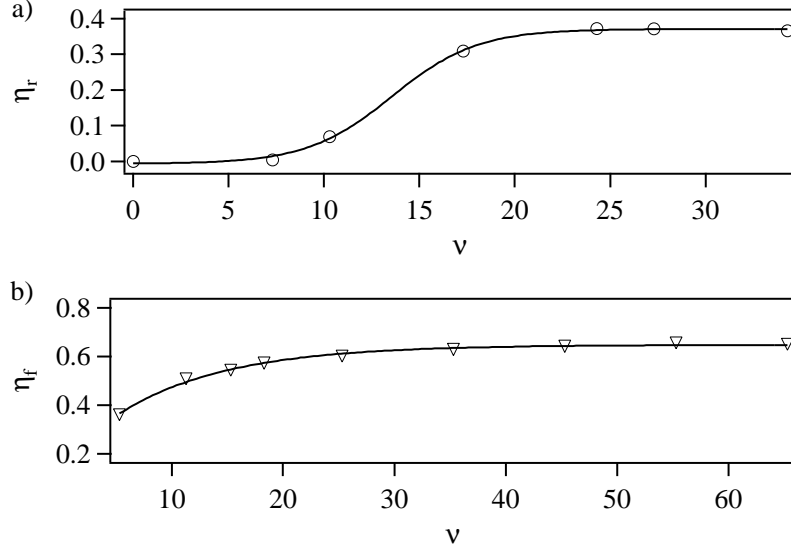


Figure 3.11: Fraction of particles below the single-wave threshold η_r and inside the forbidden acceleration region as functions of the normalized wave frequency ν . Points extracted from numerical simulations (\circ and ∇) are given together with the best fits, which are given by Eqs. 3.14.

For the forbidden acceleration region $c_f = (\nu - \sqrt{\varepsilon})/2$, as was discussed before, since the vertical extent of that region scales with the position of the elliptic point [51]. Similarly, for the regular acceleration region $c_r = \nu - \sqrt{\varepsilon}$. The value of c_s , which is the proportionality coefficient for the stochastic acceleration region, can be calculated from the numerical simulations by averaging the velocities of the particles in the stochastic acceleration region, and fitting the resultant numbers as a function of ν , as shown in Fig. 3.12.

To simplify our analysis we also assume that the initial particle velocity distribution is Maxwellian and is distributed randomly along the θ axis on the Poincaré section. This assumption is verified by the measurements of the ambient ion velocity distribution in the BWX experiment, as described in Chapter 5. The ion velocity distribution can be expressed in terms of ρ as

$$f_{\perp}(\rho) = 4\pi \left(\frac{m_i}{2\pi k_b T_i} \right)^{3/2} \left(\frac{\omega_{ci}}{k_{\perp}} \right)^2 \rho^2 \times e^{-\left(\frac{\omega_{ci}}{k_{\perp}} \right)^2 m_i \rho^2 / 2k_b T_i}, \quad (3.15)$$

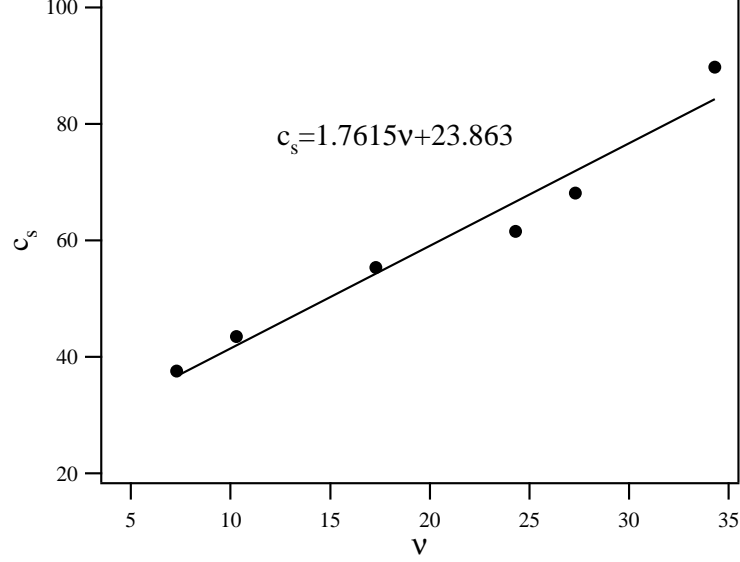


Figure 3.12: Proportionality coefficient c_s for the average energy of the particles in the stochastic acceleration region. Circles are computed by averaging ρ for the particles in the stochastic acceleration region at the end of each simulation. The proportionality coefficient is obtained through a linear least-squares fit to these points.

Where k_b is the Boltzmann constant, k_\perp is the perpendicular wavenumber, T_i is the perpendicular ion temperature, m_i is the ion mass, and ω_{ci} is the ion cyclotron frequency. We then can express the initial fraction of particles in each acceleration region as,

$$N_r = \int_0^{\nu-\sqrt{\varepsilon}} 4\pi \left(\frac{m_i}{2\pi k_b T_i} \right)^{3/2} \left(\frac{\omega_{ci}}{k_\perp} \right)^3 \rho^2 \times e^{-\left(\frac{\omega_{ci}}{k_\perp} \right)^2 m_i \rho^2 / 2k_b T_i} d\rho \quad (3.16)$$

$$N_s = \int_{\nu-\sqrt{\varepsilon}}^{\infty} 4\pi \left(\frac{m_i}{2\pi k_b T_i} \right)^{3/2} \left(\frac{\omega_{ci}}{k_\perp} \right)^3 \rho^2 \times e^{-\left(\frac{\omega_{ci}}{k_\perp} \right)^2 m_i \rho^2 / 2k_b T_i} d\rho. \quad (3.17)$$

Figure 3.13 shows the maximal velocity ρ_{ave}^{max} as a function of the wave frequency ν . The open circles were obtained from the numerical simulations for a collisionless plasma described above (e.g. see Fig. 3.10), while the solid curve is the solution of Eq. (3.13). The analytical equation predicts the right trends. For small values of ν (0–10) the maximal energy increases with the frequency because most of the particles already lie in the

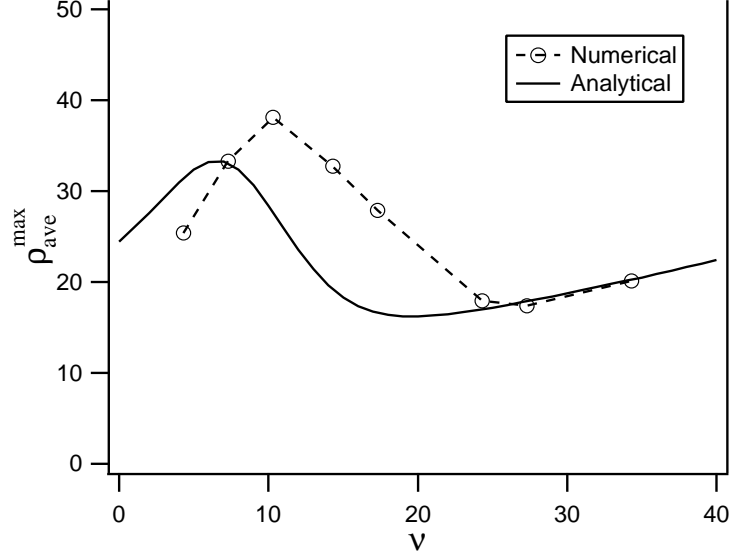


Figure 3.13: Maximal energy (averaged over 1000 particles) as a function of the wave frequency for the cases with collisionless BEW heating. The curve extracted from numerical simulations (e.g. the maximal values of curves in Fig. 3.10) is shown by dashed line and open circles. It is in a good qualitative agreement with the solution to Eq. (3.13), shown by solid line. Other parameters used to construct this figure are: $\varepsilon = 10$, $\nu_{1,2} = 24.3, 25.3$, $T_i = 0.1$ eV, and $B = 0.2$ T.

stochastic region, and are vigorously accelerated by the waves. For the intermediate values of ν (10–20) a progressively larger particle fraction falls into the forbidden acceleration region. Consequently the maximal energy also decreases. For yet higher values of ν (>20) the fraction of particles in the forbidden region saturates and the maximal energy resumes its growth.

The analytical model described allows one to choose the right wave frequency to maximize the heating effectiveness. According to Fig. 3.13, a wave with frequency slightly above the ion cyclotron frequency, $\nu = \omega/\omega_{ci} \sim 8$, will result in the greatest amount of ion heating by beating electrostatic waves. It should be noted, however, that Fig. 3.13 was obtained for the specific plasma and wave parameters listed in Section 3.3. These parameters were chosen to closely resemble conditions of the previously reported experiments [17], and plasma parameters in the BWX experiment, which will be described in the next chapter. Effects of changing these parameters could be a subject of future studies.

3.4 Chapter Summary

In this chapter we extended the study of a single particle interacting with beating electrostatic waves, which we described in the previous chapter, to the case of a real plasma, in which a large number of particles interacts with beating electrostatic waves while undergoing Coulomb collisions. The following conclusions can be drawn from this study,

- Our simulations showed that a single electrostatic wave can heat ions below the single-wave threshold in presence of collisions, whereas no heating below the threshold is possible in a collisionless plasma.
- The results also indicate that ion-ion collisions can improve the ion heating rate and increase the maximal attained energy for both the SEW and BEW heating schemes. The simulations showed that the ion heating effectiveness increases as the plasma density (i.e. collision frequency) is raised from 10^9 to 10^{12} cm^{-3} . The heating effectiveness also increases with the wave amplitude for collisional as well as collisionless cases of the BEW and SEW heating mechanisms.
- The results of the numerical simulations show that in a collisionless plasma the maximal ion energy is a complicated function of the wave frequency. Using a simple analytical model we were able to predict the maximal energy dependence on the wave frequency.
- The BEW heating scheme was found to be more effective than the SEW scheme even in dense plasmas, as long as the initial ion temperature is high enough to ensure low collisionality.
- Further improvements in the ion heating effectiveness can be achieved by choosing appropriate plasma and wave parameters. The simulation-supported phenomenological picture points to the promise of using beating electrostatic waves as a new and effective method for heating magnetized ions in a real plasma.

Chapter 4

Experimental Setup and Diagnostics

If you wish to make an apple pie from scratch, you must first create the universe.

– Carl Sagan

This chapter presents a detailed description of the BWX (Beating Waves Experiment) apparatus and diagnostics used to study the electrostatic wave propagation and dispersion, as well as the resulting stochastic ion heating. The chapter is organized as follows. First, we give a detailed description of the vacuum chamber in Section 4.1 and the rf plasma source in Section 4.2. Section 4.3 describes various electrostatic (ES) antennas that were tried in order to excite the electrostatic waves. Section 4.4 is dedicated to the diagnostics. It describes the various Langmuir probes and the LIF apparatus used to measure the plasma and wave properties.

4.1 Vacuum Chamber

A technical drawing and computer rendering of the Beating Waves Experiment (BWX) are shown in Fig. 4.1 and Fig. 4.2. The BWX vacuum chamber consists of a 6 cm diameter and 37 cm long Pyrex cylinder serving as the plasma source, connected through an aluminum

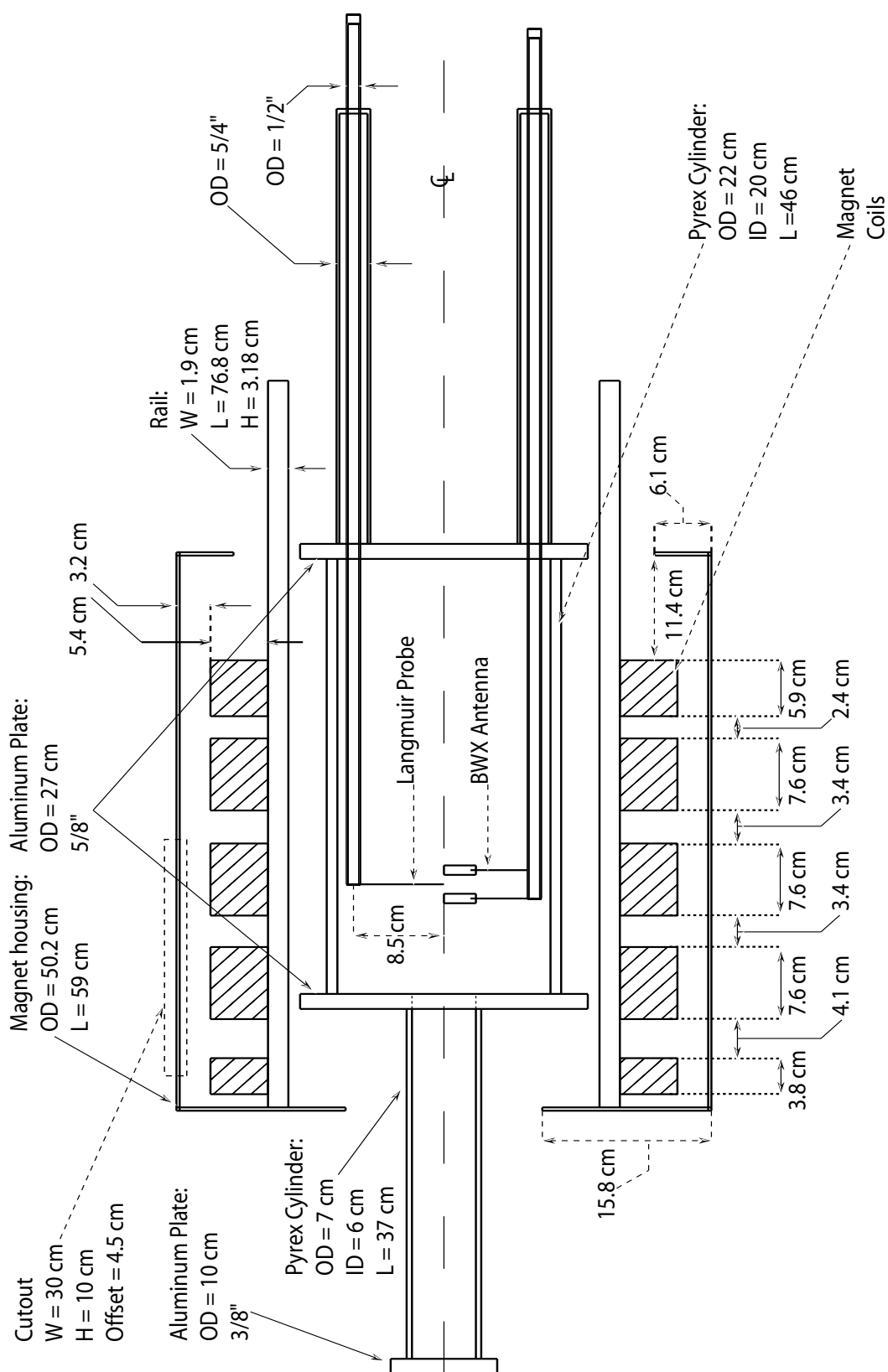


Figure 4.1: Schematic of the BWX vacuum chamber.

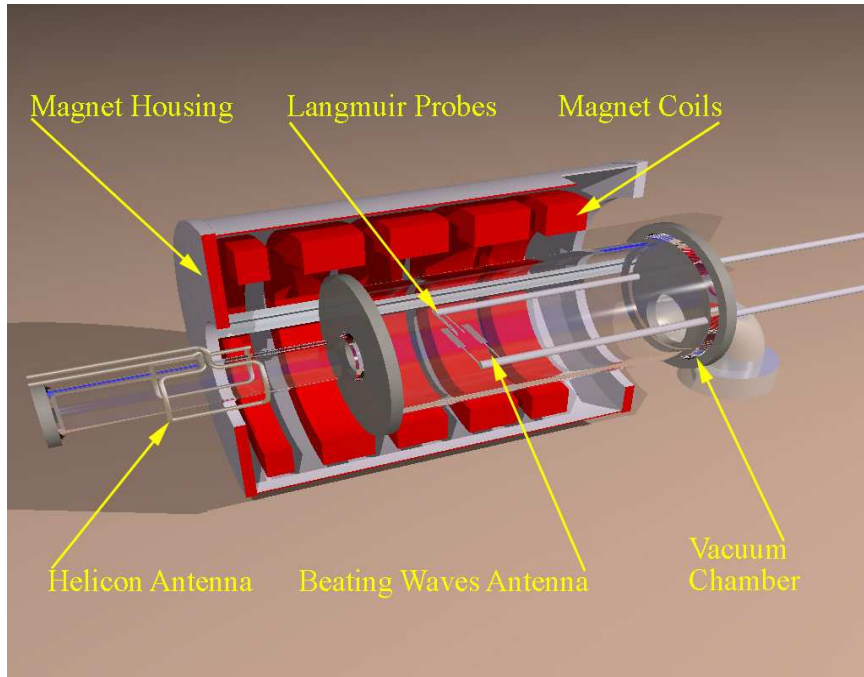


Figure 4.2: Computer rendering showing how the components of the BWX apparatus fit together.

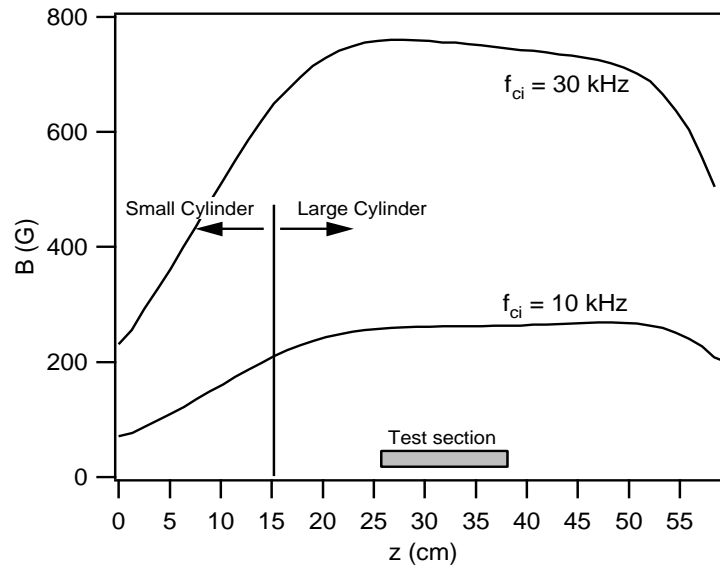


Figure 4.3: Axial magnetic field B_z along the centerline of the magnet. The ion cyclotron frequency varies by less than 3% within the test section of the large chamber, where the electrostatic waves are launched.

plate to a 20 cm and 46 cm long Pyrex cylinder serving as the test section. The aluminum plate is electrically isolated from the rest of the chamber and the electromagnet. The small cylinder is capped with a molybdenum backplate, which is electrically floating to minimize sputtering. The vacuum chamber is placed inside an electromagnet, which produces a homogeneous, steady-state magnetic field up to 0.1 Tesla, that is uniformly axial throughout the test section. The axial magnetic field along the centerline is shown in Fig. 4.3. The two curves correspond to ion cyclotron frequency of 10 kHz and 30 kHz in the test section of the vacuum chamber. Pressure of 1 to 30 mTorr is typically maintained by a gas feed (Ar or He) at the aluminum endplate of the large cylinder and by a 150 l/s turbo pump with a conductance controller backed up by a roughing pump. The system is capable of maintaining a base pressure of $2 \cdot 10^{-6}$ Torr.

Two 46 cm long arms protrude from the large endplate, as shown in Fig. 4.1. Wilson seals attached at the ends of the arms provide a vacuum-sealed translation and rotation feedthrough mechanism for the internal ES antenna (used to launch the electrostatic waves) and the Langmuir probes. Two 92 cm long, 0.5" (OD) hollow rods are inserted through the Wilson seals. Langmuir probes or ES antennas can be attached at one end of each of the rods. The rods consist of a 46 cm long stainless steel section that is attached to a 46 cm long G-11 fiberglass section. While the stainless steel section provides a good vacuum seal, the insulating G-11 section ensures that the proximity of the rod does not alter the plasma discharge. The wires to the ES antenna and the Langmuir probes are carried inside the hollow rods. The distance between the centerline of the vacuum chamber and the center of each rod is 8.5 cm, while the distance between the two rods is $2 \times 8.5 = 17$ cm.

Once the discharge is ignited in the small cylinder, the plasma propagates along the magnetic field lines, which are parallel to the axis of the cylinders, into the large chamber where the wave-launching and plasma-heating experiments are conducted.

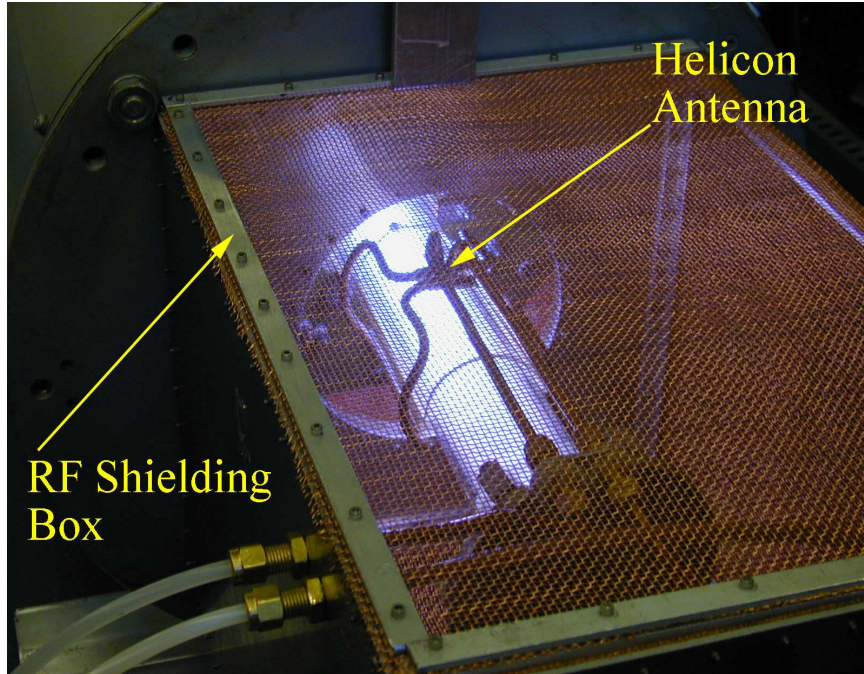


Figure 4.4: Photograph of an inductive rf discharge established by the helicon antenna. The copper mesh box surrounding the vacuum chamber forms a safety rf shielding cage.

4.2 Plasma Source

The plasma is generated in the smaller cylinder by a helicon source consisting of a Boswell saddle-type rf antenna wrapped around the smaller Pyrex cylinder, as shown in Fig. 4.4. The helicon antenna is made of 0.25" copper tubing to allow water cooling. The discharge is produced by supplying rf power to the helicon antenna from an ENI 13.56 MHz 1.2 kW power supply through a tuner. The tuner, shown in Fig. 4.5, consists of an L network made of two Jennings 1000 pF 3 kV variable vacuum capacitors. The tuner is placed as close to the helicon antenna as possible to maximize coupling to the antenna. A power control circuit allows for pulsed as well as steady-state plasma generation. The vacuum chamber is incased in a Faraday cage consisting partly of the magnet casing and partly of copper mesh to prevent the radiation emitted by the helicon antenna from leaking into the laboratory. The shielding is shown in Fig. 4.4.

A power control circuit allows for pulsed as well as steady-state plasma generation.

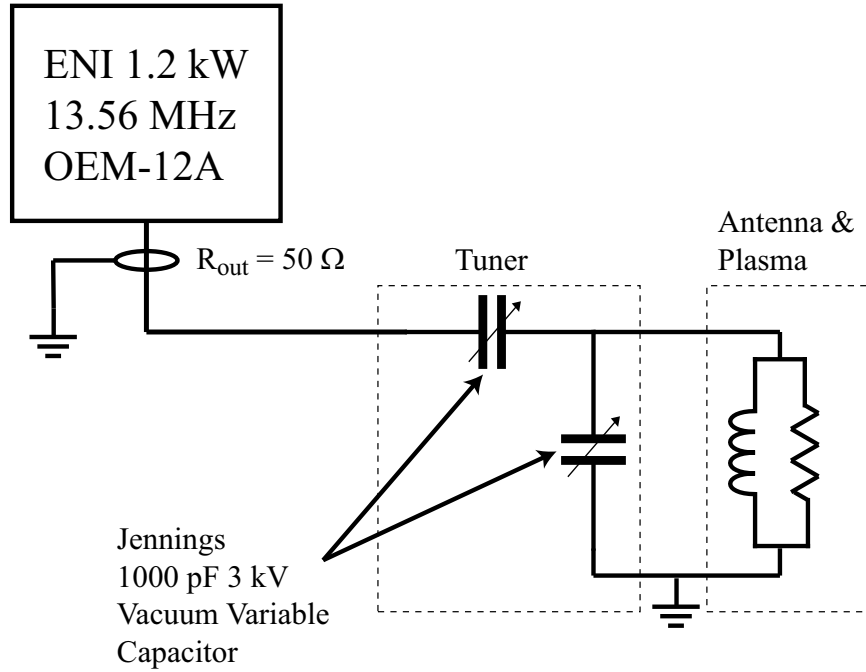


Figure 4.5: Schematic of the electric circuit driving the helicon antenna. An ENI OEM-12A 13.56 MHz rf power supply provides up to 1.2 kW to the helicon antenna through a π -network tuner consisting of two Jennings 1000 pF 3 kV variable vacuum capacitors.

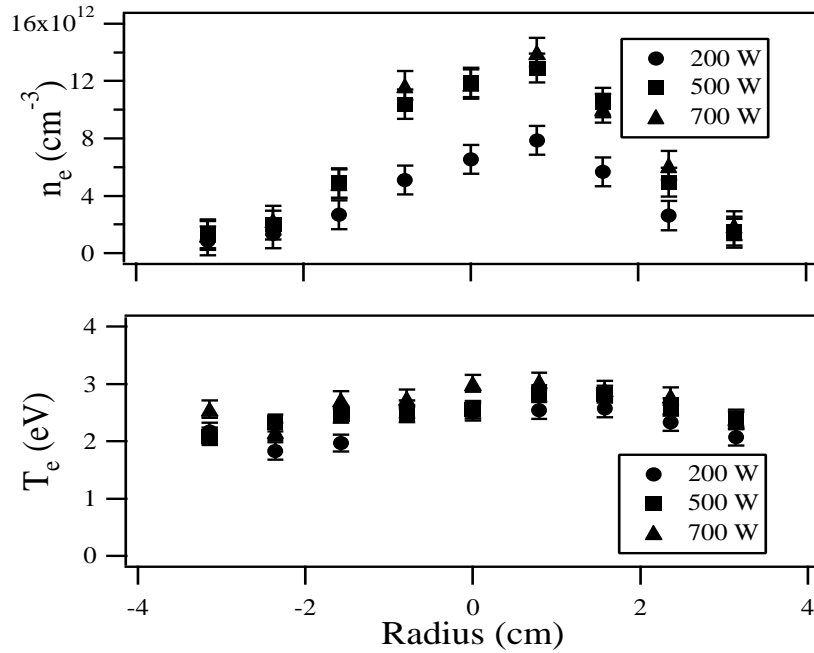


Figure 4.6: Plasma density and electron temperature profiles for various rf power to the helicon antenna. Plasma density increases with rf power. Electron temperature, on the other hand, is not a strong function of the rf power. Helicon discharge is observed as the rf power is raised beyond 500W. $B=261$ Gauss, $P=1$ mTorr.

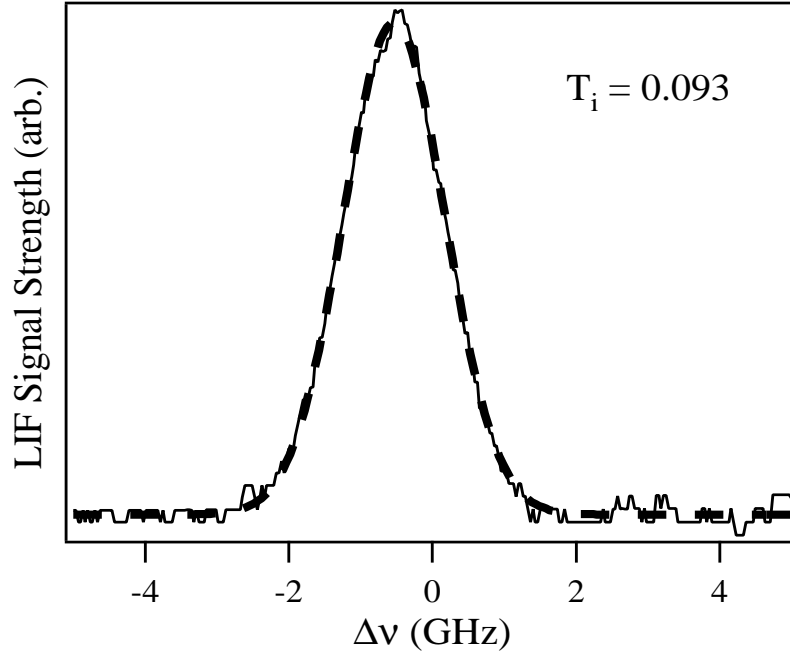


Figure 4.7: Typical LIF signal strength profile measured in the BWX experiment. The thin line is obtained from ~ 300 LIF data points, while the thick dashed line (almost indistinguishable) is a Gaussian fit to the data points.

The circuit consists of an HP 8116A function generator that sends a control and trigger signals to the ENI RF power supply. In addition, the signal from the HP function generator is delivered to a digital pulse and delay generator (DDG) DG565, where the signal can be delayed by an arbitrary amount to trigger the ES antennas, Langmuir probes, or other diagnostics.

An inductive discharge is easily obtained with only a few watts of forward rf power to the helicon antenna and only a few percent of rf power reflected. A helicon discharge with high plasma density ($n_e = 10^{13} \text{ cm}^{-3}$) can be produced as rf power to the helicon antenna is raised above 500 W by properly adjusting pressure, magnetic field, and capacitance of the coupling tuner. The inductively coupled discharge looks homogeneous and occupies the entire cross-section of the small cylinder. When the helicon discharge is obtained with argon, a bright blue column can be observed at the centerline. Measured radial profiles of plasma density and electron temperature for both types of discharges are shown in Fig. 4.6.

The radial distribution of the plasma density depends on the power input from the helicon antenna. For the low-power discharges the profile is more uniform, while at higher rf powers the profile becomes peaked at the center of the plasma column. The electron temperature, on the other, hand displays a more uniform profile, and is much less sensitive to the helicon antenna power. A small asymmetry in both plasma density and electron temperature profiles is most likely due to the interaction between the Langmuir probe and the plasma column.

An example of the ion velocity distribution function measured by the LIF technique is shown in Fig. 4.7. The distribution profile is obtained by scanning the laser through ~ 300 different frequencies. The ion temperature can be determined from a Gaussian fit to the measured velocity distribution profile. This technique will be further explained in Section 4.4.5. An excellent agreement between the fit (thick dashed line) and the measured distribution (thin line) indicates that the accuracy of the ion temperature measurement is determined primarily by the shot-to-shot repeatability rather than the fit accuracy. For the experiments reported here, the background electron and ion (perpendicular) temperatures were $T_e \approx 3$ eV and $T_{i\perp} \approx 0.1$ eV, and the ratio of the ion-neutral charge-exchange collision frequency to the ion cyclotron frequency $\nu_{ex}/\omega_{ci} = 0.2$, as will be shown in the next section. The parallel ion temperature was not measured, but in a typical inductive discharge it roughly equals half of the perpendicular ion temperature. It should be noted that the ratio ν_{ex}/ω_{ci} is an order of magnitude above that of the Skiff's experiment [17]. While the ion-neutral collision frequency is an order of magnitude smaller than the ion cyclotron frequency, charge-exchange collisions play an important role in the electrostatic wave dispersion. Figure 4.8 shows the range of some natural plasma frequencies in the BWX that were calculated with the measured T_e , T_i , n_e , and B_0 .

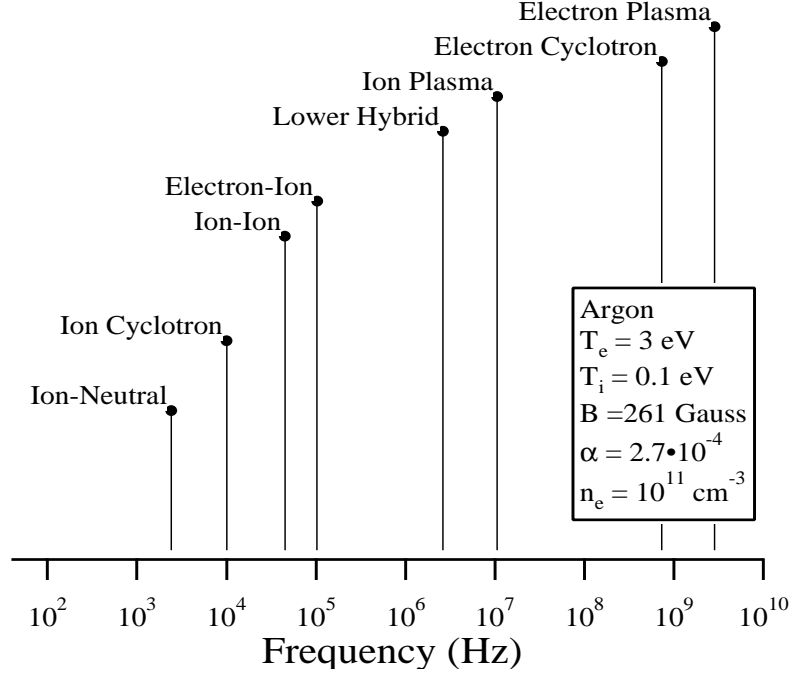


Figure 4.8: Typical plasma parameters for the BWX experiment calculated with measured T_e , T_i , n_e , and B .

4.3 Electrostatic (ES) Wave Antennas

In order to launch electrostatic waves into the plasma three different electrostatic (ES) antenna types were tested: 1) Helmholtz-coil antenna wrapped outside the vacuum chamber, 2) internal (to the vacuum chamber) two-plate antenna, and 3) internal loop antenna. We were unable to launch electrostatic waves with the Helmholtz-coil antenna. Therefore, for the rest of this dissertation we will concentrate on the other two antenna types. The two-plate or loop antennas were placed inside the test section of the BWX vacuum chamber. In addition, the two-plate ES antenna was situated directly inside the plasma column. The ES antennas were driven by one or two Wavetek 180 signal generators, which are capable of producing a signal up to 20 V_{pp} into a 50Ω load. The signal was further amplified by an operational amplifier or an ENI 2100L broadband amplifier, and sent through a tuning circuit to match the ES antenna impedance.

4.3.1 Two-plate ES Antenna

The two-plate ES antenna has been previously used to launch a single electrostatic wave above the ion cyclotron frequency by Goree *et al.* in the toroidal ACT-1 device [16, 52], and by Skiff *et al.* in a linear device [17]. The two-plate ES antenna used in the BWX experiment is similar to the one used in these experiments, and is constructed from two $1\text{ cm} \times 6\text{ cm}$ molybdenum plates placed $\sim 3\text{ cm}$ apart along the magnetic field lines. The plates are oriented such that the long side and the surface normal are perpendicular to the center axis of the vacuum chamber (and the magnetic field), as shown in Fig. 4.9. The plates are attached to a movable arm that can rotate the ES antenna in and out of the plasma column, and is also free to move along the axis of the vacuum chamber. The plates could be electrically driven in or out of phase with each other by a circuit schematically illustrated in Fig. 4.10. To drive the ES antenna in phase, a coupling capacitor ($C_c = 2\mu\text{F}$) can be used to allow both plates to float with respect to the plasma potential. To drive the plates out of phase, the ES antenna is connected through a 1:1 transformer. When the plates are driven out of phase, the parallel wavenumber is controlled by the plate spacing, and when the plates are driven in phase, the parallel wavelength is determined by the vacuum chamber geometry and the antenna position inside the vacuum chamber.

During the wave launching experiments reported in the next chapter, the plates were driven by a single Wavetek 180 signal generator with a sinusoidal signal (10-300 kHz) through a Tektronix AM 501 modular op-amp either in or out of phase, as shown in Fig. 4.10. To increase the power supplied to the ES antenna during the ion heating experiments, the op-amp was replaced by a more powerful broadband ENI 2100L power amplifier with the input and output impedance of 50 Ohm.

4.3.2 Loop ES Antenna

The loop ES antenna, shown in Fig. 4.11, was constructed from four aluminum rings measuring 1 cm wide and 6.7 cm in diameter each. The rings were attached to an arm, similar

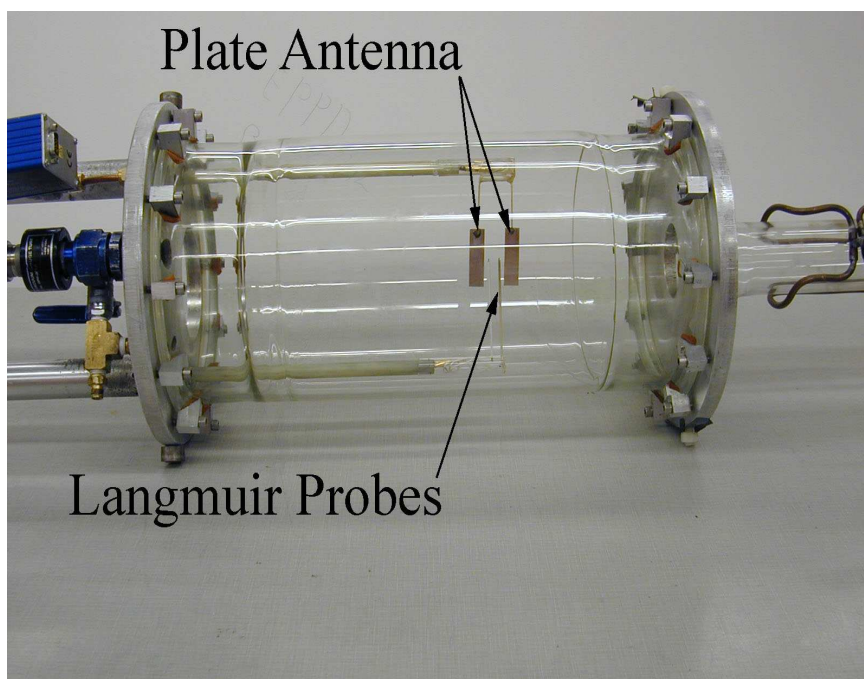


Figure 4.9: Photograph of the BWX test section showing the two-plate ES antenna attached to the moving arm. A set of Langmuir probes attached to the other arm can also be seen.

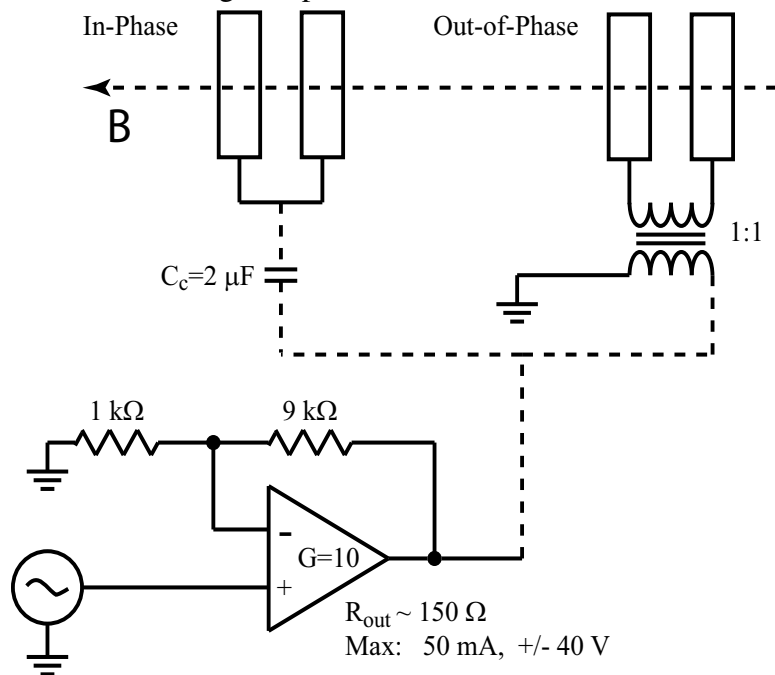


Figure 4.10: Circuit diagram of the two-plate ES antenna, signal generator, and rf amplifier. The two antenna plates can be driven in or out of phase by connecting them to the amplifier through either a capacitor or transformer.

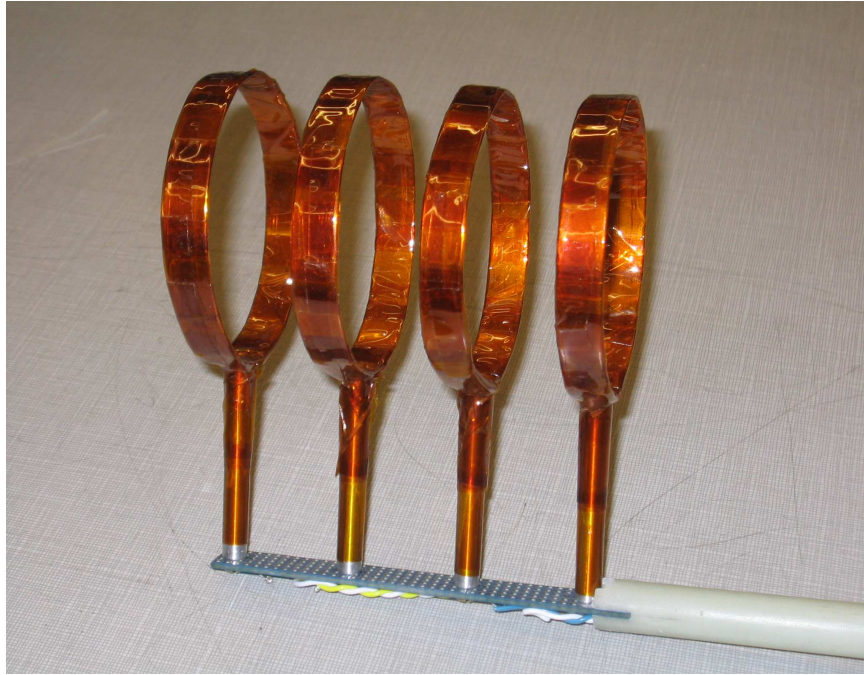


Figure 4.11: Photograph of the loop ES antenna showing its four aluminum rings. The rings are insulated from the plasma by wrapping them in Kapton tape.

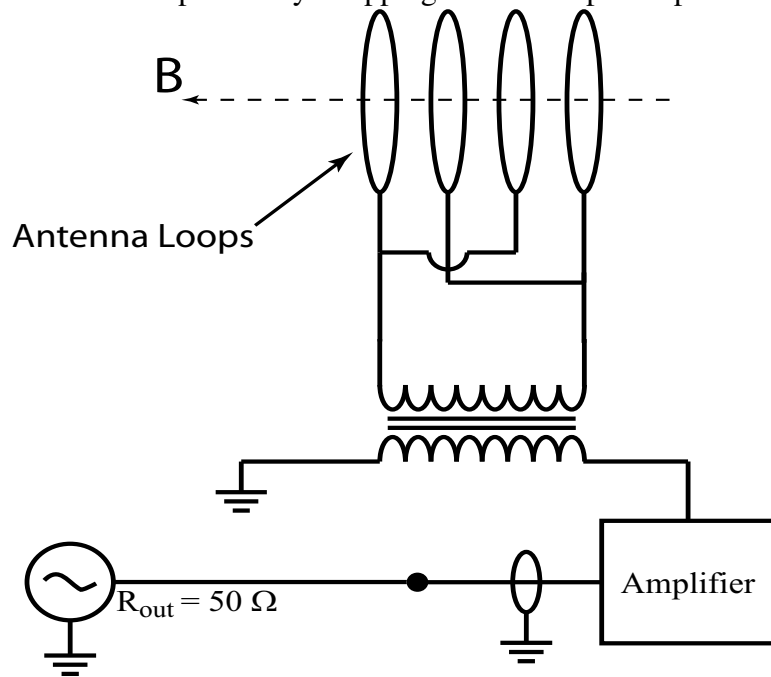


Figure 4.12: Circuit diagram of the loop ES antenna, signal generator, and rf amplifier. The rings are driven by a signal generator through an rf amplifier in either $[0, \pi, 0, \pi]$ (shown here) or $[0, \pi, \pi, 0]$ configuration. The transformer turns ratio is chosen to optimize the impedance matching between the ES antenna and the driving circuit.

to that of the two-plate ES antenna, so that the entire antenna assembly could be rotated in and out of plasma, and moved along the axis of the experiment. To prevent ohmic losses each loop was wrapped in Kapton tape. The antenna was inserted into the plasma such that the center axis of all four rings was coincident with the center axis of the experiment and the direction of the magnetic field. The spacing between the center of each loop is 3 cm. Just as with the two-plate ES antenna, the loop spacing controls the parallel wavenumber, k_{\parallel} , while the perpendicular wavenumber, k_{\perp} , is free to evolve according to the dispersion relation as a function of wave frequency and other relevant plasma parameters.

While each ring could be supplied with a voltage signal independently, the two useful configurations are $[0, \pi, 0, \pi]$, and $[0, \pi, \pi, 0]$, as described in Ref. [53]. The first configuration establishes parallel wavenumber $k_{\parallel} = 1 \text{ cm}^{-1}$ ($\lambda \sim 6 \text{ cm}$), while the second configuration establishes a larger wavelength $k_{\parallel} = 0.5 \text{ cm}^{-1}$ ($\lambda \sim 12 \text{ cm}$). In the experiments reported in this dissertation the loop ES antenna assembly was driven in the $[0, \pi, 0, \pi]$ configuration. A schematic of the electric circuit used to drive the loop ES antenna is shown in Fig. 4.12. Note that the turns ratio of the transformer in that figure is chosen to optimize the impedance matching between the ENI 2100L amplifier and the antenna.

4.3.3 Beating Waves – Mixing Signals from Two Sources

Beating electrostatic waves can be launched into the plasma by combining the output from two signal sources. This is achieved by mixing the low-power signals from the two Wavetek 180 signal generators and sending the combined output to an amplifier, as shown in Fig. 4.13. The output impedance of the signal generators and the input impedance of the amplifier is 50 Ohms. To make sure that the signal of one of the signal generators is not distorted by the other, the circuit impedance should be matched. A power combiner consisting of a 100 Ohm resistor and a tapped inductor in parallel provide good matching between the signal generators and the amplifier.

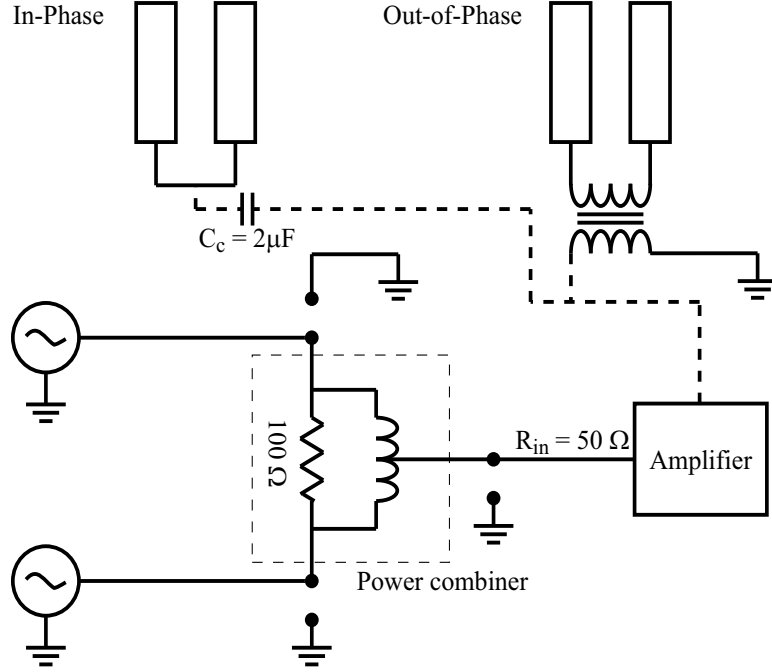


Figure 4.13: Circuit diagram for launching two waves into the plasma column. The impedance between the two signal generators and the amplifier is matched by a power combiner.

4.4 Diagnostics

The BWX diagnostics consist of rf-compensated and uncompensated Langmuir probes and a Laser Induced Fluorescence (LIF) apparatus. The Langmuir probes can be used to measure the steady-state and pulsed parameters such as the plasma density n_e , electron temperature T_e , as well as to analyze the electrostatic waves dispersion and relative amplitude. The LIF system can measure the perpendicular ion velocity distribution function, and thus yielded the ion temperature. Although this was not done for the experiments reported here, the LIF system could also be reconfigured to measure the parallel ion velocity distribution.

4.4.1 Langmuir Probes

Two types of Langmuir probes were employed to measure the steady-state plasma properties and wave propagation. The plasma density and electron temperature were determined using a radio-frequency-compensated Langmuir probe with 0.5 mm graphite tip

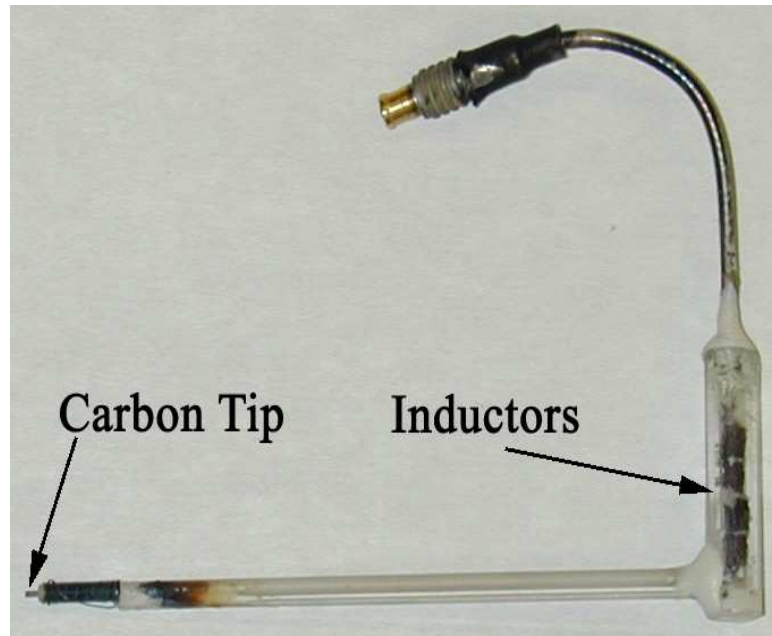


Figure 4.14: Rf-compensated Langmuir probe used to measure the electron temperature plasma density.

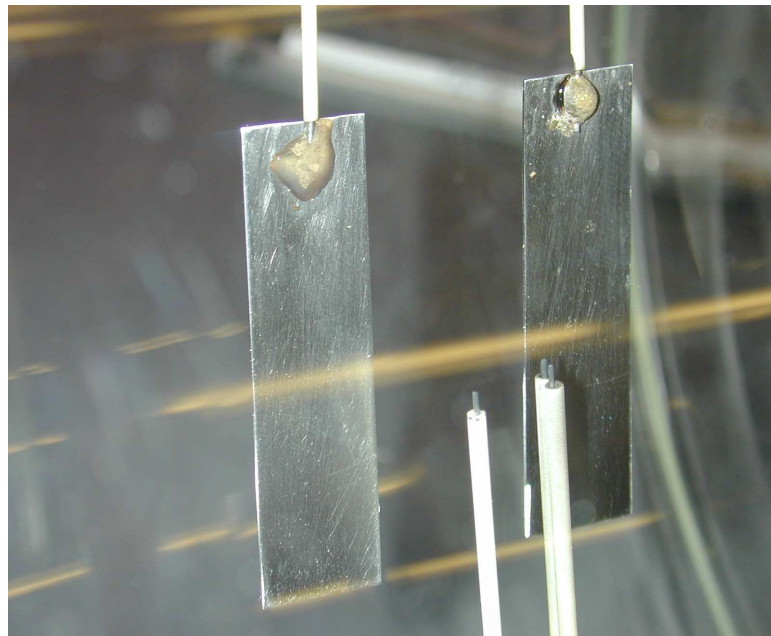


Figure 4.15: Picture of the two-plate antenna together with three Langmuir probes. The three probes can be used to measure the perpendicular and parallel components of the wavenumber as the frequency of the wave is varied.

[54], shown in Fig. 4.14. The rf compensation was achieved with four miniature inductors placed in series and close to the probe tip. The inductors were chosen to filter out the fundamental (13.56 MHz) and the second harmonic (27.12 MHz) signals of the helicon antenna. The design of the rf-compensated Langmuir probes is described by Sudit and Chen [54].

Instead of the Laframboise analysis [55] of the Langmuir probe I-V characteristic we used the empirical floating potential method developed by Chen *et al.* [56] to determine the T_e and n_e with the rf-compensated Langmuir probes in the rf-sustained plasmas.

A set of three uncompensated Langmuir probes placed orthogonally to each other were also used to measure the perpendicular and parallel wavenumber components of the propagating electrostatic wave, simultaneously. The three-probe set and its position relative to the two-plate ES antenna is shown in Fig. 4.15. Once the parallel wavenumber was established a system of two probes with T-shaped tips made of 10 mil tungsten wire were used to conduct the further studies. The T shape provided a better signal-to-noise ratio of the Langmuir probe signal.

4.4.2 Electron Temperature and Plasma Density Measurements

A Langmuir probe is the simplest plasma diagnostics device. Typically it is constructed from a thin metal or graphite rod. Langmuir probes can measure electron temperature T_e , plasma density n_e , and electron velocity distribution function $f_e(v)$.

An unbiased probe inserted into a plasma that is at some plasma potential V_p will reach a floating potential V_f . In order to measure the electron temperature and density a sweeping voltage signal is applied to the probe. The amplitude of the voltage sweep is chosen such that the current to the probe oscillates between the ion saturation current I_i^{sat} and the electron saturation current I_e^{sat} . At any point during the sweep the measured current to the probe is $I = I_i - I_e$, where I_i and I_e are the ion and electron contributions to the total current respectively. The electron current becomes negligible when the voltage is swept

below the floating potential, and the ion current reaches its saturation limit [56],

$$I_i^{sat} \approx 0.5qA_p n_e c_s, \quad (4.1)$$

where A_p is the surface area of the probe and $c_s = \sqrt{k_b T_e / m_i}$ is the Bohm velocity. Below the plasma potential, the electron current collected by the probe is exponential,

$$I_e = qn_e A_p v_{te} e^{q(V-V_p)/k_b T_e}, \quad (4.2)$$

where $v_{te} = \sqrt{k_b T_e / 2\pi m_e}$ is the electron thermal speed. The electron temperature can be inferred from the slope of $\ln(I_e)$ vs. V plot. Plasma density can subsequently be calculated from Eq. (4.1).

The method outlined above was derived for unmagnetized plasmas [55]. During the experiments described in this dissertation the plasma parameters were such that the ratio of the ion Larmor radius to the Langmuir probe radius is greater than unity, $r_{ci}/r_{probe} > 1$, implying that Eqs. (4.1) and (4.2) can be used.

An improved method of extracting T_e and n_e from the probe's I-V trace was developed by Chen *et al.* [56] specifically for the rf-compensated Langmuir probes in helicon discharges. The method is based on the empirical observation that the ion current has the following power law dependence

$$I_i = V^{3/4} \quad (4.3)$$

The equation above can be fitted to the ion saturation current region, extrapolated to the plasma potential, and then subtracted from the total current measured by the probe. The result is the electron current that can be fitted by Eq. (4.2). This method is explained in more details in Ref. [56]. Figure 4.16 shows a typical I-V trace taken in the BWX apparatus. The figure indicates that both methods give similar results. In that figure superscript "L"

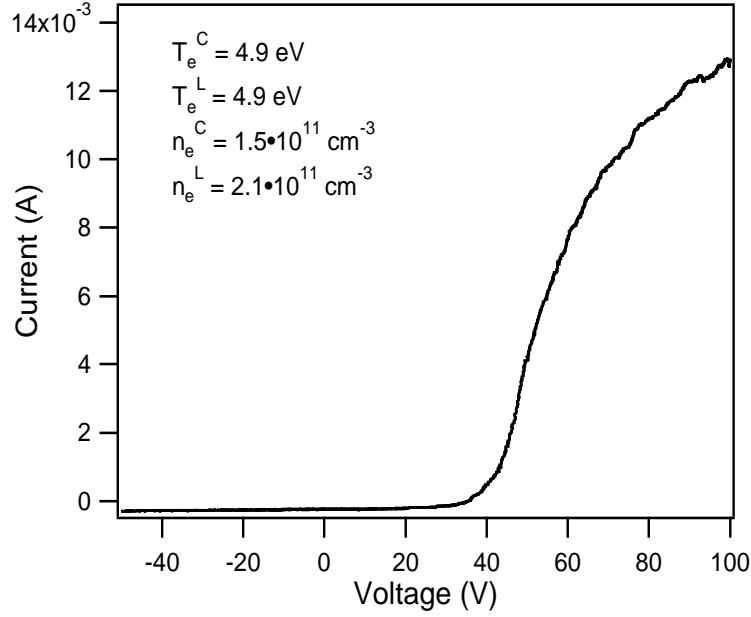


Figure 4.16: Typical I-V trace for the rf-compensated Langmuir probe. Superscript “L” refers to the Laframboise method [55] while superscript “C” refers to the values obtained using the Chen’s floating potential method [56].

refers to Laframboise method [55] while superscript “C” refers to the values obtained using Chen’s floating potential method [56]. In this dissertation we will adopt Chen’s method since it was developed specifically for rf-compensated probes and inductive plasma discharges similar to ours.

4.4.3 Dispersion Relation Measurements

An electrostatic wave is one that has no magnetic field fluctuations. According to Maxwell’s equations that leads to a curl-free electric field component,

$$\nabla \times \mathbf{E} = -\frac{1}{c} \frac{\partial \mathbf{B}}{\partial t} \Rightarrow \mathbf{k} \times \mathbf{E} = \omega \mathbf{B} = 0,$$

which means that the wavenumber is aligned along the electric field. Therefore, electrostatic waves are longitudinal in nature. Propagation of an electrostatic wave is characterized by oscillations in the local plasma density. These oscillations can be detected by a Lang-

muir probe. Thus, Langmuir probes can be used to detect electrostatic waves, analyze their dispersion relation, and measure their electric fields. Two different method involving Langmuir probes can be used to measure the dispersion relation of an electrostatic wave. For this work we used the two-probe method, however a brief description of an interferometric method is also given.

Langmuir Probe Interferometry Method

This technique requires only one Langmuir probe. The interferometric approach relies on comparing the antenna reference signal, $\sin(\omega t)$, with the signal detected by the Langmuir probe, $\sin(kx - \omega t)$, as it is moved relative to the ES antenna. The convolution of the signals, $0.5\{\cos(kx) + \cos(kx - 2\omega t)\}$, contains two spectral components. The wavenumber can be extracted from the graph of the dc component, $\sin(kx)$ vs. x .

The wavenumbers of two or more waves of the same frequency can be separated since the interferometric signal will contain a linear juxtaposition of the sinusoidal terms, $\sin(k_1x) + \sin(k_2x) + \dots$

The method outlined in this section requires an accurate probe positioning system. In addition, large distances must be traversed by the probe in order to accurately measure waves with long wavelength. Unfortunately, the dimensional constraints of the BWX system make interferometric measurements very difficult.

Two-Probe Method

A simple way to measure the dispersion relation of an electrostatic wave is to compare the phase delay between two or more Langmuir probes separated by a known distance [57]. A plane wave $A \sin(kx - \omega t)$ will introduce a phase delay

$$\Delta\phi = kd \tag{4.4}$$

between the signals from two Langmuir probes separated by a distance d . The component of the wavenumber in the direction of the probe separation can then be found as $k = \Delta\phi/d$. Figure 4.15 shows the three probe system used in the BWX experiment. The system allows simultaneous measurements of k_{\parallel} and k_{\perp} components.

It is typical for a dispersion relation to have two or more roots for a given wave frequency. Physically this means that two or more waves having different wavenumbers but the same frequency can be sustained by the plasma. In such situation the method described above may produce an erroneous measurement. This can be demonstrated by deriving the phase delay introduced between two Langmuir probes by two such waves, $\sin(k_1x - \omega t) + \sin(k_2x - \omega t)$ (assuming the waves have the same amplitude). After some simple algebraic manipulations it can be shown that the phase delay between the signals of the two probes is

$$\Delta\phi = (k_1 + k_2)d/2.$$

It is thus impossible to distinguish between the two waves. However, in our experiments this was not a problem since only one wave was observed. As will be discussed in the next chapter, this wave corresponds to the forward branch of the Electrostatic Ion Cyclotron (EIC) wave. It is possible that a wave corresponding to the backward EIC branch was also excited, but its amplitude was much smaller than that of the forward branch. As can be seen from Fig. 5.3 of the next chapter, the experimentally measured dispersion relation is in good agreement with the forward branch of the EIC wave.

4.4.4 Laser Induced Fluorescence

Various non-invasive spectroscopic plasma diagnostic techniques have been implemented since the development of lasers. One powerful and versatile technique, Laser Induced Fluorescence (LIF), can be used to measure neutral and ion temperatures, flow velocities,

plasma density, and even the dispersion relation of electrostatic waves [58, 59].

One of the first measurements of ion velocity distribution and plasma density with a non-tunable LIF system was performed by Stern and Johnson [60]. Development of tunable dye lasers allowed significant improvements and simplifications to the technique [61]. Advances in tunable diode lasers allowed construction of relatively cheap, compact, and portable LIF systems [62].

This section describes the experimental setup consisting of the portable, diode-laser LIF system built as a part of the plasma diagnostics for the BWX experiment. In addition, this section provides a brief overview of the theory behind the LIF ion velocity distribution and temperature measurements.

4.4.5 LIF Theory

The Laser Induced Fluorescence diagnostic technique is based on the Doppler shift of the ion absorption lines due to thermal motion and directed drifts. The ion velocity distribution measurement along a particular direction can be achieved by directing a laser beam along that direction. An ion observes the laser frequency ν_l that is Doppler-shifted proportionally to the ion velocity v ,

$$\nu_l = \nu_{l0} \left(1 - \frac{v}{c} \right) \quad \text{for} \quad \frac{v}{c} \ll 1, \quad (4.5)$$

where c is the speed of light and ν_{l0} is the frequency of the laser signal in the laboratory frame. When the laser wavelength is swept around an ion absorption line, the plot of absorption intensity versus the laser frequency will be proportional to the ion velocity distribution along the direction of the laser beam.

An insightful example of the technique summarized above can be made by assuming

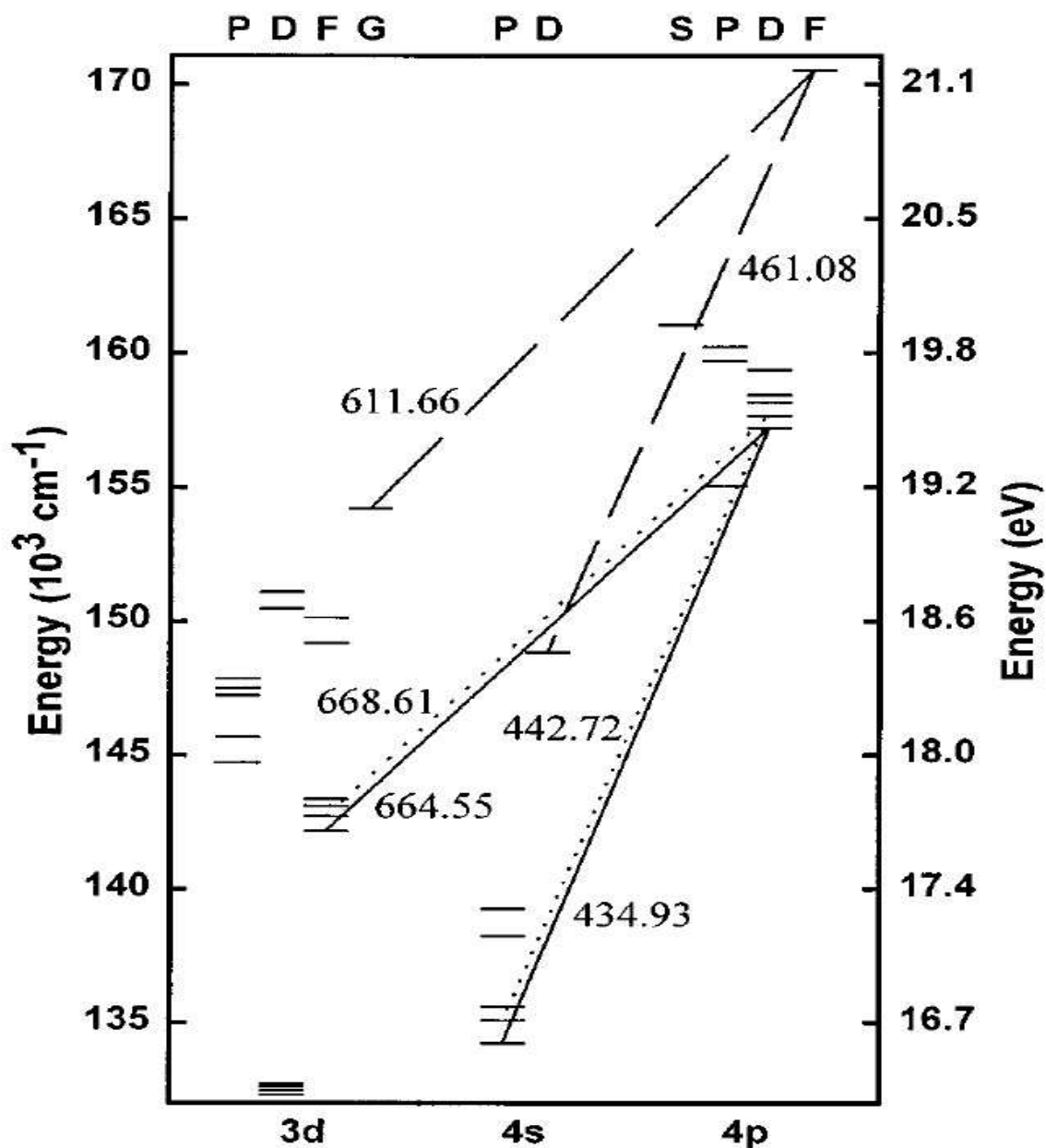


Figure 4.17: Simplified Grotrian diagram for an ArII ion. The diagram shows some possible LIF schemes. The excitation (668.61 nm) and decay (442.72 nm) lines used for the BWX experiments are shown by the dotted lines. The figure is taken from Ref. [62].

the Maxwellian non-drifting ion velocity distribution,

$$f_i(v) \sim e^{-m_i v^2 / 2k_b T_i}. \quad (4.6)$$

Rearranging Eq. (4.5) and expressing v through $\Delta\nu_l = \nu_l - \nu_{l0}$, the absorption intensity $I_l(\nu_l)$, which is proportional to the velocity distribution, can be written as,

$$I_l(\nu_l) = I_{l0} \exp \left[-\frac{\Delta\nu_l^2}{\nu_{l0}^2} \frac{m_i c^2}{2k_b T_i} \right]. \quad (4.7)$$

Thus, a fit of Eq. (4.7) to the LIF absorbtion intensity data can yield the ion temperature.

4.4.6 LIF Implementation

In practice it is difficult to measure laser light absorbtion. Instead, the laser wavelength is chosen to excite the electrons from a well populated metastable state to some unstable state. The intensity of the emitted light during the transition from the unstable state is proportional to the absorbtion intensity, and can be easily measured with a photomultiplier. The photomultiplier signal is then plotted versus the laser wavelength to yield the ion velocity distribution. Some transition lines that can be utilized for the LIF experiments with diode lasers in argon plasmas were investigated in Ref. [62] and are shown in Fig. 4.17. For the BWX experiment a scannable diode laser is tuned to 668.61 nm center wavelength. The chosen wavelength induces the $3d^4 F_{7/2} - 4p^4 D_{5/2}^0$ transition in argon ions. The $4p^4 D_{5/2}^0$ state is unstable and decays quickly to the $4s^4 P_{3/2}$ state producing 442.72 nm light.

In general, an additional experimental difficulty arises from Zeeman splitting of the transition lines due to the external magnetic field. Other broadening mechanisms, such as natural line broadening, Stark broadening, and power broadening were found to be negligible in similar rf-sustained plasmas [63]. For the perpendicular ion temperature measurements performed during the BWX experiments, the laser was aligned such that the electric field of the light was polarized along the magnetic field. Equation (4.7) can then be used

directly to deduce the ion temperature.

4.4.7 LIF Instrumentation

A schematic of the LIF system used for the BWX experiment is shown in Fig. 4.18. A 15 mW Sacher Lasertechnik Lynx tunable diode laser in the Littrow configuration is set to 668.61 nm center wavelength. The laser beam is modulated by a SRS SR-540 chopper spinning at approximately 3.5 kHz. A 10/90 beam splitter allows a Burleigh WA-1500 wavemeter to measure the wavelength of the laser beam with an accuracy of 0.2 ppm. Collection optics focuses the 442.7 nm emission light into an optical fiber which carries the signal to a Hamamatsu HC124-06MOD photomultiplier. A Stanford Research Systems SR830 lock-in amplifier further amplifies the photomultiplier signal with the chopper signal used as a reference. Laser control and data acquisition are achieved with a LabWindows/CVI code written by the WVU helicon source group [64]. For the BWX experiment the code runs on a 950 MHz PC with a National Instruments PCI-6024E and a GPIB data acquisition card through a BNC-2110 connector block and a Tektronix TDS 460A digital oscilloscope.

The LIF system can be used to measure the steady-state as well as time-resolved ion velocity distribution. The steady-state measurements are acquired directly by the computer as the laser wavelength is scanned. For the time-resolved measurements the plasma source needs to be pulsed at a known repetition rate and duty cycle. The plasma source trigger signal, as well as the low integration time signal from the lock-in amplifier, are fed into a TDS 460A oscilloscope. The controlling computer acquires the time-resolved data from the oscilloscope through a GPIB interface.

A picture of the entire LIF assembly is shown in Fig. 4.19. The entire system is small enough to fit on a portable table. The photograph shows all the components except the computer and the oscilloscope.

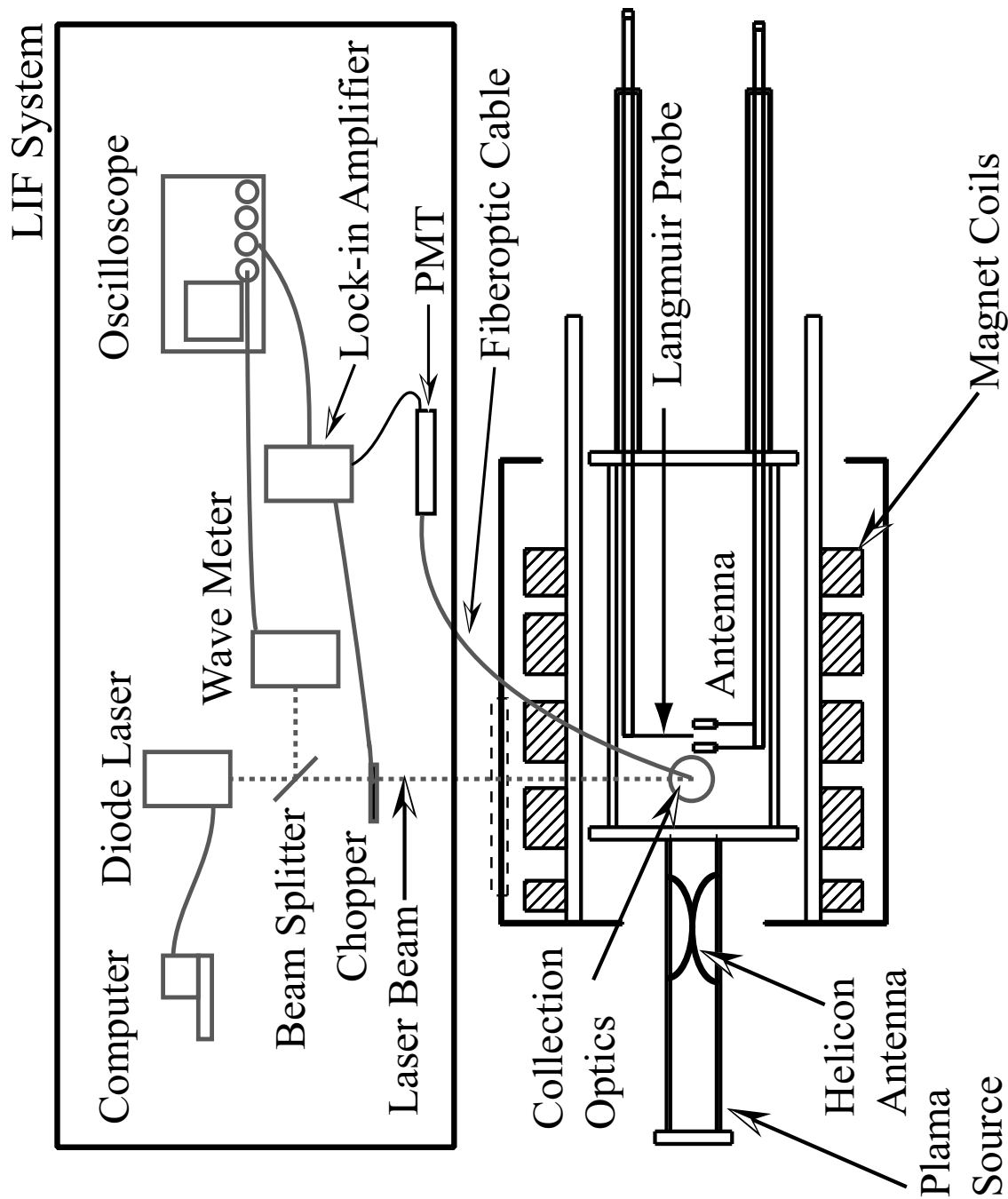


Figure 4.18: Schematic illustrating the LIF setup. The laser wavelength is controlled by a PC through an I/O card. The signal is modulated by a chopper spinning at approximately 3.5 kHz. The signal is detected and amplified by a photomultiplier. The photomultiplier signal is plotted versus the wavelength on a digital scope.

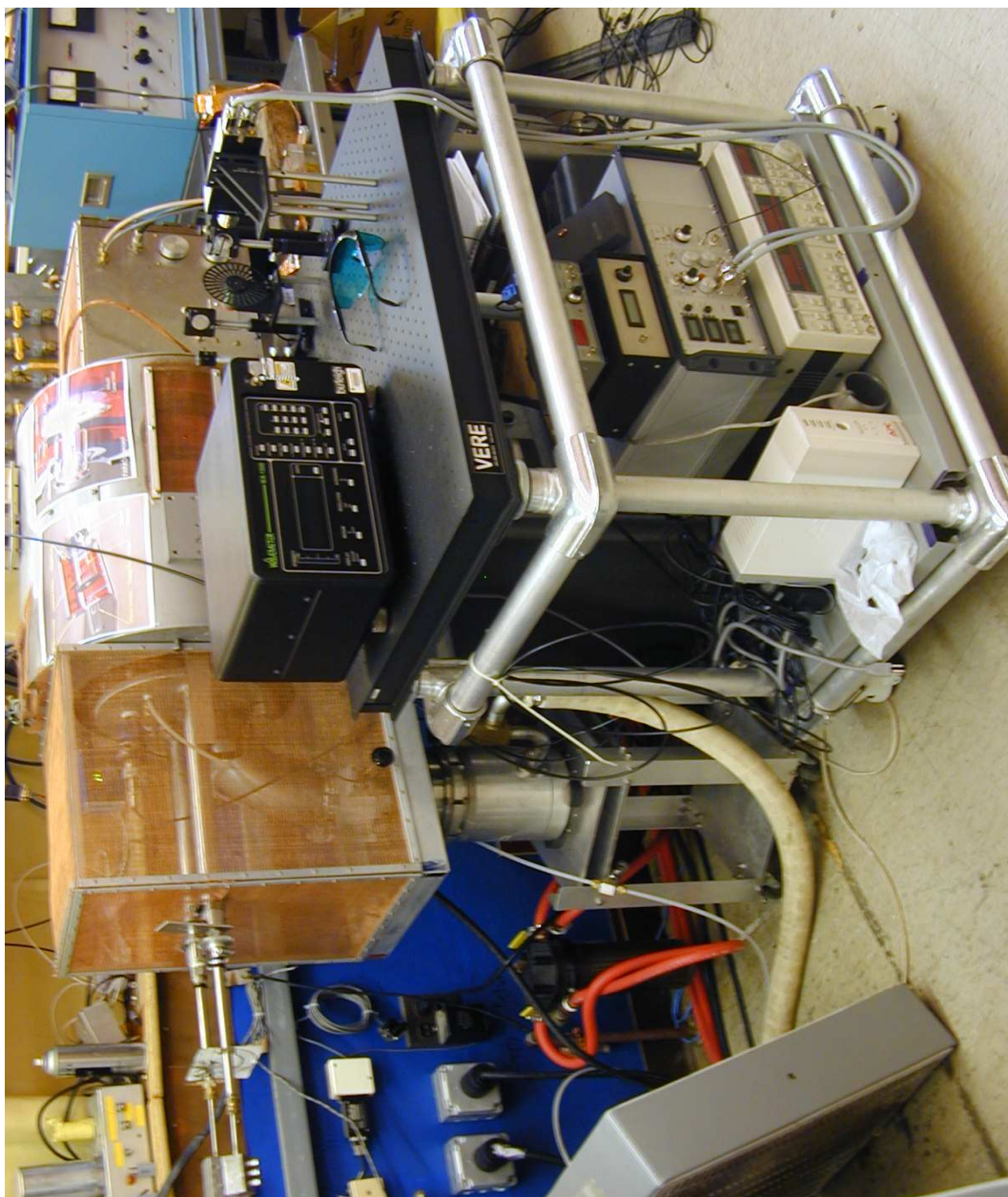


Figure 4.19: Photograph of the portable LIF system in front of the BWX experiment. The picture shows all the LIF components except the computer used to control the laser and the oscilloscope.

4.5 Operation and Procedures

The entire BWX experiment, including the helicon plasma source, can be operated in either steady state or pulsed modes. For pulsed operation, a variable voltage, 100 ms TTL pulses were produced by an HP8116A function generator at 5 Hz and 50% duty cycle. The signal controls the ENI OEM-12A RF power supply, which is used as a power source for the helicon antenna. The same signal can be used as a gate signal for the time-resolved LIF measurements. In addition, the function generator controls a DDG DG565 where the signal can be delayed by an arbitrary amount to trigger the Langmuir probes, ES antenna or other equipment. Most of the experiments were performed with 125 W of rf power to the helicon antenna and only a few watts reflected. The wave launching and time-resolved ion heating experiments were conducted with at least a 30-ms delay from the time the helicon antenna is triggered to ensure that all plasma parameters have reached their steady-state values [65].

Unless stated otherwise, the steady-state LIF measurements were composed of three laser scans. Typical voltage applied to the photomultiplier varied from 600 to 750 volts. For the time-resolved measurements the lock-in integration time was set to 3 ms and each time-resolved wavelength line was averaged over 100 shots.

Chapter 5

Experimental Results and Analysis

I have not failed. I've just found 10,000 ways that won't work.

– Thomas Alva Edison

This chapter presents and analyzes the data collected during the experimental investigation of the ion heating by beating electrostatic waves. The experiments consisted of two main components. First, dispersion properties of electrostatic waves, which were launched from the two-plate ES antenna into a magnetized plasma column, were characterized. In order to investigate the BEW ion heating mechanism, we needed to ensure that the electrostatic waves propagate in the plasma column at an angle close to 90° relative to the external magnetic field, since we limited our theoretical study in Chapter 2 to propagation perpendicular to magnetic field. Single particle acceleration by oblique beating electrostatic waves has been studied by Strozzi *et al.* [34]. They found that, as long as both beating waves have equal parallel wavenumber, and the angle of propagation is close to 90° , the regular acceleration region remains connected to the stochastic acceleration region, similarly to what was found for the case of perpendicular propagation, which was presented in Chapter 2. Measurements of the wave dispersion relation confirmed the electrostatic nature of the waves and determined the angle of their propagation.

The second component of the study involved measurements of the perpendicular ion

temperature increase in the presence of the electrostatic waves. Three different measurement techniques were attempted. A Retarding Potential Analyzer (RPA) could not provide a reliable perpendicular ion temperature measurement because the ion Larmor radius in the BWX experiment was on the order of the RPA thickness. Ion temperature can also be inferred from the dispersion properties of the backward branch of the Electrostatic Ion Cyclotron (EIC) wave [18]. However, with the available diagnostics we only observed the forward branch of the EIC wave. We were able to successfully measure the perpendicular ion temperature, using the Laser Induced Fluorescence (LIF) system, described in Chapter 4. Therefore, only the results of the perpendicular ion temperature measurements performed with the LIF technique are reported in this chapter.

In the following section we present and analyze the ES antenna circuit response during the wave-launching experiments. In Section 5.2 we describe the electrostatic wave dispersion and propagation properties in our rf-sustained, magnetized plasma. Effects of ion-neutral collisions on wave propagation are described in Section 5.3. Ion heating by a single and beating electrostatic waves are then compared and contrasted in Section 5.4. Finally, in Section 5.5 we offer some concluding remarks.

5.1 Wave Detection

We conducted the wave dispersion relation studies with the two-plate ES antenna because this antenna coupled better to the plasma than the loop antenna. The waves were detected with a set of uncompensated Langmuir probes with either cylindrical carbon tips or tungsten T-shape tips. A set of three carbon-tipped probes is shown next to the two-plate ES antenna in Fig. 4.15. The circuit used to launch a single electrostatic wave from the two-plate ES antenna into the plasma column is shown in Fig. 4.10. Figure 5.1 shows typical fourier-transformed voltage signals a) driving the ES antenna, b) detected by a Langmuir probe in our plasma, and c) AC coupling between the ES antenna and the Langmuir probe

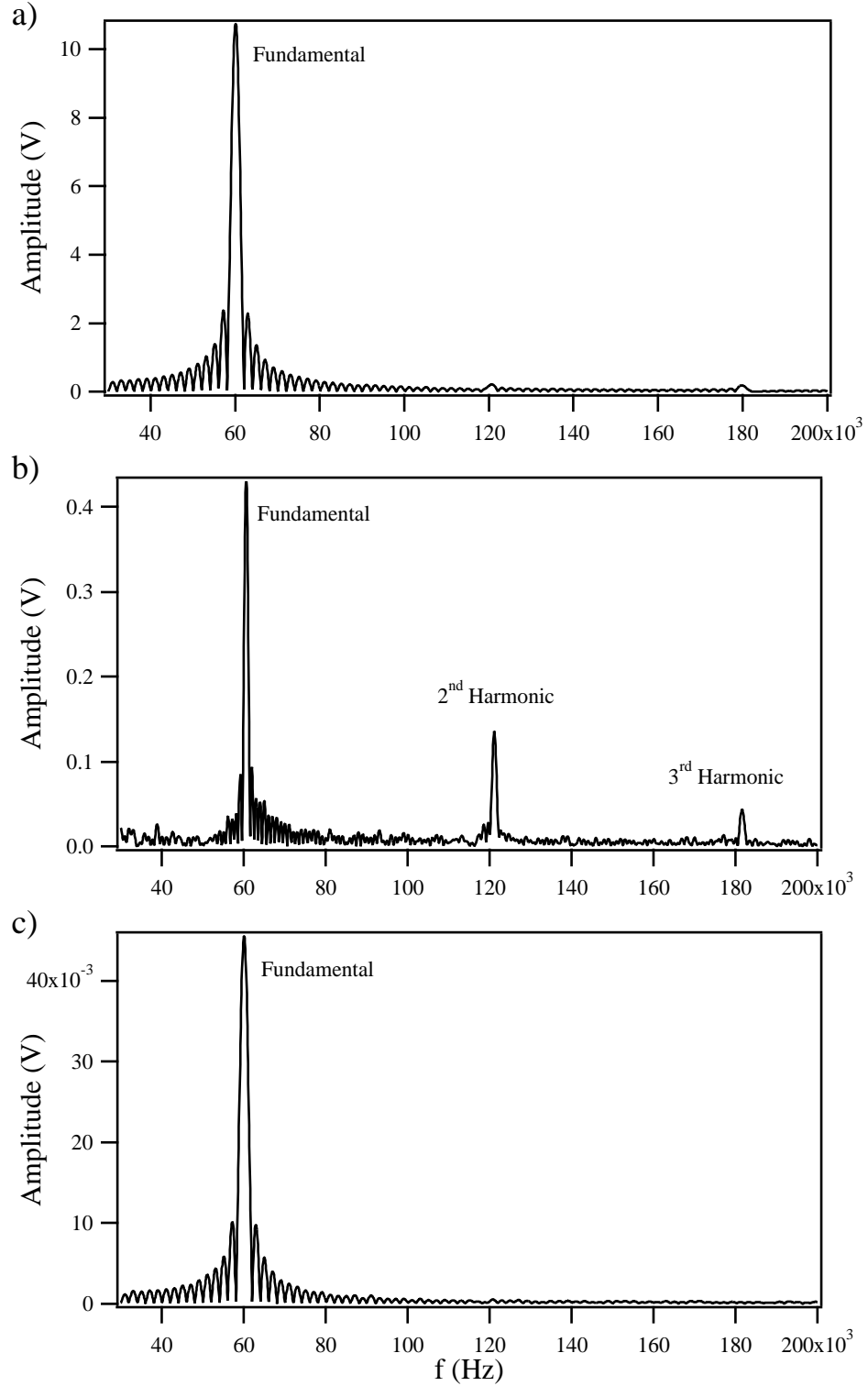


Figure 5.1: Magnitude of the Fourier transform of a typical a) voltage signal to the ES antenna, b) Langmuir probe signal, showing also the second and third harmonics of the excited wave in the plasma, and c) Langmuir probe signal with plasma turned off. The signal is due to the AC coupling between the ES antenna and the Langmuir probe.

without the plasma. The figure indicates that the AC coupling between the antenna and probe is an order of magnitude below the plasma wave signal, and thus AC coupling does not affect the plasma wave measurements.

To ensure efficient wave generation we needed to maintain good coupling between the ES antenna, its driving circuit, and the plasma. By choosing the appropriate plasma parameters that maximize the amplitude of the launched electrostatic wave for a given input power to the ES antenna we can optimize the coupling. For a fixed magnetic field and neutral pressure, the plasma impedance varies with the plasma density, i.e. with the rf power delivered to the helicon antenna. Therefore, the power delivered to the ES antenna can be correlated with the helicon antenna power.

In order to investigate the wave launching conditions we conducted the following experiment. The signal generator and the op-amp in Fig. 4.10 were set to produce a 30-Volt sinusoidal signal ($f = 60$ kHz). A magnetized argon plasma with $n_e = 10^9 - 10^{13} \text{ cm}^{-3}$ and $f_{ci} = 30$ kHz was produced by the helicon antenna at various rf powers with the chamber neutral pressure of 1 mTorr. Measuring the ES antenna's voltage and current simultaneously we were able to determine the impedance and power delivered to the antenna plates as a function of the rf power delivered to the helicon antenna. A Langmuir probe inserted into the plasma column measured the amplitude of the launched waves.

As was mentioned in the previous chapter, the plates of the two-plate ES antenna could be driven in or out of phase with each other. We found that for the in-phase configuration the maximum power to the ES antenna plates is delivered when the helicon antenna power is 100-200 W, as shown in Fig. 5.2a. The amplitude of the Langmuir probe signal peaks at ~ 250 W of rf power, when the real component of the measured impedance (Z_r) approaches 150Ω , which is the output impedance of the op-amp used in this experiment, and the imaginary part (Z_i) is small. At that condition the entire circuit is closely matched.

A similar experiment was repeated with the antenna plates driven out of phase. The results are shown in Fig. 5.2b. The maximum power in this case is about 75% of that

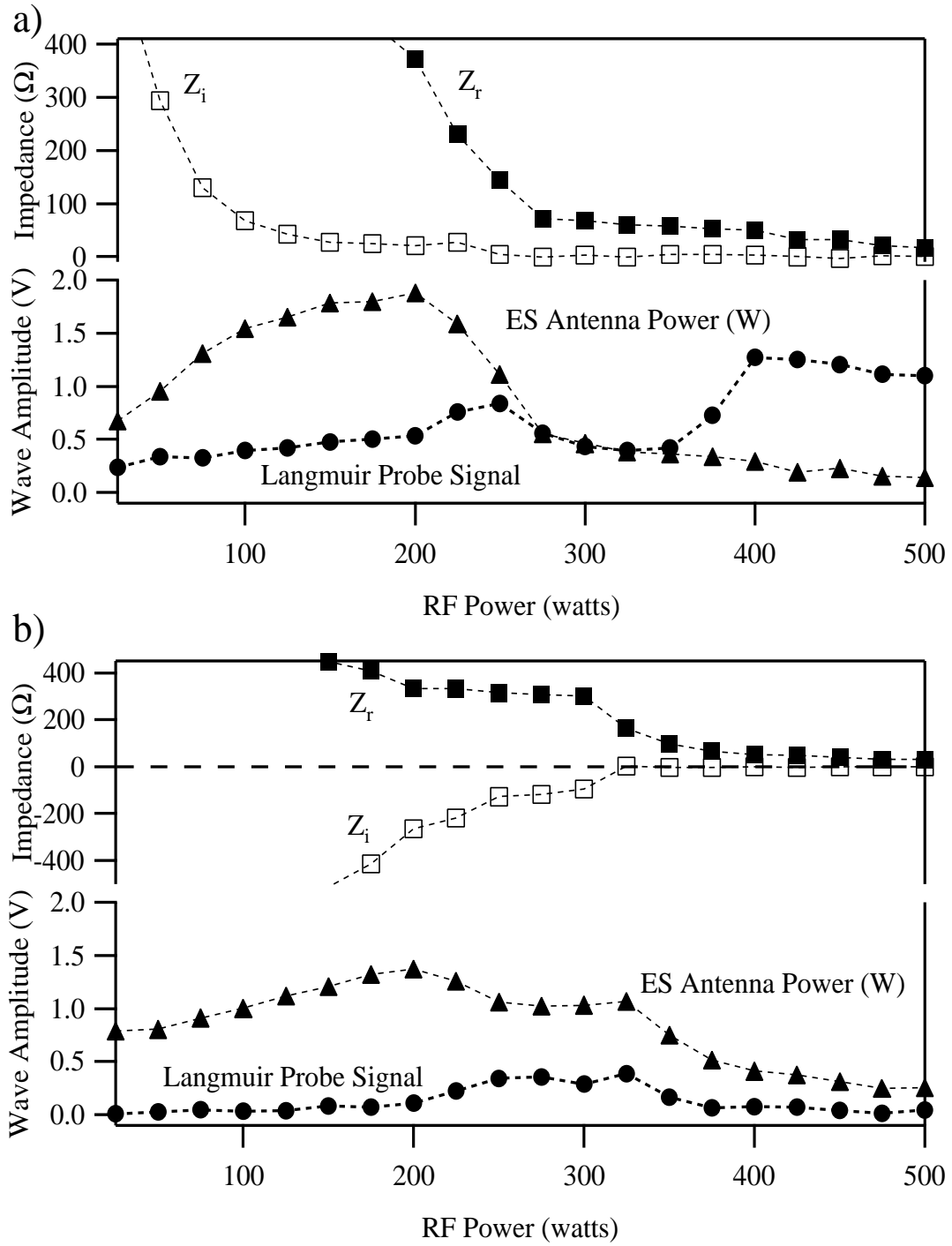


Figure 5.2: The amplitude of the launched ES wave (measured by the Langmuir probe) as well as the impedance and the power delivered to the ES antenna are shown as functions of rf power to the helicon antenna. The real and imaginary components of the ES antenna impedance are designated by Z_r and Z_i respectively. a) Both plates are driven in phase. b) The plates are driven out of phase.

delivered to the ES antenna driven in phase. Also, the wave amplitude detected by the Langmuir probe is significantly lower than the amplitude of the wave launched by the plates driven in phase. Possible reasons for this are given in the next section. However, as in the previous case, the maximum in wave amplitude corresponds to the matched circuit condition, $Z_i \ll Z_r \sim 150 \Omega$.

The in-phase driven antenna couples better to the plasma, resulting in a wave with a higher amplitude than the out-of-phase driven antenna. We therefore undertook further study of the in-phase configuration. The goal of the study was to determine whether the launched wave is electrostatic in nature and whether it propagates transversely to the magnetic field.

5.2 Dispersion Relation Measurements

Linear electrostatic dispersion relation for a collisional, homogenous, isotropic, non-drifting, and infinite plasma with finite electron and ion temperature, can be derived from the Vlasov equation by including the BGK collision term as described by Choueiri, who performed a similar derivation for unmagnetized ions [66, 67]

$$-i(\omega - k_z v_z - k_\perp v_\perp \cos \theta + i\nu)f_1 + \omega_c \frac{\partial f_1}{\partial \theta} = \frac{iq}{m} \mathbf{k} \Phi \cdot \nabla_v f_0 + \nu \frac{n_1}{n_0} f_0, \quad (5.1)$$

where f_0 , n_0 , f_1 , and n_1 are the zeroth and first order perpendicular ion velocity distribution functions and particle densities respectively, θ is the angle between the wave propagation and the external magnetic field, and Φ is the electric potential. After some manipulations the first order distribution function can be expressed as

$$f_1 = \frac{q}{T} f_0 \sum_n \sum_m \frac{J_n\left(\frac{k_\perp v_\perp}{\omega_c}\right) J_m\left(\frac{k_\perp v_\perp}{\omega_c}\right) e^{i(n-m)\theta}}{w + i\nu - n\omega_c - k_z v_z} \left[(k_z v_z + n\omega_c) \Phi + i\nu \frac{n_1}{n_0} \frac{T}{q} \right]. \quad (5.2)$$

The equation above can be integrated over the velocity space to obtain n_1 , and then used in Poisson's equation to yield the ES dispersion relation

$$1 + \sum_s \alpha_s \frac{1 + e^{-\mu_s} \xi_{0s} \sum_n I_n(\mu_s) Z(\xi_{ns})}{1 + i(\nu_s/k_z v_{ts}) e^{-\mu_s} \sum_n I_n(\mu_s) Z(\xi_{ns})} = 0, \quad (5.3)$$

where subscript s refers to the type of the charged species, $\alpha_s = 1/k^2 \lambda_{Ds}^2$, λ_{Ds} is the Debye length, $\mu = k_\perp^2 v_t^2 / 2\omega_c$, and $I_n(\mu)$ is the modified Bessel function of the first kind. It could be easily checked that upon setting ν_s to zero, Eq. (5.3) reduces to the familiar collisionless electrostatic dispersion relation, e.g. Eq. (85) given by Stix in Ref. [68]. A more detailed derivation of Eq. (5.3) is given in Appendix F.

To launch an electrostatic ion cyclotron (EIC) wave above the ion cyclotron frequency the following conditions must be satisfied [16],

$$\begin{aligned} \omega_{pi} &> \omega_{ci}, \quad T_i \lesssim T_e, \\ (2T_i/m_i)^{1/2} &\ll \omega/k_\parallel \ll (2T_e/m_e)^{1/2}. \end{aligned}$$

In the reported experiments the following parameters were measured $T_e \sim 3$ eV, $T_i \sim 0.1$ eV, $B = 261$ Gauss, $\omega = 30 - 180$ kHz, and $\lambda_\parallel \approx 46$ cm, and therefore the above inequalities are satisfied. The numerical solution of Eq. (5.3) for the plasma parameters in our experiment is shown in Fig. 5.3. The first panel in that figure shows the solution to Eq. (5.3) in the collisionless limit ($\nu_s = 0$), while the second panel includes the ion-neutral collisional effects (these will be discussed in the next section). In additions, Fig. 5.3b shows the experimentally measured dispersion.

According to Eq. (5.3), two wave modes can propagate in the neighborhood of the ion cyclotron frequency. The first mode is a forward branch of the EIC wave (ω/k_\perp parallel to $\partial\omega/\partial k_\perp$) with a relatively large wavelength ($\lambda_\perp \sim 6$ cm). The other mode is the backward branch of the EIC wave (ω/k_\perp antiparallel to $\partial\omega/\partial k_\perp$) with the perpendicular wavelength on the order of the ion Larmor radius. The latter branch is also sometimes referred to as the

Neutralized Ion Bernstein Wave (NIBW). In both panels of Fig. 5.3 the forward branch of the EIC and four branches of the NIBW waves are shown by thick lines. The line with the short dashes shows the imaginary part of the perpendicular wavenumber for the forward EIC branch. This wave is weakly damped. On the other hand, the lines with the longer dashes represent the imaginary part of the wavenumber for the NIBW. A large negative imaginary component close to the wave harmonics in Fig. 5.3a indicates that this wave is highly damped at the exact resonances. However, away from the resonance $k_i/k_r \ll 1$ the wave can propagate freely from the ES antenna. Indeed, both the forward and backward branches of the EIC wave have been observed by Skiff *et al.* [17], Alba *et al.* [18], Goree [52], and others in discharges with low neutral density ($\nu_{in}/\omega_{ci} \leq 0.02$). As can be seen from Fig. 5.3b, only the forward branch of the EIC wave could be detected in the BWX machine with our diagnostic method.

The dispersion relation for the forward branch of the EIC wave can also be derived from the fluid equations as [13],

$$\omega^2 = \omega_{ci}^2 + v_{ti}^2 k_{\perp}^2, \quad (5.4)$$

where v_{ti} is the ion thermal speed. As can be seen from this expression, the slope of the forward branch of the EIC dispersion is sensitive to the electron temperature. Thus, comparing the experimentally measured dispersion relation to the theoretical expression provides a good check of the electron temperature. The electron temperature inferred by the slope of the experimental dispersion relation, $T_e = 2.75$ eV, is in good agreement with the values measured independently with the rf-compensated Langmuir probe, shown in Fig. 4.6. Additionally, just as the forward branch of the EIC dispersion relation is sensitive to the electron temperature, the backward is sensitive to the ion temperature [69]. However, since we could not detect the backward branch with our diagnostic methods, the ion temperature in our experiments had to be measured with an alternative method – the LIF.

As was mentioned above, the theoretical dispersion relation given by Eq. (5.3) was derived for an idealized plasma. Some relevant plasma parameters are shown in Fig. 4.8. It can be seen that the plasma is collisional ($\nu_{ei}, \nu_{ii} > f_{ci}$). Also, the density profiles shown in Fig. 4.6 indicate that the plasma is not homogeneous, $(a/n)\partial n/\partial x \gtrsim 1$, specifically at high rf power. Another point of concern is the effect of the plasma boundaries. At low values of k_{\perp} (long wavelength) the effect of the boundaries can be significant and the experimental data might diverge from the theoretical prediction. With these considerations in mind, Fig. 5.3b shows a good agreement between the experiments and the theory for a wide range of frequencies.

The experimental dispersion was obtained in the following manner. A single sinusoidal wave was launched by the two-plate ES antenna driven in the in-phase configuration, and inserted at the edge of the plasma column. We measured the wave dispersion by a system of three uncompensated Langmuir probes. The probes were placed orthogonally to each other so that simultaneous determination of k_{\perp} and k_{\parallel} could be performed by measuring the signal delay between any two probes [57]. This setup is shown in Fig. 4.15. Measuring the probe signal with the plasma discharge off we determined that the ac-coupling between the ES antenna and the probes was very small (an order of magnitude below the wave signal with the plasma turned on, as shown in Fig. 5.1b and c).

The parallel component of the wavenumber, measured by the two probes placed along the magnetic field, indicated that the parallel wavelength of the wave is 46 cm – the length of the large glass cylinder. The measured perpendicular wavenumber, shown in Fig. 5.3b, varies in accordance with the forward branch of the EIC wave dispersion. The error of the measurements, shown by a horizontal bar in the lower right corner of the figure, was calculated from multiple (10–30) measurements at the same conditions. The dispersion measurements at frequencies up to $\omega/\omega_{ci} = 10$ indicate that the wave propagates at the angles of 82° to 86° with respect to the magnetic field. It should be noted that, while theoretical work presented in Chapter 2 strictly applies only to the perpendicular wave

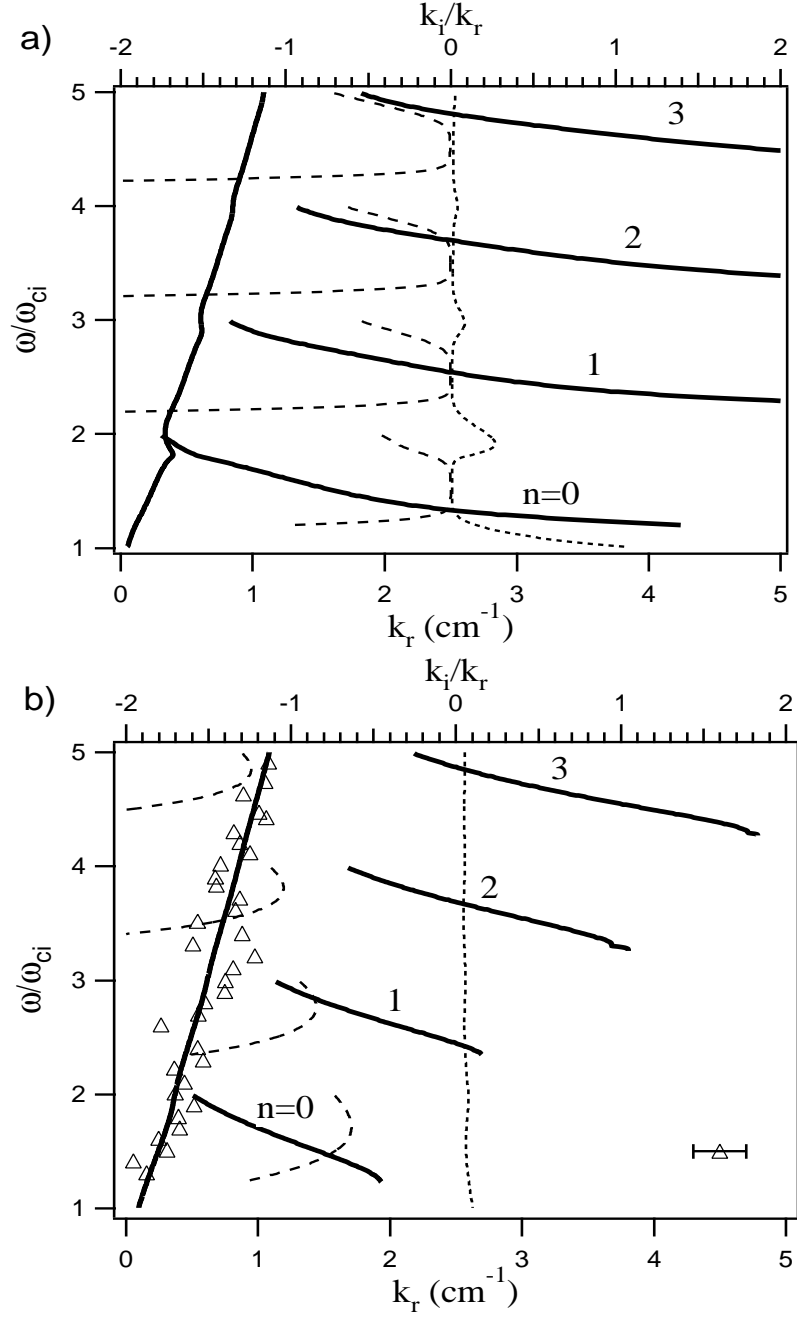


Figure 5.3: Electrostatic dispersion relation for the waves propagating in an argon plasma slightly above the ion cyclotron frequency obtained from Eq. (5.3) for a) collisionless plasma, b) a plasma typical to the BWX experiment, including ion-neutral collisions at 1 mtorr. The thick black lines show the wave frequency as a function of the real component of the wavenumber, while the dashed lines show the wave frequency as a function of the imaginary component of the wavenumber (top scale). Experimentally measured dispersion relation (Δ) is also shown. Other plasma parameters common to both a) and b) are $B=261$ G, $T_e=3$ eV, $T_{i\perp}=0.11$, and $k_{\parallel}=0.14 \text{ cm}^{-1}$.

propagation, recent theoretical work by Strozzi *et al.* [34] shows that we should expect the BEW heating mechanism to exist even when the waves propagate obliquely with respect to the magnetic field, as long as the waves have the same wavenumber. This is indeed the case in our experiment since both beating waves were launched from the same antenna simultaneously. For both waves, the parallel wavenumber was established either by the plate spacing or the physical dimensions of the chamber.

We should also note that when the antenna plates were driven out of phase, the measured dispersion relation did not follow the theoretical dispersion relation for the EIC wave. According to the previous discussion, we expected the parallel wavelength for the out-of-phase configuration to be 6.28 cm – twice the spacing between the plates. However, the measured parallel wavelength was on the order of the chamber length, similar to the in-phase configuration. While we have not investigated this in detail, it is possible that the wave propagation was affected by the closeness of the conducting end-plates of the vacuum chamber or by ion Landau damping since, for that configuration, $w/k_{\parallel} \sim v_{ti}$. For the experiments presented in the following sections we, therefore, used only the in-phase configuration.

5.3 Effects of Ion-Neutral Collisions

As we have discussed earlier, the effects of ion-neutral collisions can be investigated by including the BGK collisional operator into the Vlasov equation. For argon, at temperatures and densities typical to the BWX experiment, the charge-exchange and ion-neutral elastic scattering collision cross-sections are on the order of $\sim 10^{-14} \text{ cm}^2$ [70, 71], and the total ion-neutral collision frequency can be estimated to be $\sim 1.5 \times 10^4 \text{ s}^{-1}$. Therefore, in our experiment $\nu_{in}/\omega_{ci} = 0.2$, which is an order of magnitude higher than in Skiff's experiment [17]. Even though the ratio of ion-neutral collisions to the ion cyclotron frequency is small ($\nu_{in}/\omega_{ci} < 1$), we now show that the collisions nevertheless significantly alter the EIC wave

propagation.

When ion-neutral collisions are taken into account in the dispersion relation, the backward branch of the EIC wave becomes highly damped at all frequencies. Figure 5.3b shows solutions to Eq. (5.3) that include ion-neutral collisions. Note that collisions have little effect on the real part of the forward branch of the dispersion relation. While the forward branch of the EIC wave is mainly unaffected, the imaginary part of the NIBW wavenumber grows significantly. For example, with $\omega/\omega_{ci} = 1.5$ the imaginary part of the wavenumber, k_i , increases by three orders of magnitude to $k_i \sim k_r$ (k_r is the real part of the wavenumber), as compared to the collisionless case. Thus, for our collisional plasma we expect the backward branch of the EIC wave to be damped within a short distance away from the ES antenna. As was mentioned above, we did not observe the backward branch of the EIC wave. However, the experimental dispersion relation, shown in Fig. 5.3(b) by triangles, is in a good agreement with the solutions to Eq. (5.3) for the forward branch of the EIC wave.

For the conditions of our experiments, with the plate antenna driven in phase, we were able to launch the forward branch of EIC, which despite the attenuating effect of ion-neutral collisions propagates in the vicinity of the antenna. While we were only able to measure the dispersion relation of the forward branch, it is possible that the heating reported in the next section could be due to the backward branch, whose amplitude may have been too small to detect by our diagnostic, because it is known to have better coupling with the ions.

5.4 Ion Heating in the BWX

The NIBW mode interacts with ions much stronger than the forward branch of the EIC wave, because its wavelength is on the order of the ion Larmor radius. Therefore, to observe any significant ion heating by an electrostatic wave in a warm, dense discharge, either the amount of power to the ES antenna or the magnetic field should be increased. The former increases the amount of power transferred from the waves to the ions. The latter decreases

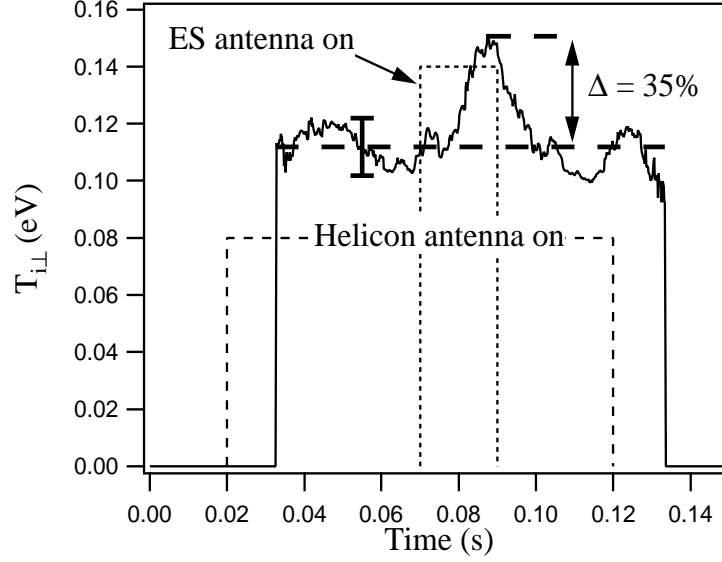


Figure 5.4: Ion temperature evolution for a 100 ms plasma pulse. A steady-state plasma is established 15 ms after the rf power is applied to the helicon antenna. Perpendicular ion temperature increases by $\sim 35\%$ when an electrostatic wave propagates from the two-plate ES antenna. When the two-plate ES antenna is turned off the ion temperature returns to its ambient level.

the ratio ν_{in}/ω_{ci} , thus making the plasma less collisional, allowing the NIBW to propagate. The magnetic field in the BWX experiment is limited by the amount of the current available from the magnet power supply. To reduce ν_{in}/ω_{ci} to an acceptable level in our experiment, the magnetic field should be increased to at least 0.3 T, which is three times the amount available. Therefore, we have chosen the route of increasing the power by amplifying the signal to the ES antenna. We have observed ion heating with the two-plate and the loop ES antennas. The heating with the two-plate ES antenna was more pronounced than heating with the loop ES antenna because more power could be transferred to the plasma from the former than the latter.

We first performed a time-resolved study of ion heating by a single electrostatic wave launched by the two-plate ES antenna. For this study, all plasma parameters were similar to the experiments described in Refs. [64] and [72]. The plasma was created by sending a 100 ms, 125 W rf pulse to the helicon antenna. The two-plate ES antenna was turned on for 20 ms with a delay of 50 ms (to ensure that the plasma has reached a steady state), as shown in

Fig. 5.4 by the dashed boxes. For the first 15 ms after the helicon antenna was turned on we observed a population of fast ions propagating through the plasma column. The velocity distribution of this population was found not to be Maxwellian, and thus a perpendicular ion temperature could not be established. The plasma reached a steady state after about 15 ms with an average temperature of 0.11 eV, shown by the thick dashed horizontal line in Fig. 5.4. The uncertainty in the temperature measurement can be determined from the temperature fluctuation when the two-plate ES antenna is off. Analysis shows that this error, shown by the vertical bar in Fig. 5.4, is ~ 0.01 eV or 10%. We have also confirmed this uncertainty through a series of repeated steady-state ion temperature measurements with the two-plate ES antenna turned off.

When the ES antenna was turned on, we observed significant rise in the ion temperature. Figure 5.4 shows a 35% temperature increase. However, this increase is an order of magnitude below that reported by Skiff *et al.* [17] in a less collisional plasma of a Linear Magnetized Device, but on the same order as reported by Kline *et al.* [73, 74] in an rf-sustained plasma. This is not surprising since we expect ion-neutral collisions to play an important role in damping the waves.

Ion heating was observed within only a short distance from the two-plate ES antenna. While the position of the antenna relative to the LIF measurement volume could not be precisely controlled, we observed a sharp increase in the ion temperature as the ES antenna was moved within half a centimeter of the LIF laser beam. This observation qualitatively supports prediction of the collisional dispersion relation in Fig. 5.3b.

Next, we performed a study of the beating wave ion heating in a steady-state plasma. Time-resolved measurements are quite time consuming; it takes about 30 minutes to obtain a time-resolved ion temperature profile with 31 different laser wavelengths. A small drift in the helicon antenna tuning may change plasma parameters over this period. This renders the time-resolved measurements impractical for comparison between different scans. On the other hand, a measurement of a steady-state plasma with 300 different wavelengths can

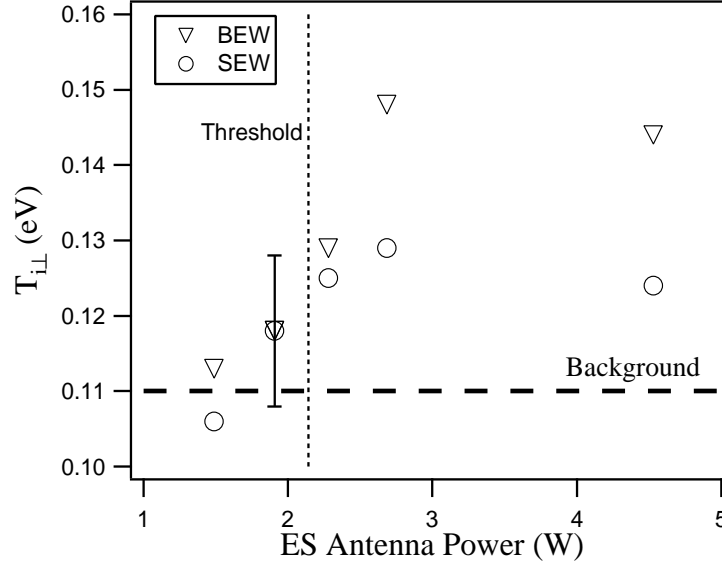


Figure 5.5: Results of the BEW (∇) and SEW (\circ) ion heating experiments. The background perpendicular ion temperature is 0.11 eV, and is shown by the thick dashed line. The plot shows a heating threshold in wave power (amplitude) at about 2 W above which there is significant heating for both BEW and SEW schemes. The data also indicates a threshold at about 2.5 W above which the perpendicular ion temperature is higher for the BEW heating scheme.

be performed under 30 seconds. For this experiment we have compared ion heating by a single electrostatic wave with $\omega = 3.5\omega_{ci}$ to that resulting from two beating waves with $\omega_1 = 3.5\omega_{ci}$ and $\omega_2 = 4.5\omega_{ci}$. To ensure that the comparison is valid we set the total power for both beating waves to be the same as that for the single wave. Figure 5.5 shows the results of these experiments as a function of power delivered to the ES antenna. Each data point is an average of three measurements.

Experiments revealed a threshold in the ES antenna power (wave amplitude) at about 2 W, above which there is a significant ion heating for both single and beating waves, as shown in Fig. 5.5. Power to the ES antenna was calculated by the simultaneous measurements of the oscillating current and voltage delivered by the amplifier. When the ES antenna power was below 2 W we did not observe ion heating with either single or beating electrostatic waves. As the antenna power was increased above 2 W, ion temperature also increased for both SEW and BEW heating mechanisms. This behavior can be ex-

plained with the help of the wave-amplitude threshold (not to be confused with the velocity threshold) derived from the single-particle model developed by Karney [28], and given by Eq. (2.8a), quoted here for convenience,

$$E/B = \frac{1}{4}(\omega_{ci}/\omega)^{1/3}(\omega/k_{\perp}). \quad (5.5)$$

Using this equation we can determine the electric field amplitude of the wave at the threshold. Then, from Fig. 5.2a we can estimate the minimum ES antenna power needed to observe the ion heating. For the parameters of our experiments, the amplitude of the electric field at the threshold determined by Eq. (5.5) is 0.14 V/cm. With the wavenumber of 0.7 cm^{-1} (from Fig. 5.3 at $\nu = 3.5$) this corresponds to 0.6 V of the probe signal. Figure 5.2a shows that, at 125 W of RF power, and with ~ 1.5 W of power into the ES antenna, the Langmuir probe signal is 0.42 V. A simple extrapolation of that signal to 0.6 V gives 2.14 W needed at threshold. This threshold is shown in Fig. 5.5 by a vertical dashed line, and is in good agreement with the power above which ion heating is observed shown in 5.5. Similar threshold behavior was observed by Skiff *et al.* [17], who investigated ion heating by SEW in a less collisional plasma. At ES antenna powers below this threshold we do not observe significant ion heating, while at powers above this threshold ions are heating by both SEW and BEW mechanisms.

In previous chapters we have shown that the BEW heating mechanism has the potential of providing a more effective method of ion heating than the SEW mechanism because beating electrostatic waves can interact with ions below the single-wave velocity threshold, given by Eq. (2.8b). We expect that a wave interacting with a larger number of ions will be able to produce higher ion temperatures. Figure 5.5 shows that as the ES antenna power level is increased above 2 W, the ion temperature resulting from the BEW heating increases over that of the SEW heating. To ensure that the increase in the heating effectiveness of the BEW mechanism is due to the waves interacting with particles whose initial velocity

is below the SEW velocity threshold, we check that the bulk of the initial ion velocity distribution function falls below the threshold given by Eq. (2.8b), which we quote here for convenience

$$v = \frac{\omega}{k_{\perp}} - \sqrt{\frac{qE}{k_{\perp}m_i}}. \quad (5.6)$$

Using the value of electric field calculated above, we find that the threshold velocity is $\sim 3 \times 10^5$ cm/s, which is higher than the ion thermal velocity, $v_{ti} \sim 5 \times 10^4$. We, therefore, conclude that the bulk of the initial ion velocity distribution function is below the single-wave velocity threshold for the SEW and BEW, and the higher ion temperature observed with the BEW is a manifestation of threshold-less behavior that allows a larger portion of the distribution function to be energized. We found that the BEW ion heating is $\sim 15\%$ stronger than the SEW heating for the particular conditions used in this experiment. This provides the first evidence of an increase in efficiency between SEW and BEW heating. We expect that this enhancement would be much more significant without the effects of collisions.

The loop ES antenna could not be coupled to the plasma as well as the two-plate antenna. As the result, the heating produced by the loop antenna was significantly smaller. Using the loop antenna, we have attempted to heat ions with either a single or beating waves at frequencies varying from 30 kHz up to 1.8 MHz. We were able to heat ions by $\sim 15\%$ with a wave at 450 kHz, and by $\sim 2.4\%$ at 1.8 MHz. It is interesting to note that at the latter frequency the ion heating most likely results indirectly from the interaction between the lower-hybrid waves and the electrons. Nevertheless, beating waves with $\omega_1 = 1.77$ MHz and $\omega_2 = 1.8$ MHz produced $\sim 5\%$ heating, which is twice the heating produced by the single wave at 1.8 MHz.

5.5 Final Remarks

In this chapter we have reported on the excitation and propagation of Electrostatic Ion Cyclotron (EIC) waves launched by the two-plate ES antenna into a magnetized, rf-sustained argon plasma. We described in detail the circuitry necessary to drive the ES antenna in the in- and out-of-phase configuration. We found that the ES antenna driven in phase couples better to the plasma and can excite a higher amplitude wave than the plates driven out of phase. In addition, we determined that the wave amplitude can be optimized by carefully choosing the right plasma parameters and selecting appropriate electric components to match the driving circuit.

The ES antenna driven in phase excited a wave with $\lambda_{\parallel} = 46$ cm - the length of the test section of the vacuum chamber. The perpendicular component of the wavenumber varies according to the EIC dispersion relation, and is in good agreement with the forward branch of the theoretical dispersion relation despite the simplifying assumption of a homogeneous, isotropic, and infinite plasma slab. As a part of the study we have also investigated the effects of ion-neutral collisions using the electrostatic dispersion relation, and shown that the backward branch of the EIC wave is strongly damped by these collisions. We found that the forward branch of the EIC waves launched at frequencies between ω_{ci} and $10\omega_{ci}$ can propagate with little damping at an angle between 82° and 86° with respect to the magnetic field.

We have also reported on an experimental investigation of the ion heating by a single and beating electrostatic waves in order to explore the heating enhancement predicted by the theory of ion acceleration by beating electrostatic waves. We were able to produce ion heating with a single and beating waves using two different ES antennas. Using the two-plate antenna we were able to increase the ion temperature by $\sim 35\%$ above background. We observed a threshold behavior consistent with the single-particle theory for both single and beating wave heating by increasing the power to the ES antenna. In addition, we showed that beating waves can consistently heat ions to higher temperature than a single

wave within the error bar of the measurement. This enhancement in ion temperature was found to be 15% for the particular conditions of these experiments, but is expected to be significantly higher in a less collisional plasma. This observation supports the theoretical prediction that beating electrostatic waves interact with ions moving below the single-wave velocity threshold.

Chapter 6

Conclusions

Thus, the task is, not so much to see what no one has yet seen; but to think what nobody has yet thought, about that which everybody sees.

– Erwin Schrödinger

This dissertation presented an investigation of the ion heating by beating electrostatic waves (BEW) in a magnetized plasma. This type of heating mechanism may be promising for various applications because the BEW interaction is inherently a non-resonant process that allows the waves to energize arbitrarily slow particles.

Previous works on the BEW heating mechanism [3, 4] were limited to theoretical investigations dealing with one magnetized charged particle. In addition, the theory lacked a description of the necessary and sufficient conditions that govern this interaction. Furthermore, effects of collisions on this interaction have not been investigated. Finally, no experimental studies of the stochastic ion heating by beating electrostatic waves have been previously reported. The work presented in this dissertation has thus been channeled along three directions: 1) theoretical, 2) numerical, and 3) experimental with the following specific aims

- To improve the single-particle theory of the BEW ion heating. Specifically, to determine the necessary and sufficient conditions for the stochastic wave-particle interac-

tion to occur.

- To understand the applicability of the BEW ion heating mechanism to warm collisional plasmas.
- To perform an experimental demonstration of the BEW heating for the first time in a laboratory environment.

6.1 Summary of Major Findings

6.1.1 Theoretical Findings

Theoretical investigation of the model describing the stochastic interaction between a single charged and magnetized particle and beating electrostatic waves revealed that the beating criterion

$$\omega_1 - \omega_2 = n\omega_c,$$

described by Benisti *et al.* [3, 4] provides the necessary but not sufficient condition for the stochastic interaction to occur.

We have found that the necessary and sufficient conditions can be described through the positions of the elliptic and hyperbolic points in the regular acceleration region on the Poincaré section describing the BEW acceleration. These points define an energy well that a particle must overcome in order to be stochastically accelerated by the beating waves. In the notation used throughout this dissertation we call this well the forbidden acceleration region of phase space. This forbidden region can be described by the Hamiltonian of the

two critical points.

$$\begin{aligned}
H([\nu - \sqrt{\varepsilon}]/2; \pi) &< H(\rho_0; \vartheta_0) < H(\nu - \sqrt{\varepsilon}; \pi), \\
\text{with } \rho_0 &< \nu - \sqrt{\varepsilon},
\end{aligned} \tag{6.1}$$

where the subscript “0” refers to the particle initial position on the Poincaré section (i.e. its velocity and phase angle), and H is the system Hamiltonian. Equation (6.1) states that a particle with the Hamiltonian inside the energy well does not interact with the beating waves strongly, and its energy oscillates between the high and low points of the well. On the other hand, particles outside the well are said to be in the allowed acceleration region. These particles strongly interact with the waves, and on average gain energy.

6.1.2 Numerical Findings

While useful, the theoretical model is limited to the BEW interaction with a single particle. In a real plasma, other processes, such as collisions between ions, electrons, and neutral atoms can alter the heating mechanism. We have studied the effects of ion-ion collisions on the BEW heating scheme by conducting Monte Carlo simulations.

Our simulations have shown that ion-ion collisions improve the heating effectiveness of the BEW as well as SEW schemes. In a real plasma, initial ion temperature, plasma density, and wave frequencies can be chosen to optimize the effectiveness of the BEW heating mechanism over that of the SEW.

We have also found that for collisionless plasmas the maximal energy attained by the simulated system (i.e. its temperature, when the distribution is Maxwellian) is a complex function of the wave frequency. Using an analytical model that is based on a simple physical argument we were able to predict the maximal energy dependence on the wave frequency. This model may serve to optimize the plasma and wave parameters for future detailed experimental investigations of the BEW heating mechanism.

6.1.3 Experimental Findings

We have found that an EIC wave could be launched into a magnetized, rf-sustained plasma from a two-plate ES antenna at frequencies up to $10\omega_{ci}$. These waves propagate at the angles between 82° and 86° relative to the external magnetic field. According to the single-particle theory these waves can result in significant ion acceleration [34].

We have also found that in a warm, collisional plasma that is sustained by an rf source, ion-neutral collisions play a key role in electrostatic wave propagation. This effect was not considered in the theoretical and numerical investigations that we have conducted because these studies focused on the wave-particle interaction, and not on the wave generation and propagation mechanisms. For an ion-neutral collision frequency of $\sim 0.2\omega_{ci}$ we found that the backward branch of the EIC wave is strongly damped. Since this is the branch mostly responsible for the wave-ion interaction, the BEW heating mechanism, for our particular experiment, was strongly affected by ion-neutral collisions.

Nevertheless, we have found that even in such a collisional plasma, ions can be heated by $\sim 35\%$ over background level by the electrostatic waves. We have confirmed a threshold in wave energy above which we observe ion heating for both the BEW and SEW mechanisms. This threshold was predicted theoretically by Karney *et al.* [1, 28, 38] and confirmed experimentally by Skiff *et al.* [17] for the single wave heating. Furthermore, we have found that the BEW interaction resulted in 15% greater temperature increase than the SEW interaction (at the same overall wave energy). Based on the dependencies discussed in Chapter 3 we expect the BEW mechanism to result in significantly higher heating in a less collisional plasma, where the relevant parameters are optimized to enhance the heating.

6.2 Recommendations for Future Work

The theoretical, numerical, and experimental studies reported in this dissertation constitute an early step in the exploration of the BEW heating mechanism. Now that the basics of

the mechanism have been elucidated, a more detailed study should be conducted to investigate the relevance of this mechanism to plasmas used specifically for space propulsion applications.

One avenue for investigation can include a more detailed numerical study that simulates the effects of collisions between all species, and includes geometric factors, such as the ES antenna extent, chamber dimensions, and plasma flow past the antenna. This will most likely require an involved PIC/DSMC solver that was beyond the scope of the goals set for this dissertation.

Another direction for future work can be focused on improving the experimental parameters to yield higher ion heating. As we have found, a key parameter for the wave propagation in our experiment is the ratio of ion-neutral collision frequency to the ion cyclotron frequency. This ratio should be lowered at least an order of magnitude in order to observe significant stochastic ion heating. There are multiple ways of achieving this goal. For example this could be done either by increasing the ion cyclotron frequency or lowering the ion-neutral collision frequency.

Lowering ion-neutral collision frequency significantly may require a different plasma source, since rf sources cannot maintain discharges at a neutral pressure much lower than used in the BWX experiment. A good candidate is a Q-machine that can sustain high plasma density while maintaining very low neutral pressure.

On the other hand, the ion cyclotron frequency can be raised by either increasing the magnetic field or utilizing a lighter gas. Both solutions are feasible, but come with their own set of problems. Increasing the magnetic field requires an expensive magnet power supply, and a magnet capable of conducting high currents without overheating. One possible solution to overheating is to pulse the magnet.

Using a lighter gas may make it hard to measure the ion temperature. For example, helium atom is ten times lighter than argon, and may be an ideal candidate for future experiments. However, direct measurements of the helium ion temperature with LIF appears to

be quite difficult [75]. As described in Chapter 5, temperature measurements with RPA and using the ES wave interferometry have also proven unsuccessful in the BWX experiment. An indirect measurement may still be possible.

Finally, ion-neutral collision frequency can be lowered by an appropriate choice of initial conditions, such as ion temperature and plasma density, as well as judiciously selecting ES wave frequency, as discussed in Chapter 3. While decreasing the plasma density while maintaining the same ionization fraction is difficult to achieve in rf-sustained plasma devices, ion temperature could be raised with various means. If the ion temperature is increased by an order of magnitude, significant BEW ion heating with the lower-hybrid waves may be possible, as shown in Fig. 3.6.

Appendix A

Review of Previous Work

This appendix reviews ionospheric rocket observations and previous experimental work on electrostatic wave propagation and particle heating.

A.1 Review of Ionospheric Rocket Observations

In this section of the appendix we review some of the satellite and sounding rocket observations of ion acceleration by electrostatic waves.

Variety of satellite observations indicate that high-energy ions in the Earth's magnetosphere have ionospheric origin [6]. In particular, it has been observed that vigorous ion acceleration from the ionosphere takes place both parallel and perpendicular to the ambient magnetic field at an altitude ranging from 400 km to 8000 km. The most detailed study of ion acceleration was performed by the S3-3 (1976-65B) satellite that was launched in 1976, and performed the first *in situ* measurements of electric fields in the auroral region [7, 8]. The satellite was placed in a nearly polar orbit (8050 km apogee, 260 km perigee, and 97.5° inclination). It contained various mass spectrometers and Langmuir probes. The data collected by the satellite indicated that ions are being accelerated at an altitude of ~ 8000 km. Additional data from the Topaz 3 [2], Isis 1 and 2 [6], OGO 5 [76], Vela 4 [77], Prognosz 7 [78], and other satellites [79, 80, 81, 82], as well as a variety of sounding rockets, such

as the Black Brant series (AAF-IVB-33 and AAF-IVB-36) [83] launched from Canada, showed that the range of the ionospheric acceleration region extends much lower than was determined by S3-3 observations.

In the second part of the 1970's a group at the Palo Alto Research Laboratory published a series of articles that presented and analyzed data obtained by the S3-3 satellite [84, 85, 86, 87]. Their analysis indicated strong (in the keV range) H^+ and O^+ ion acceleration out of the ionosphere and parallel to the magnetic field in the polar regions (5000 – 8000 km) [84]. The analysis also suggested that a field aligned electron flux could be the cause of this acceleration, however the collected data did not establish the direct and unambiguous link between this flux and the ion acceleration. In addition, the data revealed a field-aligned potential drop of up to several kilovolt as another possible source for the parallel ion acceleration [86, 87].

Upon further examination, the data collected by the S3-3 spacecraft revealed that the ions are also being accelerated transversely to the magnetic field to high ($\gtrsim 10$ keV) energies [85]. The region of the maximum perpendicular acceleration was estimated to be 4000 – 5000 km. Mozer *et al.* [7] investigated the plasma density and electric field fluctuations data collected by the S3-3 satellite and determined that the electric field structure observed by the spacecraft was due to formation of the Electrostatic Ion Cyclotron (EIC) waves. The spectrum of the waves observed by the S3-3 satellite varied between 200 Hz and 10 kHz. Existence of electrostatic turbulence in the ionosphere as low as the auroral E and F regions (130 – 400 km) was also discovered by Fejer *et al.* [88] during various ground radar experiments.

In 1963 Motley and D'Angelo [13] performed a series of experiments where they excited a single Electrostatic Ion Cyclotron (EIC) wave in a Q-machine (first described by Rynn and D'Angelo in 1960 [14]) by drawing the electron current along the magnetic field lines. They reported perpendicular ion heating when the current exceeded a certain threshold. These experiments corroborated the S3-3 data, which also showed that the electron

field-aligned current in the ionosphere was above the threshold necessary for the excitation of the hydrogen EIC wave [8].

Kintner *et al.* [8] also analyzed the S3-3 data and demonstrated that the EIC waves in the ionosphere caused predominantly transverse ion acceleration. In particular, they associated both H^+ and O^+ acceleration at the altitude of 5000 – 8000 km with the hydrogen EIC wave. The authors inferred strong perpendicular ion acceleration from the observations of conical ion distribution peaked at 90° angle relative to the Earth’s magnetic field. Okuda and Ashour-Abdalla [89] used a simple numerical model to determine that as a result of the wave-ion interaction the ion temperature becomes anisotropic with $T_i^\perp/T_i^\parallel \gtrsim 10$, as was observed by the spacecraft.

Observations of ion acceleration in the presence of large-amplitude, low-frequency plasma density fluctuations at lower altitudes than those reported by the S3-3 spacecraft were presented and discussed by Yau *et al.* [83] as well as by Satyanarayana and Chaturvedi [78]. They proposed that while the hydrogen ion acceleration occurs primarily at high altitude in the ionosphere (5000 – 8000 km), the oxygen ions are accelerated at the lower altitude (400 – 600 km) of the auroral region. Thus, the electrostatic turbulence and the EIC waves in particular, were observed in all regions of the ionospheric ion acceleration: by the S3-3 satellite at high altitudes, and by a backscatter radar observations reported by Fejer *et al.* in Ref. [88], as was mentioned above.

While the observations clearly linked ion acceleration to electrostatic turbulence, neither the satellite nor the radar data were able to determine the exact acceleration mechanism and point to the source of the EIC waves unambiguously. However, in light of the experimental work by Motley *et al.* [13] and others (to be discussed in the next section), three possible explanations were cited by Kintner and his coworkers [8] as the most likely. The first explanation relied on the field-aligned electron current. The EIC waves could also be excited by the electron diamagnetic drifts or ion beams.

A.2 Review of Previous Laboratory Experiments

While transverse ionospheric ion acceleration was observed in regions of electrostatic wave activity, the satellite observations could not unambiguously point to the wave-ion interaction mechanism as the source of acceleration. Laboratory experiments simulating ionospheric conditions were therefore aimed at determine this interaction mechanism. This section of the appendix provides a brief overview of these experiments, and discusses their relevance to the study reported in this dissertation.

The experimental studies can be subdivided into three main categories. In the first category of experiments, the electron current was drawn parallel to the magnetic field to excite the Current Driven Electrostatic Ion Cyclotron (CDEIC) waves, as first described by Motley and D'Angelo [13]. To this category we can also add the set of experiments where the waves were excited by particle (ions or electrons) field-aligned beams. In the second category, the electrostatic waves were excited by shear flows produced by the radial electric field or diamagnetic drifts without drawing significant field-aligned current. Ganguli *et al.* developed a theory for waves produced this way in a series of papers [90, 91, 92]. The theory showed that the transverse Kelvin-Helmholtz instability could be produced at frequencies below the ion cyclotron frequency and with longer wavelength than the ones observed by the satellites in the Earth's ionosphere. At the shorter wavelength a new class of waves, the Inhomogeneous Energy Density Driven (IEDD) electrostatic waves, was observed with frequencies just above the ion cyclotron harmonics.

Finally, in the third class of experiments, electrostatic waves were excited by means of a driven antenna located either inside [11, 16] or outside [93, 17] of the plasma column. An overview of this class of experiments is particularly important for application to *controlled* plasma heating, relevant for fusion or space plasma propulsion devices.

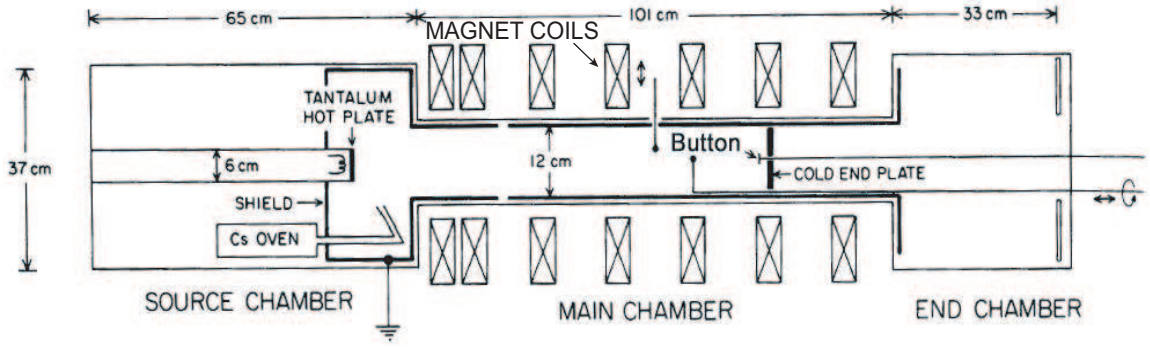


Figure A.1: Schematic of a typical setup for studying the Current Driven Electrostatic Ion Cyclotron (CDEIC) waves using a Q-Machine, such as the one used by Motley and D’Angelo [13]. Electron current, drawn to a biased small exciter disk - “button”, excites the EIC waves. This drawing is taken from Ref. [94].

A.2.1 EIC Waves Excited with Field Aligned Currents (CDEIC)

Historically the Current Driven Electrostatic Ion Cyclotron (CDEIC) waves was the first type of electrostatic waves propagating perpendicularly to the magnetic field studied in the laboratory. This mode was described by Motley and D’Angelo in the early sixties [13]. A comprehensive review of the CDEIC waves is given by Rassmusen and Schrittwieser [95].

The CDEIC waves are typically produced in laboratory plasmas by placing a small “button” electrode into a magnetized plasma column and biasing the button to draw the electron current, as shown in Fig. A.1. For effective wave generation the diameter of the button electrode should be smaller than the diameter of the plasma column but larger than the ion Larmor radius, $r_L \leq r_{button} \leq r_{plasma}$. The CDEIC wave generation is a threshold-type process. The waves are observed when the electrode potential is increased above a threshold described through the electron drift velocity v_{de}

$$v_{de} \gtrsim 5v_{ti},$$

where v_{ti} is the ion thermal velocity. Another characteristic of the CDEIC wave is that its

parallel phase velocity is in resonance with the electron drift velocity

$$\omega/k_{\parallel} \simeq v_{de}$$

In most experiments CDEIC waves were found to have essentially no azimuthal component [95]. In addition, the parallel wavenumber was found to be small: $k_{\parallel}/k_{\perp} \gtrsim (m_e/m_i)^{1/2} \sim 3.7 \times 10^{-3}$ for an argon plasma. Therefore, CDEIC waves propagate nearly perpendicularly to the external magnetic field. A simple dispersion relation for the electrostatic waves propagating perpendicularly to the magnetic field in the ion cyclotron range of frequency can be derived either from fluid theory [13] or from the cold-plasma dispersion directly [68]

$$\omega^2 = \omega_{ci}^2 + k^2 c_s^2, \quad (\text{A.1})$$

where ω_{ci} is the ion cyclotron frequency, k is the wavenumber, and $c_s = (\gamma k_b T_e / m_i)^{1/2}$ is the sound (or Bohm) velocity. This equation, however, assumes that the ions are cold, and misses a different type of electrostatic waves that can coexist in a plasma together with the EIC waves. This will be demonstrated in Chapter 5 through a dispersion relation derived from kinetic theory. This other type may interact with the ions more intensely than the EIC wave.

Kindel and Kennel produced a comprehensive study of CDEIC wave generation in the ionosphere [96]. They found that CDEIC waves propagate at $\omega \simeq \frac{3}{2}\omega_{ci}$. They also found that these waves are unstable to smaller drift velocities v_{de} than either the ion-acoustic or Buneman instabilities for a wide range of the T_e/T_i ratio. In other words, in the ionosphere, CDEIC waves are preferentially excited. A detailed study showed, however, that as T_e/T_i increases, the wave propagation vector becomes more field-aligned. For example, for oxygen with $T_e/T_i \geq 20$ the wave propagates parallel to the magnetic field, and thus turns into the ion-acoustic wave. It was also noted that the electron-ion collisions help in destabilizing the wave while the ion-ion collisions have a stabilizing effect [97].

The field-aligned electron currents observed in the ionosphere were found to have drift velocities above the threshold needed for the CDEIC wave excitation [96].

A.2.2 EIC Waves Excited without Field Aligned Currents

In the absence of the field-aligned current the Electrostatic Ion Cyclotron waves can be excited by other means. Ganguli *et al.* have published a series of papers [91, 90, 92] describing how an electrostatic instability can be excited by a radial electric field. Additionally, electrostatic drift waves with frequencies ranging from the lower hybrid down to the ion cyclotron frequency can also be excited by diamagnetic drifts and perpendicular gradients in density or temperature [98, 99].

Maekawa and Tanaka have used a Retarding Potential Analyzer (RPA) to measure significant ion heating by the ion cyclotron [100] and lower-hybrid [101] drift instabilities in a magnetized helium plasma. Both types of waves were excited by applying potential difference between an anode and cathode and creating a radial electric field in the plasma chamber. For modest values of potential ($V \sim 300$ Volts) the Ion Cyclotron Drift Instability (ICDI) was observed, and at the higher potentials the Lower Hybrid Drift Instability (LHDI) was excited. Gary and Gerwin [102] showed that the ion cyclotron drift wave can be excited by the electron diamagnetic drift instead of the ion diamagnetic drift. Gary and Sanderson [98] investigated the ion cyclotron drift wave propagation as a function of T_e/T_i ratio. They found that the critical drift velocity, v_{de}^* , for destabilizing the wave increases with the temperature ratio. For example, with $m_i = 3674m_e$, they found that v_{de}/v_{ti} ratio increases from 0.03 to 1 as T_e/T_i varies from 0.1 to 10.

A radial electric field can also excite other electrostatic modes, such as the Kelvin-Helmholtz (KH) instability. Sckopke *et al.* [103] reported that the ISEE spacecraft has observed oscillations consistent with the KH instability in the ionosphere. Pritchett and Coroniti [104] studied the excitation and growth of this mode numerically. They found that the KH instability propagates perpendicularly to the magnetic field with wavenumber

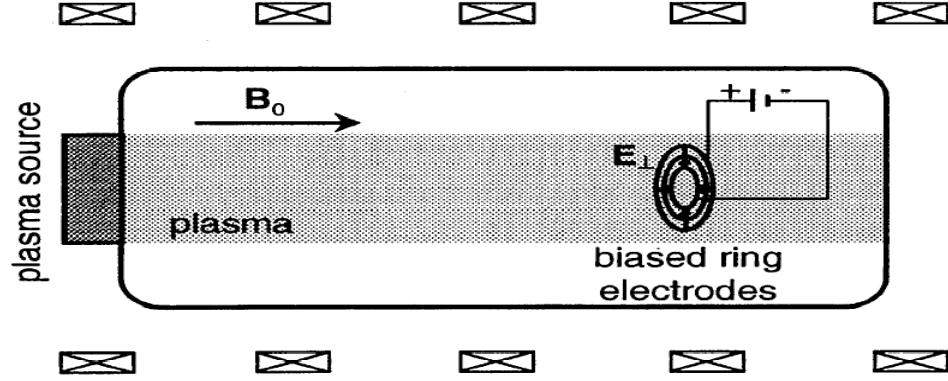


Figure A.2: Schematic of a typical setup for studying the Inhomogeneous Energy Density Driven instability (IEDD). In this type of experiments the EIC wave is excited by the radial electric field imposed by the ring electrodes. The schematic is taken from Ref. [105].

k_{\perp} and the frequency proportional to the potential drop V ($\omega \simeq k_{\perp} V/2$). The Kelvin-Helmholtz instability can be excited when the ion Larmor radius r_L is small ($k_{\perp} r_L \lesssim 0.1$).

Another electrostatic mode arises when the ion Larmor radius is large. In the literature this mode is referred to as the Inhomogeneous Energy Density Driven (IEDD) instability. An experimental apparatus that can excite the IEDD instability with a radial electric field is shown in Fig. A.2. The mode is characterized by its robustness toward various plasma parameters such as collisions and density gradients. Ganguli *et al.* [92] noted that the IEDD instability can exist even at frequencies slightly below the ion cyclotron frequency while the CDEIC waves propagate only above this frequency. Another difference between the IEDD and CDEIC waves can be found by looking at the spectrum produced by the two waves. While the CDEIC waves produce a sharp single-featured spectrum, the IEDD waves result in a broadband feature.

Various groups investigated experimentally the IEDD instability [97, 106, 107, 108, 109] as well as the KH instability [110, 111, 112]. However, since both instabilities can propagate with similar azimuthal wavenumbers there seems to be some confusion in identifying and distinguishing the KH from the IEDD modes [90].

A.2.3 Waves Excited by Antennas

The previous sections dealt with experiments that were motivated primarily by the need to explain the ionospheric observations. In these experiments the electrostatic instabilities were excited indirectly through various drifts and flows, to simulate the ionospheric processes. Some doubt related to the nature of the wave-ion interaction still remained because, with those experiments, it was impossible to separately control the wave excitation and ion heating. Experiments where the waves are launched in a controllable manner from an externally driven antenna make ion heating more tractable. In addition, this type of experiment is beneficial for investigating plasma heating for practical applications, such as fusion and space plasma propulsion.

Figure 1.2 demonstrates schematics of a few such experiments used to investigate various types of electrostatic waves. Sato *et al.* [113] studied propagation of the ion-acoustic wave in a linear device (Q-machine), while Edgley *et al.* [114] investigated a high-frequency electron-plasma wave mode conversion into the ion-acoustic wave. Numerous aspects of the excitation, propagation, and ion heating by the lower-hybrid waves in linear, as well as toroidal, devices were investigated by many authors [9, 115, 10, 116, 117, 118]. For example, Hooke and Barnabei [9] used the capacitively coupled plates and Stenzel and Gekelman [10] employed a set of wires strung along the magnetic field to launch waves close to the LH resonance, as shown in Fig. 1.2a and Fig. 1.2b. Ion heating by electrostatic waves in the ion cyclotron range of frequencies was extensively investigated by Chu *et al.* [119], Ono *et al.* [120], and others [121] in the single-ion plasmas, and by various research groups in multi-ion plasmas [122, 123]. In addition, many groups have investigated propagation of both pure (PIBW) and neutralized (NIBW) Ion Bernstein waves [124, 11, 69, 125]. Figure 1.2c shows an experimental setup for one such experiment, where a single wire at the center of the plasma column was used to launch the PIBW. Schmitt and Krumm investigated mode conversion from an extraordinary wave, launched by a wire coil wrapped around the plasma column into the ion Bernstein wave [12]. Their

experimental setup is shown in Fig. 1.2d.

The following few experiments deserve a special notice because of their relevance to the work presented in this dissertation. Goree *et al.* [16] and Skiff *et al.* [17] used the electrostatic plate antenna to launch a *single* electrostatic wave above the ion cyclotron frequency perpendicularly to the magnetic field in argon and neon plasmas. Similar experiments were performed in hydrogen and deuterium plasmas by Alba *et al.* [18]. These experiments reported significant ion heating. Since our theoretical and numerical investigations have focused on similar frequency range, we have adopted a similar antenna design to launch the beating electrostatic waves.

While helicon sources are relatively new devices [126, 127], some groups have already tried to utilize them for the wave propagation studies. Hanna and Watts [128] have launched Alfvén waves into a helicon plasma, while a group at the West Virginia University demonstrated significant ion heating by a single EIC wave [73, 74].

Appendix B

Derivation of the Hamiltonian

Here we derive the Hamiltonian for a single magnetized ion interacting with multiple transversely propagating electrostatic waves, as shown in Fig. 2.1. Section B.2 derives the non-autonomous Hamiltonian for the BEW interaction. It follows the algorithm described by Karney [28]. Then in Appendix C, we follow the recipe described by Chia *et al.* [33] to derive the autonomous form of the Hamiltonian. That form may be used to obtain the analytical Poincaré sections.

B.1 Lorentz Equation

We choose a constant magnetic field to be in the \hat{z} direction, and let the electrostatic waves propagate in the \hat{x} direction. Under these conditions an ion experiences a gyro motion in the xy plane. We can write down the potential of the waves as:

$$\begin{aligned}\mathbf{E} &= \sum_i E_{i0} \sin(k_i x - \omega_i t + \varphi_i), \\ \phi &= - \int E dx = \frac{E_{i0}}{k_i} \cos(k_i x - \omega_i t + \varphi_i).\end{aligned}\tag{B.1}$$

Remembering that $\mathbf{B} = \nabla \times \mathbf{A}$ we can rewrite the cross product in each direction

$$\begin{aligned} x : \frac{dA_z}{dy} - \frac{dA_y}{dz} &= 0, \\ y : \frac{dA_x}{dz} - \frac{dA_z}{dx} &= 0, \\ z : \frac{dA_y}{dx} - \frac{dA_x}{dy} &= B_0. \end{aligned}$$

We are now free to choose $\mathbf{A} = B_0 x \hat{y}$ without the loss of generality. It should be noted however, that the electric field does not simply equal to the divergence of the electric potential. Instead there is an extra term from the magnetic field contribution. To see that we start with a Maxwell's equation for the curl of \mathbf{E} and add the curl of \mathbf{A} :

$$\begin{aligned} \nabla \times \mathbf{E} &= -\frac{\partial \mathbf{B}}{\partial t} = \frac{\partial}{\partial t} \nabla \times \mathbf{A} \Rightarrow \nabla \times \left(\mathbf{E} + \frac{\partial \mathbf{A}}{\partial t} \right) = 0, \quad \text{therefore we may write} \\ \mathbf{E} + \frac{\partial \mathbf{A}}{\partial t} &= -\nabla \phi \Rightarrow \mathbf{E} = -\nabla \phi - \frac{\partial \mathbf{A}}{\partial t} \end{aligned} \quad (\text{B.2})$$

Now we use Eq. (B.2) in the Lorentz force equation,

$$\mathbf{F} = q(\mathbf{E} + \mathbf{v} \times \mathbf{B}) = q\left(-\nabla \phi - \frac{\partial \mathbf{A}}{\partial t} + \mathbf{v} \times \nabla \times \mathbf{A}\right), \quad (\text{B.3})$$

where we can rewrite the x component of the last term as

$$\begin{aligned} (\mathbf{v} \times \nabla \times \mathbf{A})_x &= v_y \left(\frac{\partial A_y}{\partial x} - \frac{\partial A_x}{\partial y} \right) - v_z \left(\frac{\partial A_z}{\partial z} - \frac{\partial A_z}{\partial x} \right) \\ &= \left(v_x \frac{\partial A_x}{\partial x} + v_y \frac{\partial A_y}{\partial x} + v_z \frac{\partial A_z}{\partial x} \right) - \left(v_x \frac{\partial A_x}{\partial x} + v_y \frac{\partial A_x}{\partial y} + v_z \frac{\partial A_x}{\partial z} \right), \quad (\text{B.4}) \\ \text{where} \quad \left(v_x \frac{\partial A_x}{\partial x} + v_y \frac{\partial A_x}{\partial y} + v_z \frac{\partial A_x}{\partial z} \right) &= \frac{dA_x}{dt} - \frac{\partial A_x}{\partial t}. \end{aligned}$$

With that simplification the last term becomes $(\mathbf{v} \times \nabla \times \mathbf{A})_x = \frac{\partial}{\partial x}(\mathbf{v} \cdot \mathbf{A} + \frac{\partial \mathbf{A}}{\partial t} - \frac{d\mathbf{A}}{dt})$ and the x component of the Lorentz force equation can be rewritten as

$$\begin{aligned} F_x &= q \left(-\frac{\partial \phi}{\partial x} + \frac{\partial}{\partial x}(\mathbf{v} \cdot \mathbf{A} - \frac{d\mathbf{A}}{dt}) \right) \\ &= q \left(-\frac{\partial}{\partial x} - \mathbf{v} \cdot \mathbf{A} \right) - \frac{d}{dt} \left(\frac{\partial}{\partial v_x} \mathbf{v} \cdot \mathbf{A} \right). \end{aligned} \quad (\text{B.5})$$

We can also rewrite the expression above in the Lagrangian form:

$$F_x = -\frac{\partial U}{\partial x} + \frac{d}{dt} \frac{\partial U}{\partial v_x}, \quad \text{where} \quad (\text{B.6a})$$

$$U = q(\phi - \mathbf{v} \cdot \mathbf{A}). \quad (\text{B.6b})$$

The Lagrangian of the system L is defined as $L = T - U$, where $T = \frac{1}{2}(\dot{x}^2 + \dot{y}^2)$ is the kinetic energy of the particle [42]. In expressing the kinetic energy we have chosen the z component to be zero without the loss of generality.

B.2 Canonical Variables

Hamiltonian h of the above system may be expressed in terms of the Lagrangian and the generalized coordinates p_i and q_i as $h = \sum p_i \dot{q}_i - L$, where

$$\begin{aligned} \dot{q}_i &= \frac{\partial h}{\partial p_i}, \quad \dot{p}_i = -\frac{\partial h}{\partial q_i}, \quad p_i = \frac{\partial L}{\partial \dot{q}_i}, \quad \text{and} \\ p_x &= m\dot{x}, \quad p_y = m\dot{y} + qA_y, \\ \dot{q}_x &= \dot{x} = \frac{p_x}{m}, \quad \dot{q}_y = \dot{y} = \frac{p_y - qA_y}{m}. \end{aligned} \quad (\text{B.7})$$

Here q is the charge of the ion, while q_i 's are the generalized positions. After some straightforward algebraic manipulations the Hamiltonian may be re-expressed in terms of the given physical quantities as

$$\begin{aligned}
h &= \frac{1}{2m}[p_x^2 + (p_y - qA_y)^2] + q\phi \\
&= \frac{1}{2m}[p_x^2 + (p_y - qB_0x)^2] + \sum_i \frac{qE_{i0}}{k_i} \cos(k_i x - \omega_i t + \varphi_i).
\end{aligned} \tag{B.8}$$

Now we normalize the variables in the following way

$$\begin{aligned}
\omega_c &= \frac{qB_0}{m}; \quad \tau = \omega_c t; \quad \nu_i = \omega_i / \omega_c; \quad k_i / k_1 = \kappa_i; \quad k_1 x = X; \\
\frac{k_1 q E_{i0}}{m \omega_c^2} &= \varepsilon_i; \quad \frac{k_1}{m \omega_c} p_x = P_x; \quad \frac{k_1}{m \omega_c} p_y = P_y; \quad \frac{k_1^2}{\omega_c^2 m} h = \overline{H}.
\end{aligned} \tag{B.9}$$

In addition, we notice that the Hamiltonian above does not depend on y . With the help of Eqs. (B.7) we see that this implies that p_y is a constant of motion. Therefore, we are free to choose an arbitrary value for it without the loss of generality. We choose $p_y = 0$ to further simplify the problem. Finally, we see that Eqs. (B.7) allow us to set $\dot{x} = p_x$. With all these simplifications we arrive to the following expression describing the Hamiltonian in the normalized coordinate system,

$$\overline{H} = \frac{1}{2}(\dot{X}^2 + X^2) + \sum_i \frac{\varepsilon_i}{\kappa_i} \cos(\kappa_i X - \nu_i \tau + \varphi_i). \tag{B.10}$$

Again, with the help of Eqs. (B.7) we can write down the equation of motion as

$$\ddot{X} + X = \sum_i \varepsilon_i \sin(\kappa_i X - \nu_i \tau + \varphi_i). \tag{B.11}$$

Transforming the coordinates one more time into the action-angle coordinate system we get the following expression for the Hamiltonian,

$$\overline{H} = I_1 + \sum_i \frac{\varepsilon_i}{\kappa_i} \cos(\kappa_i \rho \sin \theta - \nu_i \tau + \varphi_i), \tag{B.12}$$

where $I_1 = \rho/2 = (\dot{X}^2 + X^2)/2$ and $\rho = \dot{X} \cos \theta$ and $\rho = X \sin \theta$. This equation is identical to the one given by Benisti *et al.* [3] and Eq. (2.3).

Appendix C

Lie Transformations

C.1 General Considerations

The general idea behind the Lie transformation perturbation method modified by Deprit [43] consists of the following steps. To obtain the *autonomous* Hamiltonian H from the *non-autonomous* one, \overline{H} , we need to solve the following equation [33],

$$\frac{\partial w}{\partial \tau} = \frac{\partial H}{\partial \varepsilon} - LH - T^{-1} \frac{\partial \overline{H}}{\partial \varepsilon}, \quad (\text{C.1})$$

where w is the Lie generating function, $L = [w, \cdot]$ is the Lie operator ($[\cdot, \cdot]$ is the Poisson bracket), and T is a transformation operator to be described later. We next expand each of the variables in Eq. (C.1) in orders of ε and then solve each order separately. The nonlinear wave-particle interaction phenomenon is a second order effect, so it will suffice to solve Eq. (C.1) to that order. Thus, we express the following functions and variables as power series in ε

$$\begin{aligned} H &= \sum_i \varepsilon^i H_i, \quad \overline{H} = \sum_i \varepsilon^i \overline{H}_i, \quad w = \sum_i \varepsilon^i w_{i+1}, \\ L &= \sum_i \varepsilon^i L_{i+1}, \quad T = \sum_i \varepsilon^i T_i, \quad i = 1, 2, 3, \dots \end{aligned}$$

With these expansions we can define the transformation operator T as follows [33]

$$\begin{aligned} T_n &= -\frac{1}{n} \sum_{m=0}^{n-1} T_m L_{n-m}, \quad \text{and} \\ T_n^{-1} &= \frac{1}{n} \sum_{m=0}^{n-1} L_{n-m} T_m^{-1}, \end{aligned}$$

where $T_0 = T_0^{-1} = I$. Here I is the identity matrix. We are now ready to rewrite Eq. (C.1) using the expansion terms

$$\begin{aligned} \frac{\partial w_n}{\partial t} &= nH_n - \sum_{m=0}^{n-1} L_{n-m} H_m - \sum_{m=1}^n m L_{n-m}^{-1} \bar{H}_m, \quad \text{or} \\ \frac{\partial w_n}{\partial t} + [w_n, \bar{H}_0] &= n(H_n - \bar{H}_n) - \sum_{m=1}^{n-1} (L_{n-m} H_m + m L_{n-m}^{-1} \bar{H}_m) \end{aligned}$$

The left-hand side of the last equation can be thought of as the total derivative of w_n along the invariant of motion (a free ion gyrating in the constant magnetic field). Examining Eq. (B.10) we see that \bar{H} is a first order quantity with respect to ε and $\bar{H}_{2,3,4,\dots} = 0$. Also, we can simplify the left-hand side of the previous equation by writing out the Poisson bracket as

$$[w_n, \bar{H}_0] = \frac{\partial w_n}{\partial \theta} \frac{\partial \bar{H}_0}{\partial I_1} - \frac{\partial w_n}{\partial I_1} \frac{\partial \bar{H}_0}{\partial \theta} = \frac{\partial w_n}{\partial \theta}.$$

Finally, we can rewrite Eq. (C.1) to the zeroth, first, and second orders

$$\bar{H}_0 = H_0 = I_1 = \rho^2/2, \tag{C.2a}$$

$$\frac{\partial w_1}{\partial \tau} + \frac{\partial w_1}{\partial \theta} = H_1 - \bar{H}_1, \tag{C.2b}$$

$$\frac{\partial w_2}{\partial \tau} + \frac{\partial w_2}{\partial \theta} = 2H_2 - L_1(H_1 + \bar{H}_1). \tag{C.2c}$$

The general goal behind solving these equations is this: *Choose self-consistently the Lie generating functions w_1 and w_2 to produce “nice” expressions for H_1 and H_2 .* What is

meant by “nice” will be apparent in the next section.

Before we start solving these equations however, we need to make one more simplifying transformation. A difficulty arises when one tries to solve the terms containing \cos in Eq. (B.12) because they have both ρ and θ dependence. We can use the following identity $e^{\rho/2(t-1/t)} = \sum_{-\infty}^{\infty} t^m J_m(\rho)$ (where J_m are the m^{th} -order Bessel functions of the first kind and $t \neq 0$) to separate these dependencies into different functions [47]

$$\cos(\kappa\rho \sin \theta - \nu\tau) = \sum_m J_m(\kappa\rho) \cos(m\theta - \nu\tau). \quad (\text{C.3})$$

With that, we can rewrite the non-autonomous Hamiltonian as

$$\overline{H} = \overline{H}_0 + \varepsilon_1 \overline{H}_1, \quad (\text{C.4a})$$

$$\overline{H}_0 = I_1 = \rho^2/2, \quad (\text{C.4b})$$

$$\overline{H}_1 = \sum_i \frac{\varepsilon_i}{\varepsilon_1} \frac{1}{\kappa_i} \sum_{-\infty}^{\infty} J_m(\kappa_i \rho) \cos(m\theta - \nu_i \tau + \varphi_i), \quad (\text{C.4c})$$

and the last two equations in the set (C.2) become

$$\frac{\partial w_1}{\partial \tau} + \frac{\partial w_1}{\partial \theta} = H_1 - \sum_i \frac{\varepsilon_i}{\varepsilon_1} \frac{1}{\kappa_i} \sum_{-\infty}^{\infty} J_m(\kappa_i \rho) \cos(m\theta - \nu_i \tau + \varphi_i), \quad (\text{C.5a})$$

$$\begin{aligned} \frac{\partial w_2}{\partial \tau} + \frac{\partial w_2}{\partial \theta} &= 2H_2 \\ &- L_1[H_1 + \sum_i \frac{\varepsilon_i}{\varepsilon_1} \frac{1}{\kappa_i} \sum_{-\infty}^{\infty} J_m(\kappa_i \rho) \cos(m\theta - \nu_i \tau + \varphi_i)]. \end{aligned} \quad (\text{C.5b})$$

We are finally ready to solve these equations. We will do so in the following way. First, we solve the first-order equation. Because of the resonances (the secular terms) there are two cases to solve: 1) the *on-resonance* case when $\nu_i = \text{integer}$, and 2) the *off-resonance* case when $\nu_i \neq \text{integer}$. Then we solve the second-order equation.

C.2 First-Order Solution

$\nu_i = \textit{integer}$: In this case the resonances occur when $\nu_i = m$ in Eq. (C.5a). We therefore choose w_1 to eliminate the secularities [31, 45]

$$w_1 = \sum_i \frac{\varepsilon_i}{\varepsilon_1} \frac{1}{\kappa_i} \sum_{\substack{-\infty \\ m \neq \nu}}^{\infty} J_m(\kappa_i \rho) \frac{\sin(m\theta - \nu_i \tau + \varphi_i)}{\nu_i - m}, \quad (\text{C.6})$$

and the first order autonomous Hamiltonian in this case is

$$H_1^{\textit{on-resonance}} = \sum_i \frac{\varepsilon_i}{\varepsilon_1} \frac{1}{\kappa_i} J_m(\kappa_i \rho) \sin[\nu_i(\theta - \tau) + \varphi_i]. \quad (\text{C.7})$$

$\nu_i \neq \textit{integer}$: The first-order solution for this case is even simpler than for the $\nu_i = \textit{integer}$ case. Again, we want to get rid of the secular terms, but in this case there are none since $\nu_i \neq \textit{integer}$. It follows that

$$H_1^{\textit{off-resonance}} = 0. \quad (\text{C.8})$$

The physical significance of this equation is that it tells us that for the *off-resonance* case, to the first order the average energy is zero. Therefore, all energy exchange between the waves and the ion is a second-order process. Also, this equation provides a hint that the *on-resonance* cases are more complicated because of the first-order term.

Since we need to solve the Hamiltonian to the second order, we have to find w_1 for the *off-resonance* case. Eq. (C.5a) reduces to

$$\frac{\partial w_1}{\partial \tau} + \frac{\partial w_1}{\partial \theta} = 0 - \overline{H}_1, \quad \text{and} \quad (\text{C.9})$$

$$w_1 = \sum_i \frac{\varepsilon_i}{\varepsilon_1} \frac{1}{\kappa_i} \sum_{-\infty}^{\infty} J_m(\kappa_i \rho) \frac{\sin(m\theta - \nu_i \tau + \varphi_i)}{\nu_i - m}, \quad (\text{C.10})$$

We are now ready to proceed to the second-order equations. We will find out quickly

that solving these equations requires quite a bit more algebra.

C.3 Second-Order Solution

$\nu_i \neq \text{integer}$: As was shown in the previous subsection, the first order autonomous Hamiltonian is zero. Unfortunately, we still have to worry about $L_1 \bar{H}_1$ term,

$$L_1 \bar{H}_1 = [w_1, \bar{H}_1] = \frac{1}{\rho} \left[\frac{\partial w_1}{\partial \theta} \frac{\partial \bar{H}_1}{\partial \rho} - \frac{\partial w_1}{\partial \rho} \frac{\partial \bar{H}_1}{\partial \theta} \right]. \quad (\text{C.11})$$

For the sake of simplicity we now proceed to compute that term for the case of only two waves with $\nu_1, \nu_2 \neq \text{integer}$. A generalization for arbitrary number of waves may also be obtained. After a page or so of algebra one can show that

$$\begin{aligned} L_1 \bar{H}_1 = & \sum_{m=-\infty}^{\infty} \sum_{n=-\infty}^{\infty} \frac{m J_m(\rho) J'_n(\rho)}{2\rho(\nu_1 - m)(\nu_1 - n)} \left([2\nu_1 - (m + n)] \cos[(m - n)\theta] \right. \\ & \left. + (m - n) \cos[(m + n)\theta - 2\nu_1\tau + 2\varphi_i] \right) \end{aligned} \quad (\text{C.12a})$$

$$\begin{aligned} & + \sum_{m=-\infty}^{\infty} \sum_{n=-\infty}^{\infty} \frac{m J_m(\rho) J'_n(\kappa\rho)}{2\rho(\nu_1 - m)(\nu_2 - n)} \frac{\varepsilon_2}{\varepsilon_1} \\ & \times \left([(\nu_1 + \nu_2) - (m + n)] \cos[(m - n)\theta - (\nu_1 - \nu_2)\tau + \varphi_1 - \varphi_2] \right. \\ & \left. + [(\nu_2 - \nu_1) + (m - n)] \cos[(m + n)\theta - (\nu_1 + \nu_2)\tau + \varphi_1 + \varphi_2] \right) \end{aligned} \quad (\text{C.12b})$$

$$\begin{aligned} & + \sum_{m=-\infty}^{\infty} \sum_{n=-\infty}^{\infty} \frac{m J_m(\kappa\rho) J'_n(\rho)}{2\rho(\nu_2 - m)(\nu_1 - n)} \frac{\varepsilon_2}{\varepsilon_1} \frac{1}{\kappa} \\ & \times \left([(\nu_2 + \nu_1) - (m + n)] \cos[(m - n)\theta - (\nu_2 - \nu_1)\tau + \varphi_2 - \varphi_1] \right. \\ & \left. + [(\nu_1 - \nu_2) + (m - n)] \cos[(m + n)\theta - (\nu_2 + \nu_1)\tau + \varphi_2 + \varphi_1] \right) \end{aligned} \quad (\text{C.12c})$$

$$\begin{aligned} & + \sum_{m=-\infty}^{\infty} \sum_{n=-\infty}^{\infty} \frac{m J_m(\kappa\rho) J'_n(\kappa\rho)}{2\rho(\nu_2 - m)(\nu_2 - n)} \left(\frac{\varepsilon_2}{\varepsilon_1} \right)^2 \frac{1}{\kappa} \left([2\nu_2 - (m + n)] \cos[(m - n)\theta] \right. \\ & \left. + (m - n) \cos[(m + n)\theta - 2\nu_2\tau + 2\varphi_2] \right). \end{aligned} \quad (\text{C.12d})$$

Again, to obtain the autonomous Hamiltonian we need to choose w_2 to eliminate the secular (resonant) terms. In Eq. (C.12a) the secularities occur when $m = n$ in the first \cos term and $2\nu_1 = m + n$ in the second \cos term. Therefore, the contributions to the autonomous Hamiltonian from these two secular terms respectively are

$$S_1(\rho) = \sum_{m=-\infty}^{\infty} \frac{m J_m(\rho) J'_m(\rho)}{2\rho(\nu_1 - m)}, \quad (\text{C.13})$$

$$S_3(\rho) = \sum_{m=-\infty}^{\infty} \frac{m J_m(\rho) J'_{2\nu_1-m}(\rho)}{2\rho(\nu_1 - m)}. \quad (\text{C.14})$$

Similarly, the secular terms in Eq. (C.12d) occur when $m = n$ and $2\nu_2 = m + n$ in the first and second \cos terms respectively. Their contributions to the autonomous Hamiltonian are

$$\left(\frac{\varepsilon_2^2}{\varepsilon_1}\right) S_2(\rho) = \sum_{m=-\infty}^{\infty} \frac{m J_m(\kappa\rho) J'_m(\kappa\rho)}{2\kappa\rho(\nu_2 - m)}, \quad (\text{C.15})$$

$$\left(\frac{\varepsilon_2^2}{\varepsilon_1}\right) S_4(\rho) = \sum_{m=-\infty}^{\infty} \frac{m J_m(\kappa\rho) J'_{2\nu_2-m}(\kappa\rho)}{2\kappa\rho(\nu_2 - m)}. \quad (\text{C.16})$$

Finally, the secularities in Eq. (C.12c) occur when $m - n = \nu_1 - \nu_2$, $m + n = \nu_1 + \nu_2$, and in Eq. (C.12d) when $m - n = \nu_2 - \nu_1$, $m + n = \nu_2 + \nu_1$. The combined contribution of these two terms to the autonomous Hamiltonian is

$$\begin{aligned} & \left(\frac{\varepsilon_2}{\varepsilon_1}\right) \left[S_5(\rho) \cos[(\nu_1 + \nu_2)(\theta - \tau) + \varphi_1 + \varphi_2] + S_6(\rho) \cos[(\nu_1 - \nu_2)(\theta - \tau) + \varphi_1 - \varphi_2] \right], \\ S_5(\rho) &= \sum_{m=-\infty}^{\infty} \frac{m J_m(\rho) J'_{\nu_1+\nu_2-m}(\kappa\rho)}{2\rho(\nu_1 - m)} + \sum_{m=-\infty}^{\infty} \frac{m J_m(\kappa\rho) J'_{\nu_1+\nu_2-m}(\rho)}{2\kappa\rho(\nu_2 - m)}, \\ S_6(\rho) &= \sum_{m=-\infty}^{\infty} \frac{m J_m(\rho) J'_{\nu_2-\nu_1+m}(\kappa\rho)}{2\rho(\nu_1 - m)} + \sum_{m=-\infty}^{\infty} \frac{m J_m(\kappa\rho) J'_{\nu_1-\nu_2+m}(\rho)}{2\kappa\rho(\nu_2 - m)}. \end{aligned}$$

We are now ready to combine all the terms and write down the complete expression for the autonomous Hamiltonian

$$\begin{aligned}
H_2 = & S_1(\rho) + \left(\frac{\varepsilon_2^2}{\varepsilon_1}\right) S_2(\rho) + S_3(\rho) \cos[2\nu_1(\theta - \tau) + 2\varphi_1] \\
& + \left(\frac{\varepsilon_2^2}{\varepsilon_1}\right) S_4(\rho) \cos[2\nu_2(\theta - \tau) + 2\varphi_2] \\
& + \left(\frac{\varepsilon_2}{\varepsilon_1}\right) S_5(\rho) \cos[(\nu_1 + \nu_2)(\theta - \tau) + \varphi_1 + \varphi_2] \\
& + \left(\frac{\varepsilon_2}{\varepsilon_1}\right) S_6(\rho) \cos[(\nu_1 - \nu_2)(\theta - \tau) + \varphi_1 - \varphi_2]
\end{aligned} \tag{C.17}$$

Our derivation is not yet complete because the equation above is not precisely correct. In our derivation we assumed that $\nu \neq \text{integer}$. However, even with that assumption secular terms may still occur whenever $2\nu = \text{integer}$. To place the proper restrictions on the above equation we note that the terms (C.12a-C.12d) place the following constraints respectively: $2\nu_1 \neq \text{integer}$, $2\nu_2 \neq \text{integer}$, $|\nu_2 - \nu_1| \neq \text{integer}$, $\nu_1 + \nu_2 \neq \text{integer}$. The second-order contribution to the autonomous Hamiltonian is then

$$\begin{aligned}
H_2 = & S_1(\rho) + \left(\frac{\varepsilon_2^2}{\varepsilon_1}\right) S_2(\rho) + \delta_1 S_3(\rho) \cos[2\nu_1(\theta - \tau) + 2\varphi_1] \\
& + \delta_2 \left(\frac{\varepsilon_2^2}{\varepsilon_1}\right) S_4(\rho) \cos[2\nu_2(\theta - \tau) + 2\varphi_2] \\
& + \delta_3 \left(\frac{\varepsilon_2}{\varepsilon_1}\right) S_5(\rho) \cos[(\nu_1 + \nu_2)(\theta - \tau) + \varphi_1 + \varphi_2] \\
& + \delta_4 \left(\frac{\varepsilon_2}{\varepsilon_1}\right) S_6(\rho) \cos[(\nu_1 - \nu_2)(\theta - \tau) + \varphi_1 - \varphi_2],
\end{aligned} \tag{C.18}$$

where $\delta_1, \delta_2, \delta_3, \delta_4 = 1$ when $2\nu_1, 2\nu_2, \nu_1 - \nu_2, \nu_1 + \nu_2 = \text{integer}$ respectively, and zero otherwise.

$\nu_i = \textbf{integer}$: In this case the derivation is similar to the one given above. It could be shown that the second-order terms are also given by Eq. (C.18).

C.4 Autonomous Hamiltonian to the Second Order

We now derive the expression for the second-order autonomous Hamiltonian describing the interaction between two electrostatic waves and a magnetized ion. For the off-resonance case ($\nu_1, \nu_2 \neq \text{integer}$) the Hamiltonian is

$$\begin{aligned}
H^{off-resonance} = & \varepsilon_1^2 S_1(\rho) + \varepsilon_2^2 S_2(\rho) + \delta_1 \varepsilon_1^2 S_3(\rho) \cos[2\nu_1 \vartheta + 2\varphi_1] \\
& + \delta_2 \varepsilon_2^2 S_4(\rho) \cos[2\nu_2 \vartheta + 2\varphi_2] \\
& + \delta_3 \varepsilon_1 \varepsilon_2 S_5(\rho) \cos[(\nu_1 + \nu_2)\vartheta + \varphi_1 + \varphi_2] \\
& + \delta_4 \varepsilon_1 \varepsilon_2 S_6(\rho) \cos[(\nu_1 - \nu_2)\vartheta + \varphi_1 - \varphi_2], \tag{C.19}
\end{aligned}$$

where we have used a generating function of the second kind, $F_2 = \vartheta \cdot I_1$, where $\vartheta = \theta - \tau$ and $I_1 = \rho/2$, to rewrite the Hamiltonian in its autonomous form, as described by Chia *et al.* in Ref. [33]. It should be noted that equivalent Poincaré sections are constructed as ρ vs. θ from numerical solutions of Eq. (2.1) and as ρ vs. ϑ by plotting lines of $H = \text{const}$ using Eq. (C.21) (below). However, for the purposes of constructing Poincaré sections ϑ and θ are equivalent variables since the least common period used to construct these sections is always a multiple of 2π and ϑ appears inside either “sin” or “cos” terms.

For the on-resonance case we need to add the first-order term to Eq. (C.19)

$$\begin{aligned}
H^{on-resonance} = & \varepsilon_1 J_{\nu_1}(\rho) \cos[\nu_1 \vartheta + \varphi_1] + \varepsilon_2 \frac{J_{\nu_2}(\kappa\rho)}{\kappa} \cos[\nu_2 \vartheta + \varphi_2] \tag{C.20} \\
& + H^{off-resonance}.
\end{aligned}$$

According to Benisti *et al.* S_3 and S_5 terms are small [3]. Finally, we can generalize the second-order autonomous Hamiltonian for the case of multiple propagating electrostatic

waves as

$$\begin{aligned}
H &= \sum_{\nu_1 \in N} \frac{\varepsilon_i}{\kappa_i} J_{\nu_i}(\kappa_i \rho) \cos[\nu_i \vartheta + \varphi_i] + \sum_{\nu_i} \varepsilon^2 S^{(i)}(\rho) \\
&+ \sum_{\nu_i - \nu_j \in M\{0\}} \varepsilon_i \varepsilon_j S_6^{(i,j)}(\rho) \cos[(\nu_i - \nu_j) \vartheta + \varphi_1 - \varphi_2] \quad (\text{C.21})
\end{aligned}$$

For two waves the equation above can be reduced to Eq. (2.6) by setting $\kappa_i = 1$ and $\varphi_i = 0$, as described in Section 2.3.

Appendix D

$S_6^{\nu_i, \nu_j}(\rho)$ Term Simplification

Using Eq. (2.11) and substituting for $J_m(\rho)$ and $J'_m(\rho)$ with the following identities [46]

$$\begin{aligned} J_{m-1}(\rho) + J_{m+1}(\rho) &= \frac{2m}{\rho} J_m(\rho), \\ J_{m-1}(\rho) - J_{m+1}(\rho) &= 2J'_m(\rho), \end{aligned} \tag{D.1}$$

we can rewrite $S_6^{\nu_i, \nu_j}(\rho)$ as

$$\begin{aligned} S_6^{\nu_i, \nu_j}(\rho) &= \frac{1}{8} \left\{ \sum \frac{J_{m+2}(\rho) J_{m+1}(\rho)}{\nu - m} \right. \\ &+ \sum \frac{J_m(\rho) J_{m+1}(\rho)}{\nu - m} - \sum \frac{J_{m-1}(\rho) J_{m+2}(\rho)}{\nu - m} \\ &- \sum \frac{J_m(\rho) J_{m-1}(\rho)}{\nu - m} + \sum \frac{J_{m-1}(\rho) J_{m-2}(\rho)}{\nu - m} \\ &+ \sum \frac{J_{m+1}(\rho) J_{m-2}(\rho)}{\nu - m} - \sum \frac{J_m(\rho) J_{m-1}(\rho)}{\nu - m} \\ &\left. - \sum \frac{J_m(\rho) J_{m+1}(\rho)}{\nu - m} \right\}. \end{aligned} \tag{D.2}$$

Now we use the following identity [21]

$$\sum_{m=-\infty}^{\infty} \frac{J_{m+p}(\rho) J_m(\rho)}{\nu - m} = \frac{\pi}{\sin \pi \nu} J_{p+\nu}(\rho) J_{-\nu}(\rho),$$

which is valid for $p > 0$ to simplify Eq. (D.2) to

$$\begin{aligned} S_6^{\nu_i, \nu_j}(\rho) &= \frac{\pi}{8 \sin \pi \nu} [2J_{\nu+2}(\rho)J_{-(\nu+1)}(\rho) \\ &\quad - 2J_{\nu}(\rho)J_{-(\nu-1)}(\rho)], \end{aligned}$$

which, with the help of identities (D.1), may be shown to be

$$\begin{aligned} S_6^{\nu_i, \nu_j}(\rho) &= \frac{\rho}{\nu} \frac{\pi}{\sin \pi \nu} [J_{\nu+1}(\rho)J_{-(\nu+1)}(\rho) \\ &\quad - J_{\nu-1}(\rho)J_{-(\nu-1)}(\rho)] \\ &\quad + \frac{\rho}{(\nu+1)} \frac{\pi}{\sin \pi(\nu+1)} [J_{\nu}(\rho)J_{-\nu}(\rho) \\ &\quad - J_{\nu+2}(\rho)J_{-(\nu+2)}(\rho)]. \end{aligned}$$

Chia *et al.* [33] showed that $S_1^{\nu_i}(\rho)$ can be simplified as

$$\begin{aligned} S_1^{\nu_i}(\rho) &= \frac{\pi}{8 \sin \pi \nu_i} [J_{\nu_i+1}(\rho)J_{-(\nu_i+1)}(\rho) \\ &\quad - J_{\nu_i-1}(\rho)J_{-(\nu_i-1)}(\rho)]. \end{aligned}$$

It is then clear that

$$S_6^{\nu_i, \nu_j}(\rho) = \frac{\rho}{\nu_i} S_1^{\nu_i}(\rho) + \frac{\rho}{\nu_j} S_1^{\nu_j}(\rho). \quad (\text{D.3})$$

Finally, we caution that the relation (D.3) holds only for the special case of $\nu_i \neq \text{integer}$ and $\nu_j = \nu_i + 1$.

Appendix E

Symplectic Integration Algorithm

To solve Eq. (2.1) or Eq. (2.3) numerically one can use a 4th order Runge-Kutta algorithm. While being a standard numerical technique, this algorithm does not take into account the Hamiltonian nature of the stochastic heating problem. A symplectic numerical method that preserves the invariants of motion was developed by Candy and Rozmus [129]. A numerical routine based on their method was used in this dissertation to study the stochastic interaction between electrostatic waves and a single charged particle.

The symplectic integration algorithm (SIA4) is described in detail in Ref. [129]. Here we give the necessary steps to apply the method to Eq. (2.3).

First, we need to separate the Hamiltonian into the components,

$$H(\mathbf{q}, \mathbf{p}, t) = T(\mathbf{p}) + V(\mathbf{q}, t), \quad (\text{E.1})$$

where \mathbf{q} and \mathbf{p} are the canonical variables. In our case $T = \dot{X}^2/2$ and $V = -X^2/2 + \sum \varepsilon_i \cos(\kappa_i X - \nu_i \tau)$.

After choosing the initial condition (\dot{X}_0, X_0) we advance the solution in time in the

i	1	2	3	4
a_i	$\frac{1}{6}(2 + 2^{1/3} + 2^{-1/3})$	$\frac{1}{6}(1 - 2^{1/3} - 2^{-1/3})$	$\frac{1}{6}(1 - 2^{1/3} - 2^{-1/3})$	$\frac{1}{6}(2 + 2^{1/3} + 2^{-1/3})$
b_i	0	$(2 - 2^{1/3})^{-1}$	$(1 - 2^{2/3})^{-1}$	$(2 - 2^{1/3})^{-1}$

Table E.1: Values of the coefficients for the SIA4 algorithm.

following manner:

For $i = 1$ to 4 :

$$\dot{X}_i = \dot{X}_{i-1} + b_i F(X_{i-1}, \tau_{i-1}) \delta \tau,$$

$$X_i = X_{i-1} + a_i P(\dot{X}_i) \delta \tau,$$

$$\tau_i = \tau_{i-1} + a_i \delta \tau. \tag{E.2}$$

The variables (\dot{X}_4, X_4) give the values of (\dot{X}, X) at the next time step $\tau = \tau_0 + \delta \tau$. In the equations above functions $F(\mathbf{q}, t)$ and $P(\mathbf{p})$ are,

$$F(\mathbf{q}, t) = -\nabla_{\mathbf{q}} V(\mathbf{q}, t) = -X + \sum \varepsilon_i \sin(\kappa_i X - \omega_i \tau),$$

$$P(\mathbf{p}) = \nabla T(\mathbf{p}) = \dot{X}.$$

The values of a_i and b_i are tabulated in Table E.1.

Appendix F

ES Dispersion for a Homogeneous, Isotropic, Magnetized, Collisional Plasma

Physics is like sex. Sure, it may give some practical results, but that's not why we do it.

– Richard Feynman

In this appendix we derive the electrostatic dispersion relation for a homogeneous, isotropic, magnetized, collisional plasma. A very similar derivation was made by Choueiri [66] for unmagnetized ions. Here we generalize that derivation to include magnetized ions. We also model the ion-neutral collisions through an adjusted BGK collision operator as described by Dougherty in Ref. [130]. The first-order Vlasov equation for any charged species can be written as

$$\frac{\partial f_1}{\partial t} + \mathbf{v} \cdot \nabla_x f_1 + \frac{q}{m} E_1 \cdot \nabla_v f_0 + \frac{q}{m} \mathbf{v} \times B_0 \cdot \nabla_v f_1 = -\nu \left(f_1 - \frac{n_1}{n_0} f_0 \right), \quad (\text{F.1})$$

where all first-order variables vary as $e^{i(k \cdot v - \omega t)}$, and ν is the collision frequency. Note that by summing over all charged species the final dispersion relation will be general enough to include all collisions in a plasma (i.e. ion-neutral and electron-neutral collisions). The

following operator substitutions can now be made: $\partial/\partial t \rightarrow -i\omega$ and $\nabla_x \rightarrow i\mathbf{k}$. The equation above can be rewritten as,

$$-i(\omega - k_z v_z - k_\perp v_\perp \cos \theta + i\nu)f_1 + \omega_c \frac{\partial f_1}{\partial \theta} = \frac{iq}{m} \mathbf{k} \Phi \cdot \nabla_v f_0 + \nu \frac{n_1}{n_0} f_0, \quad (\text{F.2})$$

where we have expressed the electric field of the wave as $E_1 = -i\mathbf{k}\Phi$ and switched to cylindrical coordinates, shown in Fig. 2.1. We have also assumed, without any loss of generality that $\mathbf{k} = k_\perp \hat{y} + k_z \hat{z}$. After dividing by ω_c we see that the equation above is a first-order, ordinary, inhomogeneous equation of the type $y' + P(x)y = Q(x)$, which can be solved by the method of integrating factors [131] to obtain the following solution,

$$\begin{aligned} f_1 &= \frac{1}{\omega_c} \left[\frac{iq}{m} \mathbf{k} \Phi \cdot \nabla_v f_0 + \nu \frac{n_1}{n_0} f_0 \right] e^{\frac{i(w+i\nu-k_z v_z)}{\omega_c} \theta} e^{-i \frac{k_\perp v_\perp}{\omega_c} \sin \theta} \\ &\times \int e^{\frac{i(w+i\nu-k_z v_z)}{\omega_c} \theta} e^{i \frac{k_\perp v_\perp}{\omega_c} \sin \theta} d\theta. \end{aligned} \quad (\text{F.3})$$

With the help of the following identities

$$f_0 = \frac{n_0}{\pi \sqrt{\pi} v_t^3} e^{-v_\perp^2/v_t^2} e^{-v_z^2/v_t^2}, \quad (\text{F.4})$$

$$e^{i \frac{k_\perp v_\perp}{\omega_c} \sin \theta} = \sum e^{in\theta} J_n \left(\frac{k_\perp v_\perp}{\omega_c} \right), \quad (\text{F.5})$$

$$e^{-i \frac{k_\perp v_\perp}{\omega_c} \sin \theta} = \sum e^{-in\theta} J_n \left(\frac{k_\perp v_\perp}{\omega_c} \right), \quad (\text{F.6})$$

$$\sum J_n(z) = \sum \frac{n}{z} J_n(z), \quad (\text{F.7})$$

where J_n is the Bessel function of the first kind and v_t is the species thermal velocity, the first-order velocity distribution can finally be rewritten as

$$f_1 = \frac{q}{T} f_0 \sum_n \sum_m \frac{J_n J_m e^{i(n-m)\theta}}{w + i\nu - n\omega_c - k_z v_z} \left[(k_z v_z + n\omega_c) \Phi + i\nu \frac{n_1}{n_0} \frac{T}{q} \right]. \quad (\text{F.8})$$

In the following calculations it is helpful to express the distribution function as $f_1 = A\Phi +$

Bn_1 , where

$$\begin{aligned}
A &= \frac{q}{T} \frac{n_0}{\pi v_t^3} \sum_n \sum_m e^{i(n-m)\theta} F_\perp(v_\perp) A(v_z), \\
B &= \frac{q}{T} \frac{n_0}{\pi v_t^3} \sum_n \sum_m e^{i(n-m)\theta} F_\perp(v_\perp) B(v_z), \\
F_\perp(v_\perp) &= J_n\left(\frac{k_\perp v_\perp}{\omega_c}\right) J_m\left(\frac{k_\perp v_\perp}{\omega_c}\right) e^{-v_\perp^2/v_t^2}, \\
A(v_z) &= \frac{1}{\sqrt{\pi}} \frac{k_z v_z + n\omega_c}{\omega + i\nu - n\omega_z - k_z v_z} e^{-v_z^2/v_t^2}, \\
B(v_z) &= \frac{i}{\sqrt{\pi}} \frac{\nu T}{qn_0} \frac{1}{\omega + i\nu - n\omega_z - k_z v_z} e^{-v_z^2/v_t^2}.
\end{aligned}$$

We immediately notice that the velocity distribution depends on $n_1 (= \int f_1 d^3\mathbf{v})$, which itself depends on f_1 . However, since n_1 is not a function of velocity we can express it as

$$n_1 = \frac{\int A d^3\mathbf{v}}{1 - \int B d^3\mathbf{v}} \Phi, \quad (\text{F.9})$$

$$\text{where } \int d^3\mathbf{v} = \int_0^{2\pi} d\theta \int_\infty^\infty v_\perp dv_\perp \int_\infty^\infty dv_z \quad (\text{F.10})$$

which upon combining with the Poisson equation produces the dispersion equation

$$k^2 - \frac{q}{\epsilon_0} \frac{\int A d^3\mathbf{v}}{1 - \int B d^3\mathbf{v}} = 0, \quad (\text{F.11})$$

where $k^2 = k_\perp^2 + k_z^2$. The rest of this section is dedicated to evaluating the integrals in Eq. (F.11). Integrating both A and B over the angle θ allows the following contractions,

$$\begin{aligned}
\int_0^{2\pi} d\theta e^{i(n-m)\theta} &= 2\pi \delta(n-m) \\
A &= \frac{2qn_0}{T} \frac{1}{v_t^3} \sum_n F_\perp(v_\perp) A(v_z), \\
B &= \frac{2qn_0}{T} \frac{1}{v_t^3} \sum_n F_\perp(v_\perp) B(v_z), \\
F_\perp(v_\perp) &= J_n^2\left(\frac{k_\perp v_\perp}{\omega_c}\right) e^{-v_\perp^2/v_t^2}.
\end{aligned}$$

Next we integrate over v_\perp ,

$$\int_0^\infty v_\perp dv_\perp F_\perp(v_\perp) = \frac{1}{2} v_t^2 e^{-\mu} I_n(\mu),$$

where $\mu = k_\perp^2 v_t^2 / 2\omega_c$, and $I_n(\mu)$ is the modified Bessel function of the first kind. Integration over v_z is a bit more complicated

$$\begin{aligned} \int_0^\infty dv_z A(v_z) &= -v_t [1 + \xi_0 Z(\xi_n)], \\ \int_0^\infty dv_z B(v_z) &= -\frac{i\nu T}{qn_0 k_z} Z(\xi_n), \\ \text{where } \xi_n &= \frac{\omega + i\nu - n\omega_c - k_z v_z}{k_z v_t}, \\ \text{and } Z(\xi_n) &= \int_0^\infty \frac{e^{-z} dz}{z - \xi_n}. \end{aligned}$$

Combining all integrals and summing over all charged species (ions and electrons) we obtain,

$$1 + \sum_s \alpha_s \frac{1 + e^{-\mu_s} \xi_{0s} \sum_n I_n(\mu_s) Z(\xi_{ns})}{1 + i(\nu_s / k_z v_{ts}) e^{-\mu_s} \sum_n I_n(\mu_s) Z(\xi_{ns})} = 0, \quad (\text{F.12})$$

where $\alpha_s = 1/k^2 \lambda_{Ds}^2$ and λ_{Ds} is the Debye length. It could be easily checked that upon setting all collision frequencies to zero Eq. (F.12) reduces to the familiar collisionless electrostatic dispersion relation, e.g. Eq. (85) given by Stix in Ref. [68].

Bibliography

- [1] C.F.F. Karney and A. Bers. Stochastic ion heating by a perpendicularly propagating electrostatic wave. *Phys. Rev. Lett.*, 39:550, 1977.
- [2] A.K. Ram, A. Bers, and D. Benisti. Ionospheric ion acceleration by multiple electrostatic waves. *J. Geophys. Res.*, 103:9431, 1998.
- [3] D. Benisti, A.K. Ram, and A. Bers. Ion dynamics in multiple electrostatic waves in a magnetized plasma. I. Coherent acceleration. *Phys. Plasma*, 5(9):3224, September 1998.
- [4] D. Benisti, A.K. Ram, and A. Bers. Ion dynamics in multiple electrostatic waves in a magnetized plasma. II. Enhancement of the acceleration. *Phys. Plasma*, 5(9):3233, September 1998.
- [5] R.T.Tsunoda, R.C.Livingston, J.F.Vickrey, R.A.Heelis, W.B.Hanson, F.J.Rich, and P.F.Bythrow. Dayside observations of thermal-ion upwellings at 800-km altitude: An ionospheric signature of the cleft ion fountain. *J.Geophys.Res.*, 94(A11):15,277, November 1989.
- [6] D.M. Klumpar. Transversely accelerated ions: An ionospheric source of hot magnetospheric ions. *J. Geophys. Res.*, 84(A8):4229, 1979.

- [7] Mozer F.S., C.W. Carlson, M.K. Hudson, R.B. Torbert, B. Parady, and J. Yatteau. Observations of paired electrostatic shocks in the polar magnetosphere. *Phys. Rev. Lett.*, 38(6):292, 1977.
- [8] P.M. Kintner, M.C. Kelley, R.D. Sharp, A.G. Ghielmetti, M. Temerin, C. Cattell, P.F. Mizera, and J.F. Fennell. Simultaneous observations of energetic (keV) upstreaming and electrostatic hydrogen cyclotron waves. *J. Geophys. Res.*, 84(A12):7201, 1979.
- [9] W.M. Hooke and S. Bernabei. Direct observation of waves propagating near the lower-hybrid-resonance frequency. *Phys. Rev. Lett.*, 28(7):407, February 1972.
- [10] R.L. Stenzel and W. Geikelman. Electrostatic waves near the lower hybrid frequency. *Phys. Rev. A*, 11(6):2057, June 1975.
- [11] J.P.M. Schmitt. Dispersion and cyclotron damping of pure ion Bernstein waves. *Phys. Rev. Lett.*, 31(16):982, October 1973.
- [12] J.P.M. Schmitt and P. Krumm. Mode conversion and plasma column resonances in the ion-cyclotron harmonic range. *Phys. Rev. Lett.*, 37(12):753, September 1976.
- [13] R.W. Motley and N. D'Angelo. Excitation of electrostatic plasma oscillations near ion cyclotron frequency. *Phys. Fluids.*, 6(2):296, February 1963.
- [14] Rynn N. and N. D'Angelo. Device for generating a low temperature, highly ionized cesium plasma. *Rev. Sci. Instrum.*, 31(12):1326, December 1960.
- [15] S.L. Cartier, N. D'Angelo, and R.L. Merlino. A laboratory study of ion energization by eic waves and subsequent upstreaming along diverging magnetic field lines. *J. Geophys. Res.*, 91(A7):8025, July 1986.
- [16] J. Goree, M. Ono, and L. K. Wong. Observation of the backward electrostatic ion-cyclotron wave. *Phys. Fluids*, 28(9):2845, September 1985.

- [17] F. Skiff, F. Anderegg, and M.Q. Tran. Stochastic particle acceleration in an electrostatic wave. *Phys. Rev. Lett.*, 58(14):1430, April 1987.
- [18] S. Alba, G. Carbone, M. Fontanesi, A Galassi, C Riccardi, and E. Sindoni. Stochastic particle acceleration in an electrostatic wave. *Plasma Phys. Controlled Fusion*, 34(2):147, 1992.
- [19] G.M. Zaslavsky and N.N.Filonenko. Stochastic instability of trapped particles and conditions of applicability of the quasi-linear approximation. *Zh.Eksp.Theor.Fiz.*, 64(1590-1602):851, 1968.
- [20] G.M. Zaslavsky, M.Yu Zakharov, R.Z. Sagdeev, and A. A. Chernikov. Stochastic web and diffusion of particles in a magnetic field. *Zh.Eksp.Theor.Fiz.*, 91(500-516):294, 1986.
- [21] G.M. Zaslavsky, R.Z. Sagdeev, D.A. Usikov, and A. A. Chernikov. Minimal chaos, stochastic webs, and structures of quasicrystal symmetry. *Usp. Fiz. Nauk*, 156(193-251):887, October 1988.
- [22] G.M. Zaslavsky, R.Z. Sagdeev, D.A. Usikov, and A.A. Chernikov. *Weak chaos and quasi-regular patterns*. Cambridge University Press, Cambridge, 1991.
- [23] G.R. Smith and A.N. Kaufman. Stochastic acceleration by a single wave in a magnetic field. *Phys. Rev. Lett.*, 34(26):1613, 1975.
- [24] A. Fukuyama, H. Momota, R. Itatani, and T. Takizuka. Stochastic acceleration by electrostatic wave near ion cyclotron harmonics. *Phys. Rev. Lett.*, 38:701, 1977.
- [25] G.R. Smith and A.N. Kaufman. Stochastic acceleration by an obliquely propagating wave - an example of overlapping resonances. *Phys.Fluids*, 21(12):2230, 1978.
- [26] N. Singh, R.W. Schunk, and J.J. Sojka. Cyclotron resonance effects on stochastic acceleration of light ionospheric ions. *Geoph.Res.Lett.*, 9(9):1053, 1982.

- [27] C.R. Menyuk, J.M. Dawson, V.K. Decyk, B.D. Decyk, B.D. Fried, and G.J. Morales. Nonlinear evolution of obliquely propagating langmuir wave. *Phys.Rev.Lett.*, 48(16):1104, 1982.
- [28] C.F.F. Karney. Stochastic ion heating by a lower hybrid wave. *Phys.Fluids*, 21(9):1584, September 1978.
- [29] K. Papadopoulos, Jr. J.D Gaffey, and P.J. Palmadesso. Stochastic acceleration of a large m/q ions by hydrogen cyclotron waves in the magnetosphere. *Geoph.Res.Lett.*, 7(11):1014, 1980.
- [30] R.L. Lysak, M.K Hudson, and M.Temerin. Ion heating by strong electrostatic ion cyclotron turbulence. *J.Geoph.Res.*, 85(A2):678, 1980.
- [31] A.J. Lichtenberg and M.A. Lieberman. *Regular and Stochastic Motion*, volume 38 of *Applied Mathematical Sciences*. Springer-Verlag, New York, 1983.
- [32] P.Deeskow, K.Elsässer, and F.Jestczemski. Critical wave spectra for stochastic heating of a magnetized plasma. *Phys.Fluids B*, 2(7):1551, 1990.
- [33] Ping-Kun Chia, L. Schmitz, and R.W. Conn. Stochastic ion behavior in subharmonic and superharmonic electrostatic waves. *Phys. Plasmas*, 3(5):1545, May 1996.
- [34] D.J. Strozzi, A.K. Ram, and A. Bers. Coherent acceleration of magnetized ions by electrostatic waves with arbitrary wavenumbers. *Phys. Plasmas*, 10(7):2722–2731, March 2003.
- [35] D. Benisti, A.K. Ram, and A. Bers. Lower bound in energy for chaotic dynamics of ions. *Phys. Lett. A*, 233:209, August 1997.
- [36] D.W Longcope and R.N.Sudan. Arnol’d diffusion in $1\frac{1}{2}$ dimensions. *Phys.Rev.Lett.*, 59(14):1500, 1987.

- [37] A.A. Chernikov, M.Ya. Natenzon, B.A. Petrovichev, R.Z. Sagdeev, and G.M. Zaslavsky. Some peculiarities of stochastic layer and stochastic web formation. *Phys.Lett.A.*, 122(1):39, 1987.
- [38] C.F.F. Karney. Stochastic ion heating by a lower hybrid wave:ii. *Phys.Fluids*, 22(11):2188, November 1979.
- [39] C.T Dum and T.H Dupree. Nonlinear stabilization of high-frequency instabilities in a magnetic field. *Phys.Fluids*, 13(8):2064, 1970.
- [40] L. Chen, Z.Lin, and R.White. On resonant heating below the cyclotron frequency. *Phys.Plasmas*, 8(11):4713, 2001.
- [41] R.White, L. Chen, and Z.Lin. Resonant plasma heating below the cyclotron frequency. *Phys.Plasmas*, 9(5):1890, 2002.
- [42] H. Goldstein. *Classical Mechanics*. Addison-Wesley, Cambridge, MA, 1951.
- [43] A. Deprit. *Celest. Mech.*, 1:12, 1969.
- [44] R. Candy and W. Rozmus. Rational resonances in a wave driven linear oscillator. *Physica D*, 52:267, 1991.
- [45] R. Grimshaw. *Nonlinear Ordinary Differential Equations*. Blackwell Scientific Publications, Oxford, 1990.
- [46] G.N. Watson. *A Treatise on the Theory of Bessel Functions*. Cambridge University Press, Cambridge, 2 edition, 1962.
- [47] M. Abramowitz and I.A. Stegun. *Handbook of Mathematical Functions*. Dover Publications, Inc., New York, 1965.

- [48] E.Y. Choueiri and R. Spektor. Coherent ion acceleration using two electrostatic waves. Presented at the 36th AIAA Joint Propulsion Conference, Huntsville, AL, July 16-20, 2000. AIAA-2000-3759.
- [49] T. Takizuka and H. Abe. A binary collision model for plasma simulation with a particle code. *J. Comp. Phys.*, 25:205–219, 1977.
- [50] M. Mitchner and C. H. Kruger Jr. *Partially Ionized Gases*. John Wiley & Sons, Inc, 2nd edition, 1992.
- [51] R. Spektor and E.Y. Choueiri. Ion acceleration by beating electrostatic waves: Domain of allowed acceleration. *Phys.Rev.E*, 69(4):046402, April 2004.
- [52] G.A. Goree. *The backward electrostatic ion-cyclotron wave, fast wave current drive, and fir laser scattering*. Ph.d, Princeton University, 1985.
- [53] A. Fasoli, F. Skiff, and M.Q. Tran. Study of wave-particle interaction from the linear regime to dynamical chaos in a magnetized plasma. *Phys. plasmas*, 1(5):1452, May 1994.
- [54] R. Sudit and F. F. Chen. Rf compensated probes for high-density discharges. *Plasma Sources Sci. Technol*, 3:162–168, 1994.
- [55] J.G.Laframboise. Technical Report 100, University of Toronto, Institute for Aerospace Studies, 1966. Document No. AD634596.
- [56] F.F.Chen, J.D. Evans, and D.Arnush. A floating potential method for measuring ion density. *Phys.Plasmas*, 9(4):1449, April 2002.
- [57] D.E. Smith, E.J. Powers, and G.S. Cladwell. Fast-fourier-transform spectral-analysis techniques as a plasma fluctuation diagnostic tool. *IEEE Trans. Plasma Sci.*, PS-1:261, December 1974.

- [58] F. Skiff and F. Anderegg. Direct observation of plasma dielectric motion. *Phys. Rev. Lett.*, 59(8):896, August 1987.
- [59] M. Sarfaty, S. De Souza-Machado, and F. Skiff. Direct determination of ion wave fields in a hot magnetized and weakly collisional plasma. *Phys. Plasmas*, 3(12):4316, December 1996.
- [60] R.A. Stern and J.A. Johnson, III. Plasma ion diagnostics using resonant fluorescence. *Phys. Rev. Lett.*, 34(25):1548, June 1975.
- [61] D. Hill, S. Fornaca, and M.G. Wickham. Single frequency scanning laser as a plasma diagnostic. *Rev.Sci.Instrum.*, 54(3):309, March 1983.
- [62] G.D. Severn, D.A. Edrich, and R. McWilliams. Argon ion laser-induced fluorescence with diode lasers. *Rev.Sci.Instrum.*, 69(1):10, January 1998.
- [63] J.L. Kline. *Slow Wave Ion Heating and Parametric Instabilities in the HELIX Helicon Source*. Ph.d, West Virginia University, 2002.
- [64] E. Scime, C. Biloiu, C. Compton, F. Doss, D. Venture, J. Heard, E. Choueiri, and R. Spektor. Laser induced fluorescence in a pulsed argon plasma. *Rev. Sci. Instrum.* 76, 026107 (2005), 76:026107, 2005.
- [65] G. D. Conway, A. J. Perry, and R. W. Boswell. Evolution of ion and electron energy distributions in pulsed helicon plasma discharges. *Plasma Sources Sci. Technol.*, 7:337, 1998.
- [66] E. Y. Choueiri. Anomalous resistivity and heating in current-driven plasma thrusters. *Phys. Plasmas*, 6(5):2290, May 1999.
- [67] E. Y. Choueiri. Instability of a current-carrying finite-beta collisional plasma. *Phys.Rev.E*, 64:066413, November 2001.

- [68] T.H. Stix. *Waves in Plasmas*. Springer-Verlag, New York, 1992.
- [69] M.Ono and K.L. Wong. Externally launched ion bernstein wave in the act-1 toroidal device. *Phys.Rev.Lett.*, 45(13):1105, September 1980.
- [70] R.H. Neynaber, S.M. Trujillo, and E.W. Rothe. Symmetric-resonance charge transfer in ar from 0.1–20 ev using merging beams. *Phys.Rev.*, 157(1):101, May 1967.
- [71] A.V. Phelps. The application of scattering cross sections to ion flux models in discharge sheaths. *Phys.Rev. Lett.*
- [72] C. Biloiu, X. Sun, E. Choueiri, F. Doss, E. Scime, J. Heard, R. Spektor, and D. Ventura. Evolution of the parallel and perpendicular ion velocity distribution function in pulsed helicon plasma sources obtained by time resolved laser induced fluorescence. *To be published in Physics of Plasmas*, , pages = ,.
- [73] J.L. Kline. Resonant ion heating in a helicon plasma. Ms, West Virginia University, 1998.
- [74] J. Kline, E. Scime, P.A. Keiter, M.M. Balkey, and R.F. Boivin. Ion heating in the helix helicon plasma source. *Phys.Plasmas*, 6(12):4767–4772, December 1999.
- [75] E.E. Scime, P.A. Keiter, M.W. Zintl, M.M. Balkey, J.L. Kline, and M.E. Koepke. Control of ion temperature anisotropy in a helicon plasma. *Plasma Sources Sci. Technol.*, 7:186, 1998.
- [76] R.W. Fredricks, G.M. Crook, C.F. Kennel, I.M. Green, and F.L. Scarf. Ogo 5 observations of electrostatic turbulence in bow shock magnetic structures. *J. Geophys. Res., Space Phys.*, 75(19):3751, 1970.
- [77] M.D. Montgomery, J.R. Asbridge, and S.J. Bame. Vela 4 plasma observations near the earth’s bow shock. *J. Geophys. Res.*, 75(19):1217, 1970.

- [78] P. Satyanarayana, P.K. Chaturvedi, M.J. Keskinen, J.D. Huba, and S.L. Ossakow. Theory of the current-driven ion cyclotron instability in the bottomside ionosphere. *J. Geophys. Res.*, 90(A12):12,209, 1985.
- [79] P.M. Kintner, J. Bonnell, R.L. Arnoldy, K. Lynch, C.J. Pollock, and T.E. Moore. Scifer - transverse ion acceleration and plasma waves. *Geophys. Res. Lett.*, 23(14):1873, 1996.
- [80] T.E. Moore, M.O. Chandler, C.J. Pollock, D.L. Reasoner, R.L. Arnoldy, B. Austin, P.M. Kintner, and J. Bonnell. Plasma heating and flow in an auroral arc. *J. Geophys. Res.*, 101(A3):5279, 1996.
- [81] P.M. Kintner, J. Bonnell, R.L. Arnoldy, K. Lynch, C.J. Pollock, J. Moore, T.E. Holtet, C. Deehr, H. Stenbaek-Nielsen, R. Smith, and J. Olson. The scifer experiment. *Geophys. Res. Lett.*, 23(14):1865, 1996.
- [82] G. Lu, P.H. Reiff, T.E. Moore, and R.A. Heelis. Upflowing ionospheric ions in the auroral region. *J. Geophys. Res.*, 97(A11):16,855, 1992.
- [83] A.W. Yau, B.A. Whalen, A.G. McNamara, P.J. Kellogg, and W. Bernstein. Particle and wave observations of low-altitude ionospheric ion acceleration events. *J. Geophys. Res.*, 88(A1):341, 1983.
- [84] E.G. Shelley, R.D. Sharp, and R.G. Johnson. Satellite observations of an ionospheric acceleration mechanism. *J. Geophys. Res.*, 3(11):654, 1976.
- [85] R.D. Sharp, R.G. Johnson, and E.G. Shelley. Observation of an ionospheric acceleration mechanism producing energetic (kev) ions primarily normal to the geomagnetic field direction. *J. Geophys. Res.*, 82(22):3324, 1977.

- [86] A.G. Gielmetti, R.G. Johnson, R.D. Sharp, and E.G. Shelley. The latitudinal, diurnal, and altitudinal distributions of upward flowing energetic ions of ionospheric origin. *Geophys. Res. Lett.*, 5(1):59, 1978.
- [87] R.D. Sharp, R.G. Johnson, and E.G. Shelley. Energetic particle measurements from within ionospheric structures responsible for auroral acceleration process. *J. Geophys. Res.*, 84(A2):480, 1979.
- [88] Fejer B.G., R.W. Reed, D.T. Farley, W.E. Swartz, and M.C. Kelley. Ion cyclotron waves as a possible source of resonant auroral radar echoes. *J. Geophys. Res.*, 89(A1):187, 1984.
- [89] H. Okude and M. Ashour-Abdalla. Formation of a conical distribution and intense ion heating in the presence of hydrogen cyclotron waves. *Geophys. Res. Lett.*, 8(7):811, 1981.
- [90] Ganguli G., Y.C. Lee, and P.J. Palmadesso. Kinetic theory for electrostatic waves due to transverse velocity shears. *Phys. Fluids*, 31(4):823, April 1988.
- [91] Ganguli G., Y.C. Lee, and P.J. Palmadesso. Electrostatic ion-cyclotron instability caused by a nonuniform electric field perpendicular to the external magnetic field. *Phys. Fluids*, 28(3):761, March 1985.
- [92] Ganguli G. Stability of an inhomogeneous transverse plasma flow. *Phys. Plasmas*, 4(5):1544, May 1997.
- [93] T. Watari, T. Hatori, R.Kumazawa, T. Akoi, T. Kawamoto, M. Inutake, S. Hiroe, A. Nishizawa, K. Adati, T.Sato, T.Watanabe, and H.Obayashiand K.Takayama. Radio-frequency plugging of a high density plasma. *Phys.Fluids*, 21(11):2076, November 1978.

- [94] D.M. Suszcynsky, S.L. Cartier, R.L. Merlino, and N. D'Angelo. A laboratory study of collisional electrostatic ion cyclotron waves. *J. Geophys. Res.*, 91(A12):13,729, December 1986.
- [95] J.J. Rasmussen and R.W. Schrittwieser. On the current-driven electrostatic ion-cyclotron instability: A review. *IEEE Trans. Plasma Sci.*, 19(3):457, June 1991.
- [96] J.M. Kindel and C.F. Kennel. *J. Geophys. Res.*, 76(13):3055, 1971.
- [97] M.E. Koepke, M.W. Zintl, and T.N. Good. An effect of neutral collisions on the excitation threshold of electrostatic ion-cyclotron waves. *Geoph. Res. Lett.*, 25(16):3095, August 1998.
- [98] S.P. Gary and J.J. Sanderson. Density gradient drift instabilities: Oblique propagation at zero beta. *Phys. Fluids*, 21(7):1181, July 1978.
- [99] J.P. Fredberg and R.A. Gerwin. Lower hybrid instability at low drift velocities. *Phys. Fluids*, 20(8):1311, August 1977.
- [100] T. Maekawa and S. Tanaka. Ion cyclotron drift instability driven by cross-field electron current and plasma heating. *J. Phys. Soc. Japan*, 44(4):1354, April 1978.
- [101] T. Maekawa and S. Tanaka. Lower hybrid drift instability driven by cross-field electron current and ion heating. *J. Phys. Soc. Japan*, 45(6):1992, December 1978.
- [102] S.P. Gary and R.A. Gerwin. Electrostatic ion cyclotron electron drift instability. *Phys. Fluids*, 22(9):1764, September 1979.
- [103] N. Sckopke, G. Paschmann, G. Haerendel, B.U.Ö. Sonnerup, S.J. Bame, T.G. Forbes, E.W. Hones Jr., and C.T. Russell. Structure of the low-latitude boundary layer. *J. Geophys. Res.*, 86(A4):2099, April 1981.

- [104] P.L. Pritchett and F.V. Coroniti. The collisionless macroscopic kelvin-helmholtz instability. 1. transverse electrostatic mode. *J.Geophys.Res.*, 89(A1):168, January 1984.
- [105] D.N. Walker, W.E. Amatuucci, G. Ganguli, J.A. Antoniadis, J.H. Bowles, D. Duncan, V. Gavrishchaka, and M.E. Koepke. Perpendicular ion heating by velocity-shear-driven waves. *Geoph.Res. Lett.*, 24(10):1187, May 1997.
- [106] M.E. Koepke, W.E. Amatuucci, J.J. Carroll III, and M.W. Zintl. Excitation and propagation of electrostatic ion-cyclotron waves in plasma with structured transverse flow. *Phys. Plasmas*, 5(5):1671, May 1998.
- [107] M.E. Koepke, W.E. Amatuucci, J.J. Carroll III, and Sheridan T.E. Experimental verification of the inhomogeneous energy-density driven instability. *Phys. Rev. Lett.*, 72(21):3355, May 1994.
- [108] M.E. Koepke, W.E. Amatuucci, J.J. Carroll III, and V. Gavrishchaka. Velocity-shear-induced ion-cyclotron turbulence: Laboratory identification and space applications. *Phys. Plasmas*, 2(6):2523, June 1995.
- [109] W. E. Amatuucci, D. N. Walker, G. Ganguli, J. A. Antoniadis, D. Duncan, J. H. Bowles, V. Gavrishchaka, and M. E. Koepke. Plasma response to strongly sheared flow. *Phys. Rev. Lett.*, 77(10):1978, September 1996.
- [110] D.L. Jassby. Evolution and large-electric-field suppression of the transverse kelvin-helmholtz instability. *Phys. Rev. Lett.*, 25(22):1567, November 1970.
- [111] D.L. Jassby and F.W. Perkins. Transverse kelvin-helmholtz instability in a q-machine plasma. *Phys. Rev. Lett.*, 24(6):256, February 1970.
- [112] G.I. Kent, N.C. Jen, and F.F. Chen. Transverse kelvin-helmholtz instabilities in a rotating plasma. *Phys. Fluids*, 12(10):2140, October 1969.

- [113] N.Sato, H. Sugai, A.Sasaki, and R.Hatakeyama. Two propagating modes of low-frequency waves in a single-ended q-machine. *Phys. Fluids*, 17(1):456, February 1974.
- [114] P.D.Edgley, R.N.Franklin, S.M.Hamberger, and R.W. Motley. High-frequency driven ion-cyclotron instability. *Phys.Rev.Lett.*, 34(20):1269, May 1975.
- [115] R.J. Briggs and R.R. Parker. Transport of rf energy to the lower hybrid resonance in an inhomogeneous plasma. *Phys. Rev. Lett.*, 29(13):852, September 1972.
- [116] T.Ohnuma, K.Shibata, and S.Adachi. Radiation of electrostatic plasma near the lower hybrid frequency. *Phys.Rev. A*, 16(1):387, July 1977.
- [117] P.M.Bellan and M.Porkolab. Excitation of lower-hybrid waves by slow-wave structure. *Phys.Rev.Lett.*, 34(3):124, January 1975.
- [118] P.M.Bellan and M.Porkolab. Experimental studies of lower hybrid wave propagation. *Phys. Fluids*, 19(7):995, July 1976.
- [119] T.K Chu, S.Bernabei, and R.W. Motley. Parametrically driven ion cyclotron waves and intense ion heating. *Phys.Rev.Lett.*, 31(4):211, July 1973.
- [120] M.Ono, G.A. Wurden, and K.L. Wong. Efficient ion heating via finite-larmor-radius ion-cyclotron waves in a plasma. *Phys.Rev. Lett.*, 52(1):37, January 1984.
- [121] T.Ohnuma, S.Miyake, T.Sato, and T.Watari. Propagation of electrostatic ion waves near ion cyclotron harmonics. *Phys.Rev.Lett.*, 26(10):541, March 1971.
- [122] M.Ono, M.Porkolab, and R.P.H Chang. Parametric excitation of electrostatic ion cyclotron waves in a multi-ion-species plasma. *Phys.Rev.Lett.*, 38(17):962, April 1977.
- [123] M.Ono. Cold, electrostatic, ion-cyclotron and ion-ion hybrid resonances. *Phys.Rev.Lett.*, 42(19):1267, May 1979.

- [124] J.P.M. Schmitt. Resonance of an antenna associated with the excitation of ion Bernstein modes. *Phys.Fluids*, 15(11):2057, November 1972.
- [125] M.Ono, T.Watari, R.Ando, J.Fujita, Y.Hirokura, K.Ida, E.Kako, K.Kawahata, Y.Kawasumi, K. Matsuoka, A.Nishizawa, N.Noda, I. Ogawa, K.Ohkubo, M.Oknamoto, K.Sato, S.Tanahashi, Y.Taniguchi, T.Tetsuka, K.Toi, and K.Yamazaki. Ion-bernstein-wave heating in the jippt-ii-u tokamak plasma. *Phys.Rev.Lett.*, 54(21):2339, May 1985.
- [126] R. Boswell and F.F. Chen. Helicons - the past decade. *IEEE Trans. Plasma Sci.*, 25(6):1245, December 1997.
- [127] R. Boswell and F.F. Chen. Helicons - the early years. *IEEE Trans. Plasma Sci.*, 25(6):1229, December 1997.
- [128] J.Hanna and C.Watts. Alfvén wave propagation in a helicon plasma. *Phys. Plasmas*, 8(9):4251, September 2001.
- [129] R. Candy and W. Rozmus. A symplectic integration algorithm for separable hamiltonian functions. *J. Comp. Phys.*, 92:230, 1991.
- [130] J.P. Dougherty. The conductivity of a partially ionized gas in alternating electric field. *J. Fluid Mech.*, 16:126, November 1963.
- [131] E. Kreyszig. *Advanced Engineering Mathematics*. John Wiley, 8th edition, 1999.